TECHNISCHE UNIVERSITÄT MÜNCHEN
LEHRSTUHL FÜR THERMODYNAMIK
Prof. em. Dr.-Ing. Dr.-Ing. E.h. F. Mayinger

Diploma Thesis

Laser-Optical Visualization of Detonation Structures

Florian Pintgen

Advisors:

Prof. J.E. Shepherd
California Institute of Technology

Dipl.-Ing. Andreas Eder
Prof. em. Dr.-Ing. Dr.-Ing. E.h. F. Mayinger
Technische Universität München

Dezember 2000

Acknowledgements

The experiments for this report were carried out during my seven-month stay in the Graduate Aeronautics Laboratory at the California Institute of Technology (GALCIT) under the supervision of Prof. J.E. Shepherd. The purpose of my visit was to compile a thesis in order to complete my degree at the Technische Universität München. I would like to thank Prof. Mayinger for his support in this matter.

I express my thanks to Prof. Shepherd for his invaluable advice, suggestions and patience during my stay at Caltech.

My gratitude also to A. Eder (TU München) for his helpful ideas, C. Gerlach (TU München) for his assistance regarding the laser system and both for their decent "hand-on" education over the last four years in Munich. Furthermore thanks to J. Austin for her help in operating the explosion tube and the whole team at the Explosion Dynamics Laboratory.

Contents

List of Figures

Nomenclature

AB	light source dimension
A	focal area of the lightsheet
A_{21}	spontaneous emission rate constant
$A'B'$	image of light source
a	displacement of deflected beam at schlieren edge
B	CCD dimensions,
B_{21}	Einstein transition probability for stimulated emission
b_{nm}	absoption or stimulated emission rate constant
c	speed of light
c_p	specific heat capacity (constant pressure)
d	particle diameter
E	energy
F	fluorescence signal power
f_x	focal length of lens/mirror X
h	Planck's constant
I_ν	laser irradiance per per unit frequency interval (spectral irradiance)
I^ν_{sat}	saturation spectral irradiance
k	Bolzmann's constant
L_i	lens/ mirror i of schlieren head
M	Mach number
$\dot{m}$	mass-flow
N	number density

n	refraction index
O	focusing lens
P	predissociative rate constant
p	pressure
Q_{21}	quenching rate constant
q	heat per unit mass
R	gas constant
R_{ij}	integral rate coefficients
r	distance between schlieren edge and focusing lens
S	schliere
S'	image of schliere
s	distance between schliere and schlieren edge
T	temperature
u	velocity
W_{2i}	photoionisation rate constant
β	magnification factor
γ	ratio of specific heats
Δ	extension of the schliere along optical axis
δ	diameter of distortion
ε	angle of deflection in schliere
λ	wave length
ν	frequency
Ω	solid angle of detection
ϱ	density
τ_i	induction time

Chapter 1

Introduction

The coupling between the leading shock and the reaction front plays a major role in the propagation of detonations. In this work, fully developed detonations are investigated in a tube closed at both ends. Two optical techniques, the schlieren technique and the Planar Laser Induced Fluorescence technique (PLIF), are described and applied to detonations. The schlieren technique enables the visualization of shock waves and the PLIF technique enables investigation of species distributions in the gaseous mixture.

Most previous experimental studies investigated detonation structure by applying one optical measurement technique per experiment. Often integrating methods, for example shadowgraphs, were used. To overcome this, the detonation is often restricted to travel in a thin channel with a width on the order of the cell size. Integrating visualization techniques are often insufficient to resolve the complex three-dimensional behavior of the detonation structure. The only way to visualize the three-dimensional structure of the detonation front is to use non-integrating methods, which enable "cuts" through the flow field. The application of LIPF [AWW+92] and Rayleigh-scattering [AD92] insufficient signal intensity compared to the natural fluorescence and did not resolve details of the reaction front. The images presented in this work were by exciting the OH radical, an intermediate species in the combustion process, which functions as a direct marker of regions where chemical reaction is taking place. The obtained images have a sufficient resolution and signal to noise ration (SNR) to clearly identify for the first time, the features of the reaction zone connected to the cellular structure of the detonation front.

In some cases, simultaneous schlieren images were obtained and superposed with the PLIF

images. The simultaneous application of both techniques is suitable for the investigation of the coupling between the shock and the reaction front, and is helpful in interpreting the features seen on the PLIF images.

Chapter 2

Fundamentals of Detonations

In general, there are two types of combustion processes: premixed flames and non-premixed or diffusion controlled flames. For premixed combustion, the reactants are perfectly mixed before the chemical reaction takes place. In the case of a non-premixed or diffusion controlled combustion the reactants, the oxidizer and fuel, are separated and diffuse into each other during the chemical reaction. Premixed combustion waves can be divided into two categories: deflagration and detonation. Here the focus is on detonation.

2.1 Deflagration and Detonation

A deflagration is a combustion process which is driven by mechanisms of heat- and mass transfer. It can be influenced by shock waves but is not induced by them. Unreacted gas is heated to the necessary reaction temperature from the hot parts of the reaction zone through radiation, heat- and mass-transfer and diffusion.
A detonation is, in contrast to a deflagration, shock-induced. The shock wave compresses the unburned gas, creating the thermodynamic conditions necessary for the gas to react. The shock and reaction fronts are coupled with each other, since the reaction acts like a piston that drives the shock wave. The system is always supersonic with respect to the upstream gas.

2.2 Reaction Front Model

If a parallel, reacting, friction-free, one-dimensional flow is assumed, the continuity, conservation of energy and conservation of momentum equations in the shock-fixed frame are:

$$\text{continuity:} \qquad \varrho_1 u_1 = \varrho_2 u_2 \tag{2.1}$$

$$\text{energy:} \qquad \frac{u_1^2}{2} + h_1 + q_{12} = \frac{u_2^2}{2} + h_2 \tag{2.2}$$

$$\text{momentum:} \qquad p_1 + \varrho_1 u_1^2 = p_2 + \varrho_2 u_2^2 \tag{2.3}$$

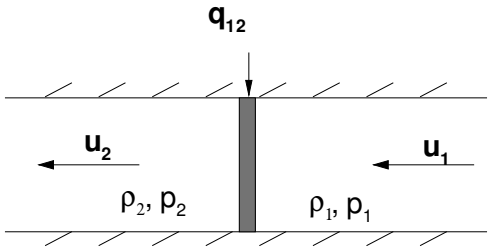

Figure 2.1: One-dimensional reaction-front model of Bartlmä [Bar75].

The reaction front is assumed to be infinitely thin and is treated as a discontinuity where the chemical energy is released. The coordinate system is attached to the reaction front, Fig. 2.1. The term q is the chemical energy release per unit mass, which can also be representad as an equivalent heat addition q_{12}. Furthermore the following realations for an ideal gas have to be used:

$$h = c_p T \tag{2.4}$$

$$p = \varrho R T \tag{2.5}$$

$$c_p = \frac{\gamma}{\gamma - 1} R \tag{2.6}$$

In order to simplify the discussion, we assume that the parameters q, γ and R are constants and have the have the same value in th reactants and products. Eliminating the velocities from the conservation equations leads to the Rankine-Hugoniot relation:

$$\frac{\gamma}{\gamma - 1}\left(\frac{p_2}{\varrho_2} - \frac{p_1}{\varrho_1}\right) - \frac{1}{2}(p_2 - p_1)\left(\frac{1}{\varrho_1} + \frac{1}{\varrho_2}\right) = q \ , \tag{2.7}$$

where γ is the specific heat ratio and ϱ and p are the density and the pressure in the unburned (subscript 1) and burned (subscript 2) region. The energy per unit mass can be made

dimensionless by dividing by the enthalpy per unit mass of the unburned gas $c_p T_1$. The non-dimensional heat of reaction can be defined as:

$$Q = \frac{q}{c_p T_1} \ . \tag{2.8}$$

The dimensionless quantity Q represents the chemical energy content relative to the thermal energy of the reactants. Equation (2.7) can so be rewritten as:

$$\frac{p_2}{p_1} = \frac{\frac{\gamma+1}{\gamma-1} - \frac{\varrho_1}{\varrho_2} + \frac{2\gamma}{\gamma-1} Q}{\frac{\gamma+1}{\gamma-1}\frac{\varrho_1}{\varrho_2} - 1} \ . \tag{2.9}$$

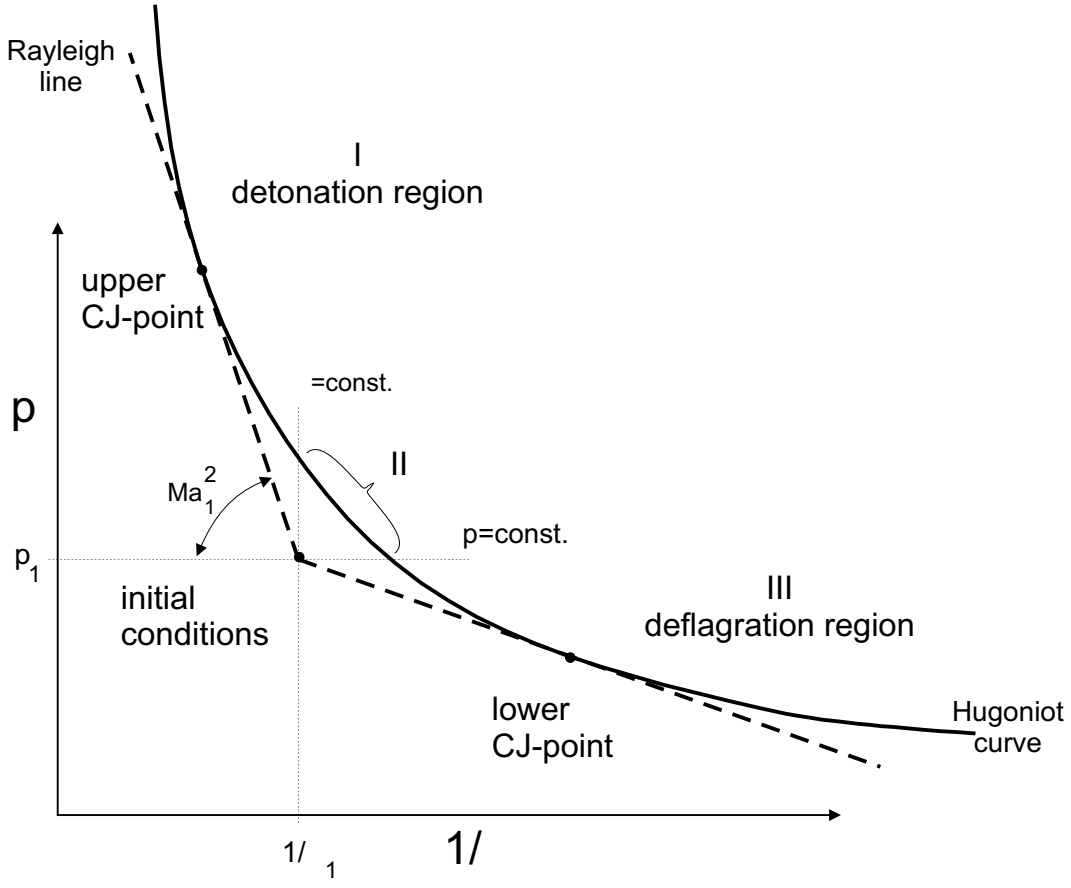

Figure 2.2: Different sections of the Hugoniot curve.

The Hugoniot curve is a plot of all the possible values of $1/\varrho$ and p_2 for a given values of $1/\varrho$, p_1 and Q. The point of the initial conditions ($1/\varrho$, p_1) is called the origin of the Hugoniot curve (Fig.2.2). Different values of Q represent different mixture compositions. An array of curves

can be plotted for different mixture compositions. The Hugoniot curve for $Q = 0$ describes the relation of pressure and density for an adiabatic shock and originates at the initial states of the reactants.

Combining only the equations for continuity and conservation of momentum leads to the Rayleigh line relation:

$$(1 - \frac{\varrho_1}{\varrho_2}) \cdot \gamma \, M_1^2 \, = (\frac{p_2}{p_1} - 1) \; . \tag{2.10}$$

The Rayleigh line equation does not take direct account of the chemical nature of the medium. The slope of the Rayleigh line is characteristic for the upstream flow velocity and is equal to $-\gamma M a_1^2$. All Rayleigh lines pass through the point (ϱ_1, p_1).

The Hugoniot curve can be divided into three regions by drawing horizontal and vertical lines from the origin A. The horizontal line represents combustion at constant pressure, the vertical line isochoric combustion. The solutions for region II are not possible since equ. 2.10 implies an imaginary wave speed for these cases. Region I is called the detonation region, region III the deflagration region.

2.3 The Chapman-Jouguet Model

The Chapman Jouguet-model assumes a shock with and an infinitesimally thin reaction front directly behind the shock, where all of the chemical energy is released. The criteria for a stable propagation of that system is that the gas flow, directly behind the reaction front, is sonic so that small disturbances behind the front can not reach the reaction front. That criteria is fulfilled if the Rayleigh line is tangent to the Hugoniot curve, Fig. 2.2.

The point of tangency is the upper Chapman-Jouguet point (upper CJ point). The coordinates of that point describe the thermodynamic state for a one-dimensional steady detonation propagation in that particular mixture. The portion of the Hugoniot point above the upper CJ point represents the so-called strong detonation solution, the lower portion represents the weak detonation solution. These unsteady regions are observed in transient situations and convergent tubes. In a straight tube without obstacles, detonations are normally CJ-waves. The Rayleigh line can be tangent to the deflagrative part of the Hugoniot curve as well. That

point is called the lower CJ point.

2.4 The ZND model

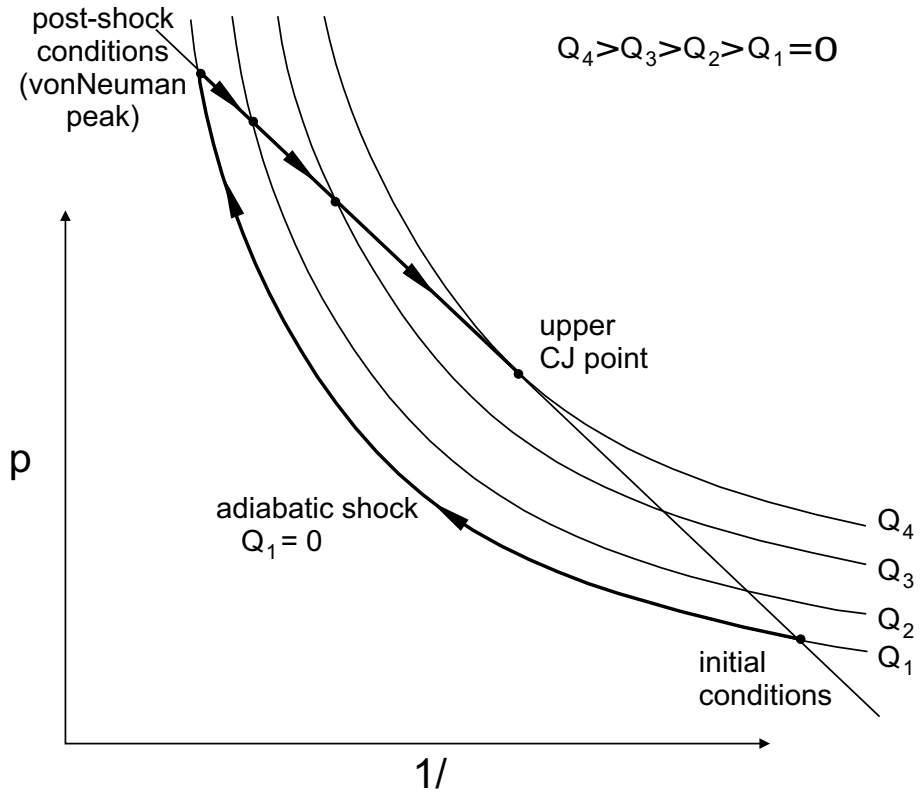

Figure 2.3: Upper CJ point and subsequent reaction.

The ZND model gives a more detailed view of the detonation wave. This one-dimensional model was suggested independently by Zeldovich, von Neumann and Döring, [Zel50], [vN42]. The initial shock transition to the so-called von Neumann point follows the Hugoniot-curve for the adiabatic shock (Q=0). This leads to a maximum in the pressure and density profiles, which is called the von Neumann spike, Fig.2.3. The chemical reaction takes place directly after the shock, but no energy is released until enough radicals for exothermic reactions are built up. This period, between a fluid particle passing the shock wave and reaching the energy release zone, is called the induction period τ_i. In the induction zone the thermodynamic conditions stay almost constant. Because a chain-branching reaction takes place, the induction zone has

slightly endothermic character. In the following energy release zone the radicals produced in the induction zone are combined subsequently with other intermediate species to form the combustion products. This is a highly exothermic process. The family of Hugoniot curves shown in Fig.2.3 correspond to successive fractions of reaction, Q_1 to Q_4. The induction time τ_i can be approximately described by an Arrhenius-type equation:

$$\tau_i = A_i \exp \frac{E_i}{RT} \tag{2.11}$$

where E_i is the activation energy and A_i is a parameter dependent on the mixture [SWS99]. Fig. 2.4 shows the qualitative variation of physical properties through a detonation wave. Quantitative plots, which were calculated based on a ZND code are shown in Chapter 6.

As the hot products expand, the pressure drops within the reaction zone. The coupling between the shock and the reaction zone is the premise for a self-propagating detonation wave.

2.5 Cell Structure

One-dimensional detonations propagating at near CJ velocities as shown in the ZND model are not observed experimentally. The detonation is intrinsically unstable which leads to a complex three-dimensional combination of shock waves at the detonation front. Disturbances can be caused by amplified instabilities, Fig.2.5. Shock waves traveling perpendicular to the main-flow direction are generated to level out the inhomogeneous pressure distribution along the front. A three-dimensional structure of longitudinal and transverse running shocks develops. The transverse shocks interact with themselves and the surface of the containment. This results in a system of periodic transverse waves and periodic oscillation in the leading shock strength.

A similar situation is observed for a shock wave traveling along an inclined surface, where shock is reflected in the gas behind the incident shock. If the surface is inclined at a certain angle to the flow, the intersection of incident and reflected shock leaves the surface and a third shock is created (Fig. 2.6).

This shock is known as Mach stem, which is perpendicular to the inclined surface. The connecting point of the incident, reflected shock and the Mach stem is called the triple point.

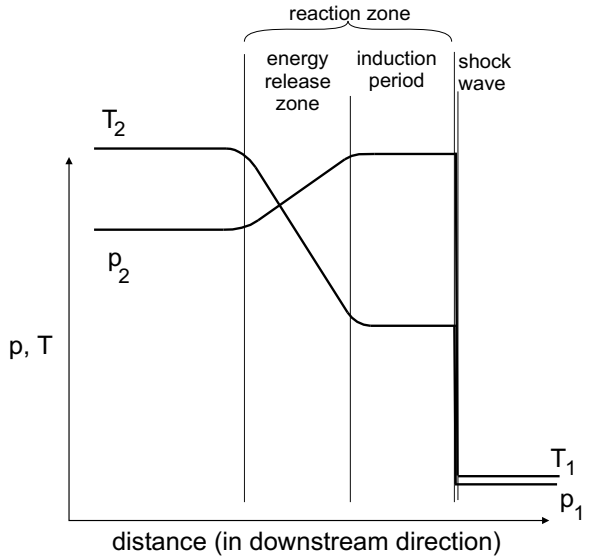

Figure 2.4: Variation of pressure and temperature through a detonation.

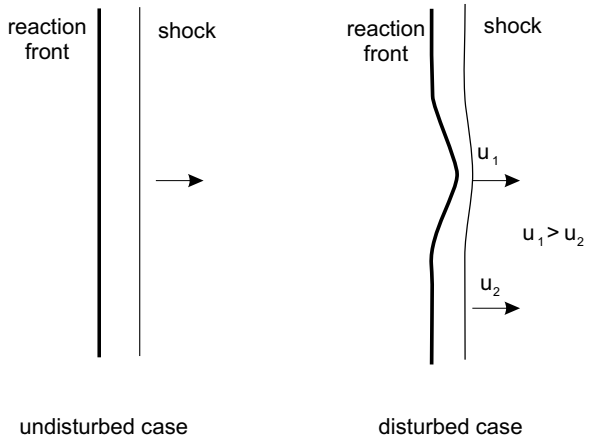

Figure 2.5: Ideal and disturbed detonation front.

These triple points, strictly speaking, are only points in a two-dimensional view. In real detonations, the shock waves are planes and so only triple lines exist. A three-dimensional detonation front consists of altering patches of incident shocks and Mach stems, which are connected by a grid of triple-lines. A schematic of the cellular structure is shown in Fig. 2.7.

A transverse wave leads back from each triple point. Two triple points moving in different directions are colliding in the apex of each cell. A Mach stem with a longitudinal velocity of up to 140% of the CJ velocity, depending on the mixture [FD79], is created. The induction

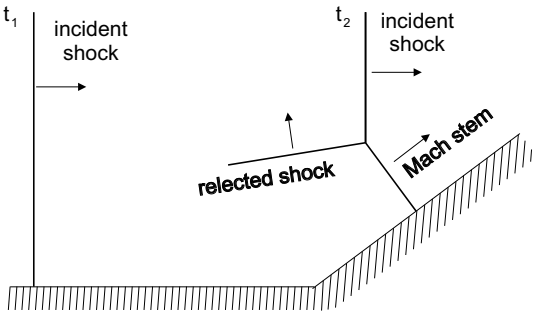

Figure 2.6: Shock reflection with formation of a Mach stem.

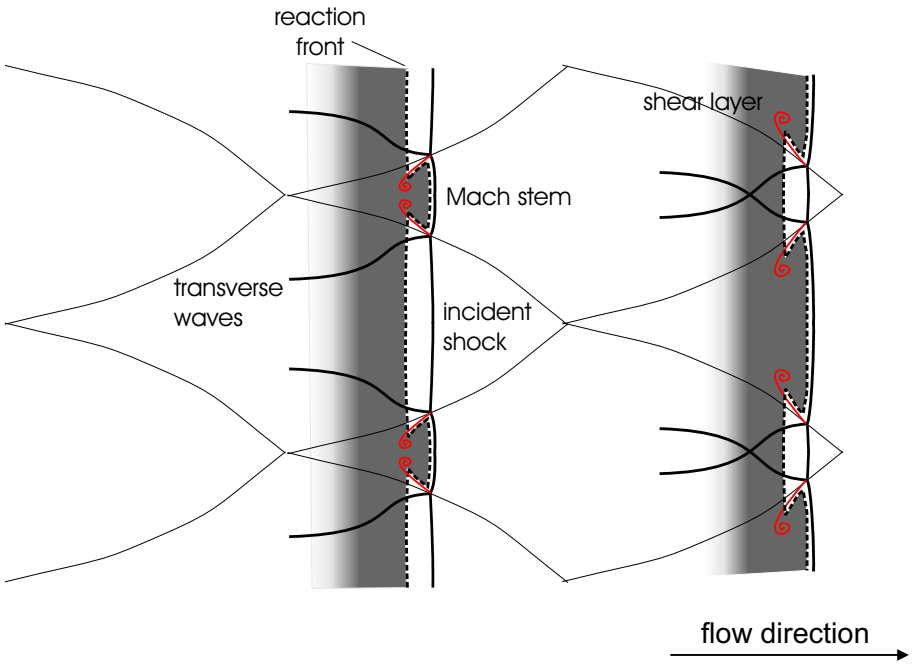

Figure 2.7: Schematic of cellular structure and its involved shock waves. The energy release region is shaded in gray.

zone length decreases strongly with increasing shock velocity. For a quantitative discussion see Section 6.6.2. Due to the high shock velocity, the induction time is very short in this stage and therefore the distance between Mach stem and reaction zone is small.

The Mach stem velocity is decreasing with time and the former Mach stem becomes an incident shock halfway through the cell. At this point shock collisions are taking place in the cells located above and below the cell under consideration. The continuous decrease in

shock velocity of the Mach stem results in a constantly rising induction period and length. The reaction front gets more and more decoupled from the incident shock. The transverse waves propagate into the induction zone and, depending on the role of the transverse wave in the specific mixture, the chemical reaction might take place significantly closer behind the transverse wave.

Near the end of the cell, the incident shock velocity reaches its minimum, which can be down to 60% [FD79] of the CJ velocity. The triple points collide at the end of a cell and the cycle begins for the next cell downstream. The propagation velocity of the detonation front is the CJ velocity only in the sense of spatial and temporal average of the CJ velocity.
The longitudinal distance between two transverse wave collisions is called the cell length l, the vertical spacing cell width λ. The cell width is also equal to the spacing of two transverse waves moving in the same direction and is an important detonation parameter [Lee84]. In the following, the term cell width and cell size are used synonymously. For detonations propagating in containments with dimensions large in comparison to the cell size, only mixture composition and the thermodynamic initial conditions determine the cell size. The triple point tracks, and so the cellular structure, can be visualized by letting the detonation travel along a sooted surface. Sootfoil records are a common technique in determining cell sizes experimentally. Even though the detailed mechanism of sootfoil records is not understood completely [SMMT86], [She99], the soot is unevenly distributed by the detonation wave in such a way that the triple point tracks are visible. One possible explanation is that the higher pressure at the triple points causes the soot to adhere to the walls, leaving darker tracks. Another theory assumes that shear layers, caused by the different flow velocities behind Mach stem and incident wave, clear away the soot in areas along the triple-point tracks. Examples of soot foil records are shown in the Appendix A.

The cellular structure observed on sootfoil records show varying regularity for different mixtures. For example Argon-diluted $2H_2$-O_2 mixtures leave a more regular cellular pattern on the sootfoils than N_2-diluted mixtures. The conditions under which a detonation has a regular structure are not completely clear. One approach explaining the different regularity is the effective activation energy. In the strong shock limit, which is a good approximation for detonation Mach numbers, the post-shock density is Mach number independent. The post-shock

temperature, in contrast, dependent on the square of the Mach number ([Sch00]). The effective activation energy parameter, is defined as:

$$\theta = \frac{E_i}{R T_{VN}} = \frac{1}{T_{VN}} \left(\frac{\ln \tau_2 - \ln \tau_1}{\frac{1}{T_2} - \frac{1}{T_1}} \right) \tag{2.12}$$

The induction times τ_1 and τ_2 of constant-volume simulations at two different temperatures T_1 and T_2 close to T_{VN} and the temperature at the von Neumann state T_{VN} have to be known. The states 1 and 2 are, e.g. in [Sch00], generated by varying the Chapman-Jouguet velocity of the shock by $\pm 1\%$. The induction time is often defined as the time corresponding to the maximum rate of OH production or temperature change. The activation parameter can be seen as an amplification factor of disturbances in reacting flows. Larger values of θ indicate a more irregular cell structure.

Simulations by Gamezo et al. [GDO99] showed that the shock velocity fluctuations in a cell increase for mixtures with higher activation energies. The wider range of velocity fluctuation and the strong dependence on temperature of the induction time may lead to a regime where the shock-induced ignition occurs more randomly. This could result in more uneven cell sizes and less regular cell structure for mixtures with higher activation energy. Other possible approaches explaining the different regularity include the influence of the heat capacity ([LOK92], [LOKvT93], [Pan97]). Due to the irregularities of the cellular structure, the experimental determination of an exact averaged cell size, λ, is difficult. Shepherd et al. [SMMT86] developed a procedure to obtain the cell size based on two-dimensional Fourier analysis of the sootfoil.

Depending on the geometry of the facility different types of cell structure can occur. Since in this thesis only detonations in a tube with square cross section are investigated, this is the only case discussed in detail. In a fully developed detonation for a square cross section, two families of transverse waves can exist which are orthogonal to each other and parallel to the walls. Waves moving along the long sidewall in rectangular channels are sometimes referred to as principal waves, those running back and forth between the side walls are sometimes referred to as slapping waves (Fig 2.8). This type of detonation is called a rectangular detonation. The triple-point attached to the principal waves leave tracks on the side walls, the slapping waves leave tracks on the top and bottom walls. The distance between two transverse waves of the same family, moving in the same direction, is equal to the cell width. The number of transverse waves of one family, called the mode number, is equal to twice the number of cells in that direction and characterizes the detonation. One mode number exists for each dimension.

In a square cross section the two mode numbers are normally equal. Fig. 2.8 shows a square 6×6 detonation (three cells in each dimension).

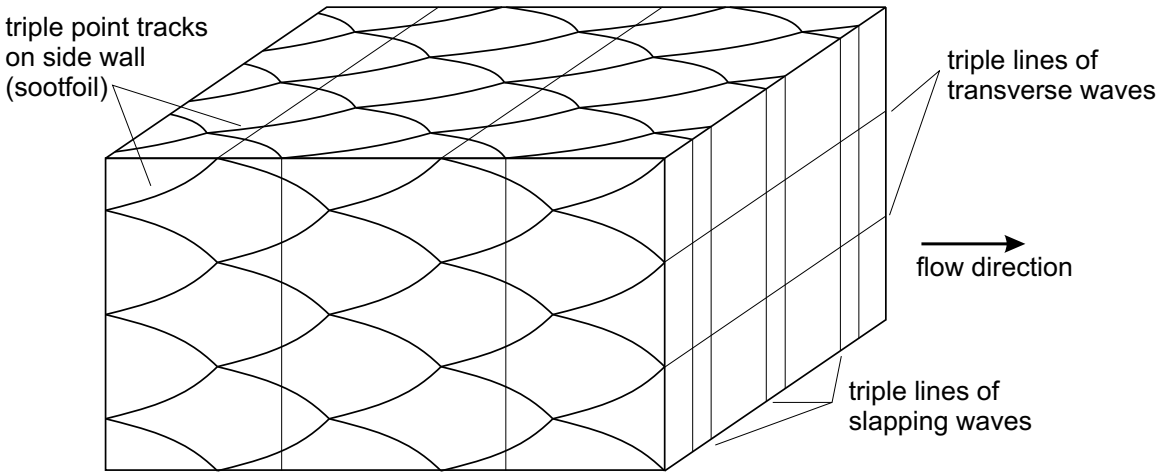

Figure 2.8: Ideal triple point tracks of a rectangular 6x6 detonation.

The angle between the triple point propagation direction and the main flow direction is called the track angle. Since the triple point is the connection point between transverse wave and main shock front (Mach stem and incident wave), it has a velocity component both perpendicular to and along the propagation direction of the detonation. The changing track within one cellular cycle indicates the variation of the incident shock strength and Mach stem strength.

In an observation frame attached to the triple point, the oncoming gas enters the incident shock as well as the Mach stem at a certain angle. Idealized stream lines through a shock configuration are illustrated in Fig. 2.9(a). The stronger the shock, the shorter the induction time. The reaction front is therefore quite close to the strong Mach stem. Fluid elements passing through the incident shock, closer to the triple point, have a shorter way to go between the incident and the transverse wave. For this reason the fluid takes a longer time to react after passing the transverse wave near C than near A. The reaction front CD is therefor inclined to the corresponding shock AC (transverse wave), Fig.2.9(a).

The slip line is the dividing line between particles having passed through the incident wave and transverse wave and particles having passed through the Mach stem. From conservation laws, the flow direction of the fluid on both sides of the slip line must be the same. The flow velocity, in contrast, must not be equivalent. Therefore, depending on the shock configuration

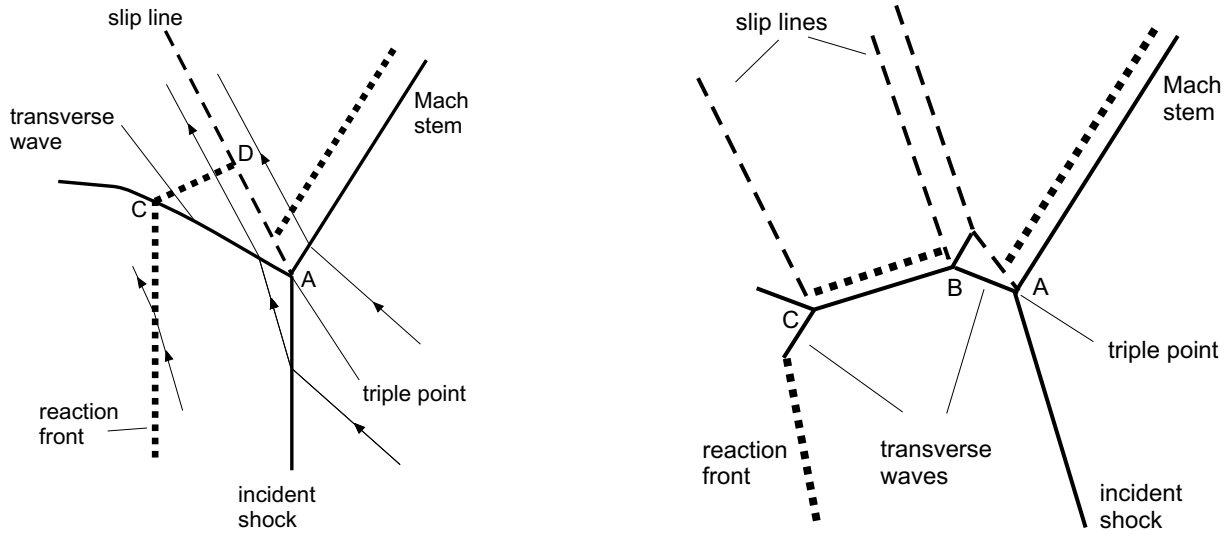

(a) View in the quasi-steady frame attached to the triple point. Weak transverse wave structure.

(b) Strong transverse wave structure with three triple points (A,B,C).

Figure 2.9: Different types of triple point structures.

and mixture, a velocity difference exists across the slip line. Due to the velocity difference in the flow on both sides, the slip line is also termed "shear layer".

Depending on the strength of the transverse wave, different triple point structures – "weak" and "strong" – are observed. For the strong structure, a second triple point exists within the induction zone (Fig. 2.9(b)). The segment BC can be reactive. Strong structures normally exhibit sootfoil patterns on which the cells are bordered by three lines. The lines are supposed to correspond to the three triple points A, B and C. The track left by A is the strongest and corresponds to the only line observed in the weak case. Marginal detonations show the stronger structure more often than do ordinary detonations ([FD79]). A marginal system, in contrast to an ordinary detonation, is one that is propagating near the detonation limit, so the cell size is on the order of the facility dimensions. Slight changes (lower pressure or smaller tube diameter) can result in failure of a marginal detonation. Marginal detonations show a bigger axial velocity variation through the cell than ordinary detonations [LWO95]. Also, the cell width of marginal detonations can be up to 2.3 times higher than the cell width measured for the same mixture in a larger diameter facility. The detonation cell width adjusts itself to the facility

dimensions in that region. A special case of marginal detonations is the spinning detonation. A detailed description of spinning detonations is found in [VMT69], [FD79] and [HLvT00].

Chapter 3

The Schlieren and Shadowgraph Technique

The schlieren technique is a non-invasive optical method used to visualize optical density gradients in transparent media. The basic principle involves the deflection of light beams at optical density gradients[1]. The schlieren technique can be applied for research in gases, liquids and solid matter and is mainly used today for scientific research, although the original application was a technical one [Toe64].

The schlieren technique is often used to investigate heat- and mass-transfer processes in gases and liquids. Due to the three-dimensionality of the investigated processes (especially if the geometry of the investigated inhomogeneity is complex), it is nearly impossible to get quantitative results about the density gradient from the schlieren image. If the geometry is known and simple (sphere, cylindrical etc.) it is possible to estimate the density gradient and get quantitative results. The disadvantage of a schlieren system is that the light beam deflections, and so the density gradients, are integrated over one dimension of the investigated volume. This is the main reason why it is so difficult to get quantitative results with the schlieren technique.

There are many different types of schlieren setups, but all are based on the same principle. Every schlieren setup consists of a light source, a schlieren head, the schlieren edge and a focusing lens. The first set up Toepler suggested is simple, and therefore useful in explaining the basic principles. The most commonly used setups are explained in Sec. 3.2.

[1] The German term "Schliere" was originally used for inhomogeneities in lenses, which are in principle optical density gradients. This technique, today called the schlieren technique, was used as early as 1864 to detect those inhomogeneities and to rate lens quality.

3.1 Basic Principle

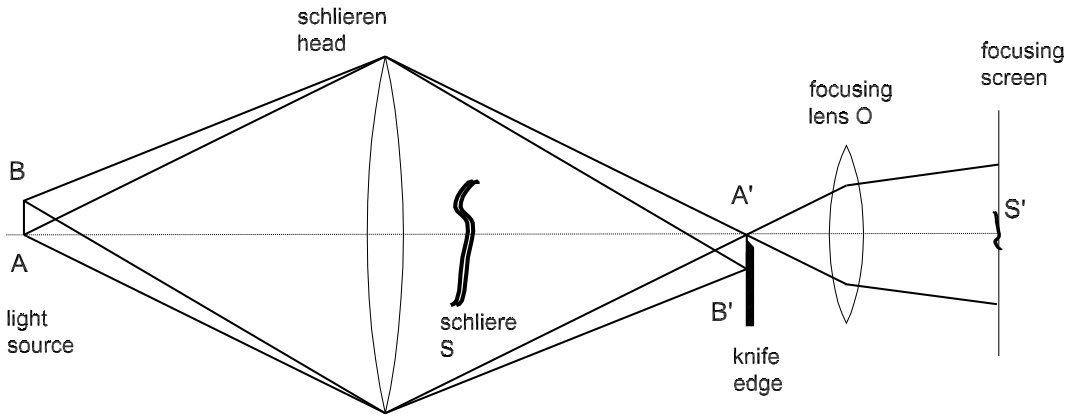

Figure 3.1: Experimental setup due to Toepler.

The light source AB of homogeneous luminosity has a sharp edge on side A (Fig. 3.1). The schlieren head, in this case a condensing lens, produces an image of the light source at A′B′, where the schlieren edge is located. The edge of the light source should be parallel to the schlieren edge and close to the optical axis. The focusing lens O is adjusted in such a way that a sharp image of the object S appears on the focusing screen.

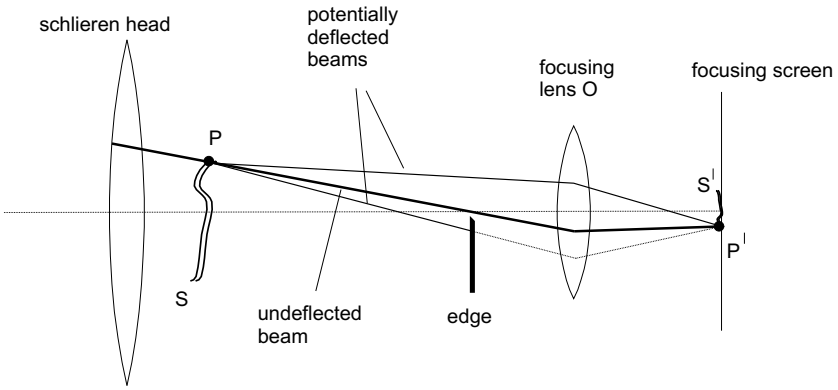

Figure 3.2: Sharp image of schliere on focusing screen.

A sharp image of the object S is obtained if every light beam sent out from a point on S is focused at the corresponding point of S′, irrespective of the original angle of the beam, Fig. 3.2.

The distance from the schlieren edge to the optical axis influences the brightness of the image

on the focusing screen. The closer the schlieren edge is to the optical axis, the more light is blocked by the schlieren edge. In this chapter, the terms optical density gradient and schliere S are used interchangeably.

An undeflected light beam, which passes the schlieren edge, and is then deflected in the schliere toward the schlieren edge, will be blocked off by the edge (Fig. 3.2). The area of that particular dot P′ will appear darker on the focusing screen. Also, a light beam blocked by the schlieren edge might be deflected in such a way passing the edge, that a brighter area will appear on the focusing screen. Deflections in both directions perpendicular to the edge can be detected. Deflections with no component perpendicular to the edge will be undetected with this setup. In this case, light beams will be displaced at A′B′ parallel to the edge, but not influenced by the edge and will remain blocked out or focused on their origin in S′. Therefore, if the schlieren edge is removed, there will be no blockage of the light beam, even when deflected, so the schliere will not be visible on the focusing screen. This fact is used to align the setup, Sec. 3.3.
Consequently, the schlieren system consists of two independent working parts. The first part, composed of the light source, schlieren head and edge, distinguishes undeflected and deflected light beams and their direction of deflection. The second part, composed of the lens and the screen, takes a sharp image by combining deflected and undeflected light beams. Deflected light beams are, in a sense, removed from the image. This is the major difference from the shadowgraph technique where deflected light beams are not removed but are relocated on the image.

3.1.1 Shadowgraphs

If the focus setting of the lens O is not exact, not every light beam emitted from point S will be focused on the corresponding point on S′. So there is no schlieren edge necessary for detecting the deflection of light beams.
Deflected light beams will simply appear slightly displaced on the screen and so create a difference in the brightness of the image. This is the classical shadowgraph technique, Fig. 3.3. The shadowgraph technique by Dvorak [Dvo80] is similar but easier to set up and simply consists of a point light source (ideal case) and a screen, Fig. 3.4.
However, unlike the schlieren technique, the images obtained by a shadowgraph system appear to be slightly fuzzy thus making a qualitative analysis difficult. Under certain conditions,

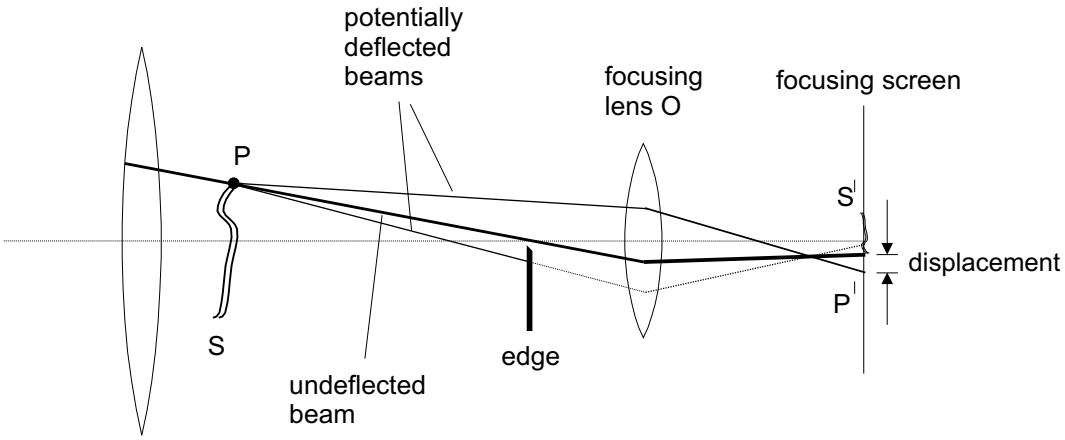

Figure 3.3: Shadowgraph: unsharp setup of schlieren system.

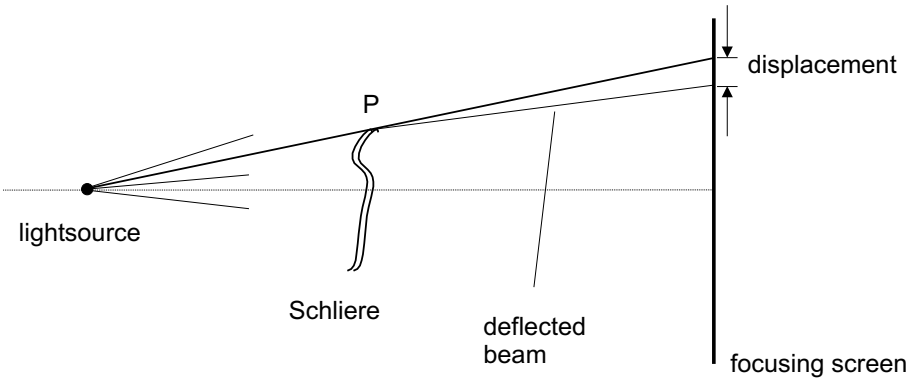

Figure 3.4: Shadowgraph by Dvorak.

in which all light beams are collected by the lenses, the shadowgraph technique detects the second derivative of the refraction index $\partial^2 n/\partial x^2$, [Sch34].

3.1.2 Refraction Index in Gases

For the refraction index n of gases a simplified relation is valid:

$$\frac{n-1}{\varrho} = const. \tag{3.1}$$

This simplified equation can be used, because in gases n is approximately 1. Since the refraction index is, with adequate accuracy, dependent only on the density, this is the state variable

directly detected by the schlieren system. At the reference state where T=273.15 K and p=1.013 bar, the refraction index of air is for example:

$$n_0 = 1.000293 \ . \tag{3.2}$$

For air, this leads to the following correlation:

$$n = 1 + (n_0 - 1)\frac{\varrho}{\varrho_0} = 1 + 0.000293\frac{\varrho}{\varrho_0} \tag{3.3}$$

where ϱ_0 stands for the density of the air in the reference state. Considering this correlation, the refraction index changes only a little with the density. If, for example, the temperature field for a constant pressure field is investigated, the equation of state can be used to calculate the density field. From the refraction index field, the light beam deflection can be always calculated, whereas the refraction index field can not always be calculated from the defection information.

3.1.3 Deflection of Light

Considering a light beam that passes an inhomogeneous medium with changing refraction index n, the light beam will follow a curve with the radius of curvature R (Fig. 3.5). The angle between the incoming light beam and the gradient is φ.

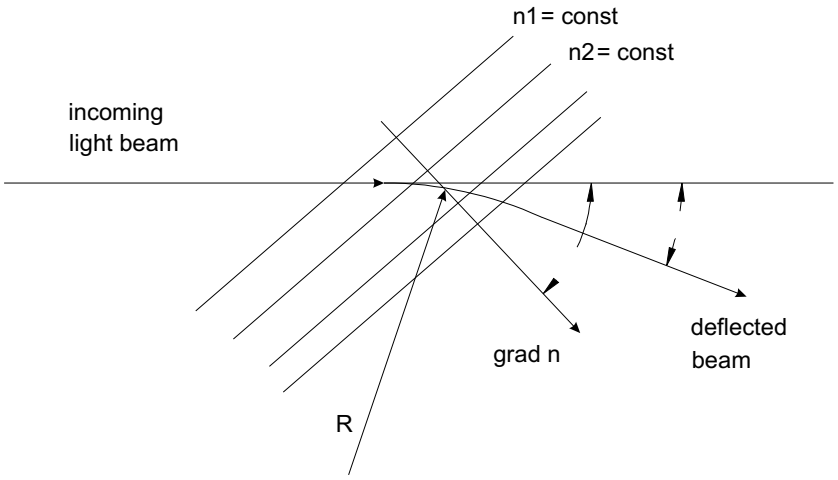

Figure 3.5: The deflection of a light beam in inhomogeneous media.

The light beam will leave the inhomogeneous area in a certain off-axis angle ϵ. With Fermat's theorem, the following expression for the radius of curvature can be derived [Sch34]:

$$\frac{1}{R} = \frac{\operatorname{grad} n}{n} \cdot \sin\varphi \tag{3.4}$$

As the angle φ approaches 0, the light beam is not deflected ($R \to \infty$). This is why the density gradient in the direction of the light beam can not be detected with the schlieren system. This equation enables the track of the bent light beam to be calculated thus predicting the behavior of the schlieren system. However, in most cases, the schlieren geometry and the density gradients are unknown, and the objective is to measure these unknown variables. From the outset it is important to note that it is impossible to draw non-ambiguous conclusions from the knowledge of the deflected light. Assumptions about the refraction index field geometry must be made to calculate the refraction index from the displacement angle and direction of a light beam.

Considering a light beam passing through a schliere, the off-axis angles ϵ_{z_0} and ϵ_{y_0} are of interest (Fig. 3.6). The angle between the gradient and the optical axis is called φ. The density gradient, $\operatorname{grad} n$, and the x-axis form a layer, called the $\eta - x$-layer, with the coordinate η perpendicular to the x-axis. This yields:

$$\eta'' = \frac{\operatorname{grad}\ n}{n} \cdot \sin\varphi \tag{3.5}$$

and

$$\begin{aligned} y'' &= \eta'' \sin\vartheta \\ z'' &= \eta'' \cos\vartheta \end{aligned} \tag{3.6}$$

where ϑ is the angle between the $\eta - x$-layer and the $z - x$-layer. Substituting η'' leads to :

$$\begin{aligned} y'' &= \frac{\operatorname{grad}\ n}{n} \cdot \sin\varphi \sin\vartheta \\ z'' &= \frac{\operatorname{grad}\ n}{n} \cdot \sin\varphi \cos\vartheta \end{aligned} \tag{3.7}$$

as shown in Fig. 3.7:

$$\begin{aligned} \operatorname{grad} n\ \sin\varphi\ \sin\vartheta &= \frac{\partial n}{\partial y} \\ \operatorname{grad} n\ \sin\varphi\ \cos\vartheta &= \frac{\partial n}{\partial z} \end{aligned} \tag{3.8}$$

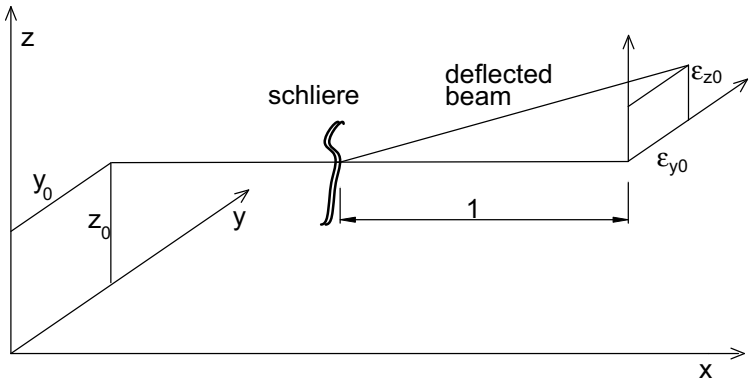

Figure 3.6: Deflection of a light beam ε_{y_0} and ε_{z_0} in radiant.

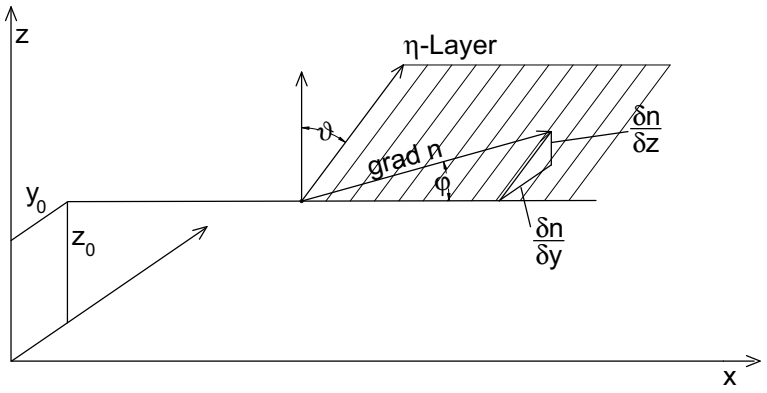

Figure 3.7: The components of grad n.

Since the difference between n and n_0 is small, for simplification n is substituted by n_0.

$$y'' = \frac{1}{n_0}\frac{\partial n}{\partial y} \tag{3.9}$$

$$z'' = \frac{1}{n_0}\frac{\partial n}{\partial z} \tag{3.10}$$

The deflection angle of a light beam in the y- and z-direction reads:

$$\varepsilon_{y_0} = \left(\frac{dy}{dx}\right)_{x_2} = \frac{1}{n_0}\int_{x_1}^{x_2}\left(\frac{\partial n}{\partial y}\right)_{x,y_o,z_o} dx$$

$$\varepsilon_{z_0} = \left(\frac{dy}{dx}\right)_{x_2} = \frac{1}{n_0}\int_{x_1}^{x_2}\left(\frac{\partial n}{\partial z}\right)_{x,y_o,z_o} dx \tag{3.11}$$

The displacement a of a light beam at the schlieren edge depends on the deflection angle ϵ and the distance s from the schliere to the schlieren edge:

$$a = \epsilon \cdot s \tag{3.12}$$

3.2 Experimental Setup

There are several types of setups which differ from each other mainly in the schlieren head, the kind of light source, and type of schlieren edge used. The diameter of the schlieren head lens used limits the field of view. Concave mirrors are used most often, since they are less expensive than lenses with the same diameter and quality. Mirrors are also free of chromatic aberrations. This topic is discussed in greater detail in Sec. 3.2.5.

3.2.1 Non-parallel Light Setups

Substituting the schlieren head lens with a concave mirror leads to the setup shown in Fig. 3.8:

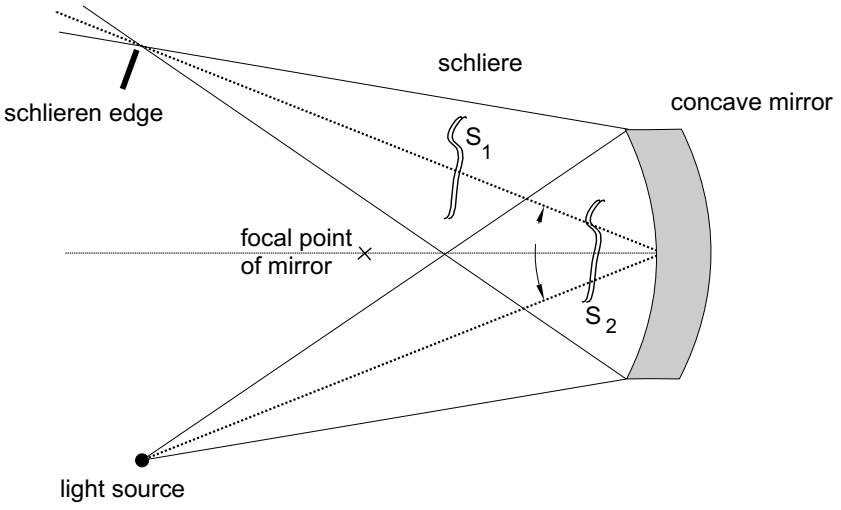

Figure 3.8: Optical setup with one concave mirror.

Neither the light source nor the schlieren edge can be placed on the optical axis of the concave mirror. There is an angle α between the incoming and the outgoing beam of the mirror.

There are, in general, two options to place the investigated volume, which are represented by the schliere S_1 and S_2 in Fig. 3.8. In the case of S_2 the light passes the schliere twice and consequently is deflected more than in the case of S_1. On the other hand, it is difficult to obtain a sharp image of S_2 since it appears twice slightly shifted on the image.
Since the optical axis of the schlieren head and the optical axis of the setup do not coincide, aberrations occur. The drawback of this particular setup is that the shadow of the light source appears in the field of view. Trying to minimize the aberration by reducing the angle between the incoming and outgoing light beams leads to the setup shown in Fig. 3.9. Since two images of the schliere are obtained, the distance from S to the mirror should be as small as possible in order to obtain a sharp image. This setup can be used if there exists only one optical access. The plane mirror in the sketch acts as a mirror and schlieren edge simultaneously. For easy alignment, it is more suitable to use a separate schlieren edge which can be adjusted independently.

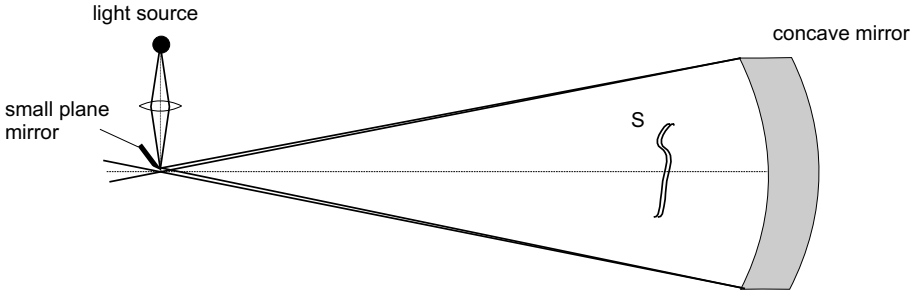

Figure 3.9: Setup to minimize the angle between the incoming and outgoing light beams.

All of the above mentioned setups are fairly inflexible in their spatial arrangements. Consequently it is not always possible to obtain a good result. For example, the concave mirror cannot be placed close enough to the schliere, or large angles between the incoming and outgoing beams increase the aberrations.

3.2.2 Parallel Light Setups

A modification of the schlieren head allows the formation of parallel light, Fig. 3.10. Substituting the lenses for concave mirrors leads to the Z-setup, Fig. 3.11. The parallel beam can be directed along any desired path with the plane mirrors. This somewhat relieves the spacial arrangement difficulties and gives a more compact setup. The schlieren head consists of two

concave lenses or mirrors. The light source is placed at the front focal point of the first lens. This results in a parallel light beam if the light source has small dimensions.

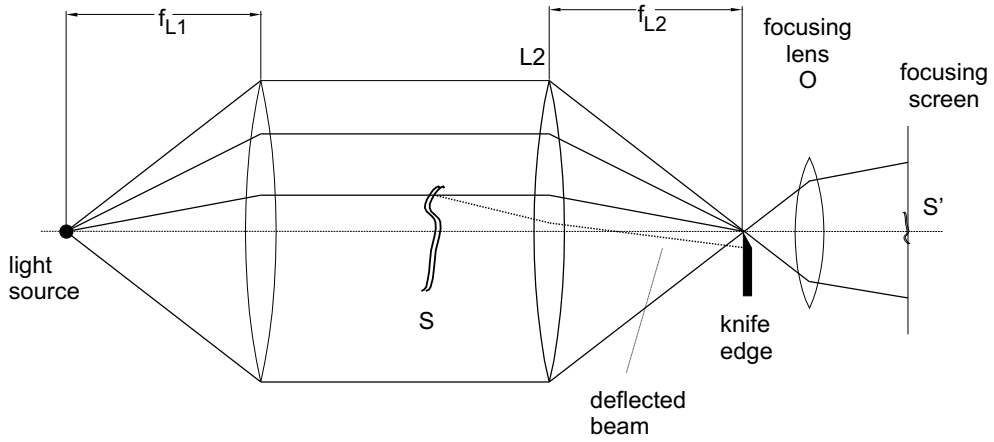

Figure 3.10: Parallel light setup using two lenses as schlieren head.

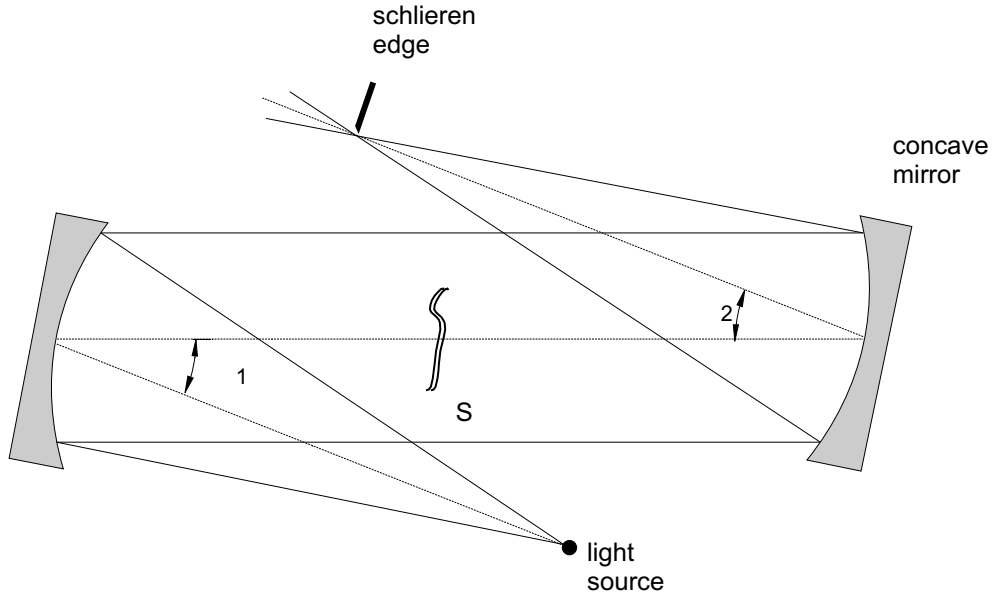

Figure 3.11: Z-setup: Parallel light setup using two concave mirrors as schlieren head.

The parallel light beam passes the schliere and is collimated by the second lens of the schlieren head, Fig. 3.10. In an ideal case an image of the light source appears in the focus point of L2. The schlieren edge is positioned at the point of the light source image. If a light beam is deflected in the schliere it is not focused in the image of the light source. Depending on the direction of deflection, the displacement at the schlieren edge is toward or away from it, and is

so blocked out or not. The lens system L2 and O image the object S on the focusing screen. The dimensions of the focusing screen are given by the dimensions of the camera CCD chip. In calculating the focal length f_O of lens O, one must consider that the lens L2 of the schlieren head produces an intermediate image S′ of the schliere. The lens O focuses that intermediate image on the CCD chip.

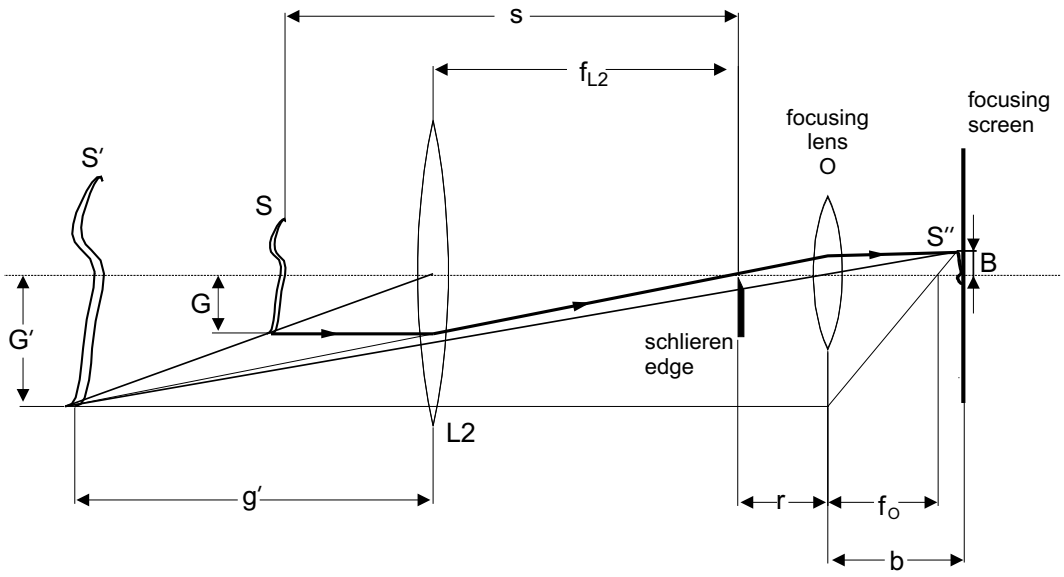

Figure 3.12: Intermediate image of schliere due to schlieren head. g' is negative in this case.

The focal length f_{L2} of the lens L2, the distance of the schliere to the edge s, the maximum size G of the schliere and the size B of the camera's CCD-chip are taken as given, Fig. 3.12. Through the fundamental optics equation, the image distance g' of the schliere S' reads:

$$g' = \frac{f_{L2}}{s - 2f_{L2}} \cdot (s - f_{L2})\,. \tag{3.13}$$

If $|s| \leq 2f_{L2}$ the image will be virtual and so on the left side of lens L2. The calculated image distance $g'$is also negative, Fig. 3.12. The image height G' can be calculated by:

$$G' = \frac{f_{L2}}{s - 2f_{L2}} \cdot G\,. \tag{3.14}$$

The distance b from the lens O to the focusing screen can be calculated (Note: g' and G' are negative in Fig. 3.12).

$$b = \frac{B}{-G'} \cdot (-g' + r + f_{L2}) = \frac{B \cdot ({f_{L2}}^2 + 2\,f_{L2}\,r - s\,r)}{2\,B f_{L2} + f_{L2}\,G - Bs} \tag{3.15}$$

The focal length of lens O can then be calculated by

$$f_O = \frac{b\,(-g' + f_{L2} + r)}{b + (-g' + f_{L2} + r)} \tag{3.16}$$

This enables the calculation of the focal length of lens O for a given camera chip dimension. The dimension r depends on the illumination diameter of lens O and can often be neglected in favor of f_{L2}. In the case where $|s| \geq 2f_{L2}$ a real image of the schliere S will appear. By choosing a certain distance s the lens O can be eliminated. In this case, the lens L2 focuses the object S directly on the CCD chip.

3.2.3 Light Source

In most setups, a white light source, such as a halogen lamp or a mercury-discharge lamp, is used. A spark light (nano-light) sometimes leads to problems because the spark is at a slightly different location each time. This displacement results in different levels of brightness for each image and can be disturbing for high-speed camera applications. It is difficult to unify a small extension and a homogeneous brightness in one light source. So, often an image of the light source is created by a condensing lens and then limited by an aperture. If we consider a light source with diameter AB and a condenser lens C, the aperture should be placed in the area within the tetragon $MANB$, Fig. 3.13.

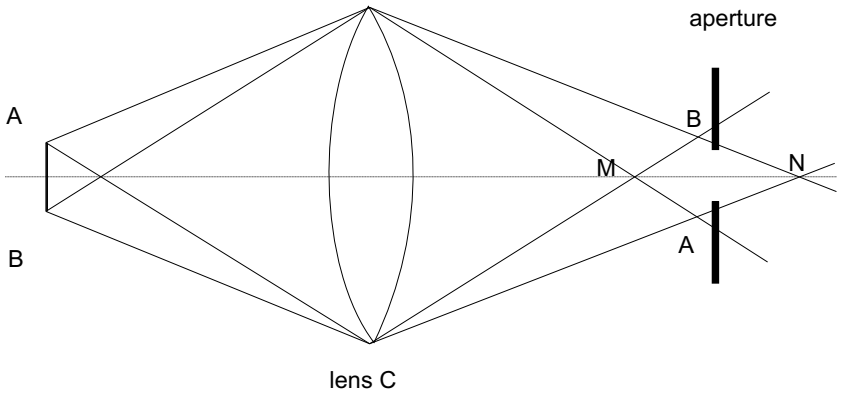

Figure 3.13: Intermediate image of light source and aperture

Depending on the focal length and the distance between the light source and the lens, the light source can be enlarged or scaled down. Minimizing the image size of the light source in order

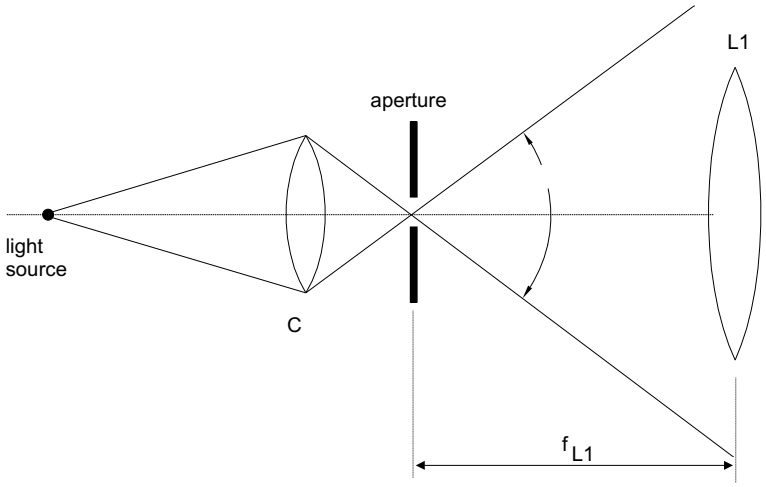

Figure 3.14: Influence of the image size on the illumination.

to get a small bright spot will not lead to sufficient illumination of the field of view for the following reasons: In order to get a small image of the light source, the distance between lens C and the light source must be increased. The greater this distance, the smaller the steradian of the light cone illuminating lens C. The illumination intensity decreases with the square of the distance. Another reason for insufficient illumination of the field of view is the low illumination of the lenses of the schlieren head. The distance from the aperture to the lens L1 is determined by the focal length of L1, Fig. 3.14. A smaller image size results in a bigger angle φ, which lowers the illumination of L1, and so the brightness of the whole image. A compromise must be found for the illumination of the two lenses and the size of the aperture. A large lens diameter of lens C is inalienable. The influences of the lens quality on the setup are discussed in Sec. 3.2.5. A small extension of the light source is desirable in order to have a sensitive setup.

The decision about the light source also depends on the amount of chemiluminescence of the investigated process, the sensitivity of the camera system and the time scale of the investigated process. For camera systems with high photosensitivity, the brightness of the light source might be orders of magnitude smaller than when using a Polaroid as a focusing screen. The shorter the time scale of the phenomenon to be investigated, the shorter the exposure time has to be, otherwise motion blur occurs. To allow a maximum blurring of 1mm (object height) in the schlieren image, the exposure time is only 1 μs assuming a velocity of 1000 m/s for the investigated process. For that reason studying steady-state phenomena is less challenging in

terms of the light-source.

Some camera systems are unable to shutter fast enough. There are twopossible methods to achieve a quick shutter. One is to use a image-gain controller. This instrument is able to shutter faster than normal cameras. However, the setup is more complicated and more difficult to adjust. Furthermore, the resolution of the image-gain-controller, in comparison to that of the camera, must be considered. The other, more commonly used possibility involves shuttering the light source. A laser is an example of a light source that is relatively easy to shutter. The small dimension of the light source is here given by the Gauss profile. A laser beam can be shuttered internally (pulsed) or shuttered externally (laser continuously working). Pulsed lasers normally have a pulse rate that is too low to obtain several frames of a fast moving process, such as detonations. Therefore, they are used in the single-shot-mode.

For high-speed applications, continuously working lasers, like HeNe lasers and Ar-ion lasers, are normally used to record a sequence. They can be shuttered by an AOM (acousto-optical modulator), which consists of a fast switching grid. The grid stands in for a multi-slit aperture, which yields, depending on the grid-state, a defraction pattern behind the AOM. By selecting the first order pattern by an aperture the laser can be shuttered. This results in a loss of intensity since the other patterns are blocked out. The loss can be minimized by turning the AOM slightly off axis.

In order to use the laser as a light source, it is necessary to expand the beam. This is done by a collimating lens with a very short focal length (glass sphere). The incoming light beam is parallel and so it is possible to set the illumination of the schlieren head-lens with the focal length of the glass sphere. Depending on the quality of the mirrors, use of a laser as the light source leads to an interferometry pattern which might be distracting in the background. To avoid this, the surface quality of the mirrors should be at least $\frac{\lambda}{8}$, where λ is the wave-length of the laser in use. The major advantage of using monochromatic light sources (e.g. lasers) is that in contrast to white light, filters can be used, which minimize the influence of light emitted out by other light sources in the room or the investigated process itself (e.g. flame).

3.2.4 Schlieren Edge

Different methods and schlieren edges can be applied to detect the displacement of a light beam at the schlieren edge. Schlieren edge stands here not only for the classical knife edge, but also for other devices, which are explained further on. The direction and the magnitude of deflection are of interest. Neither the direction nor the deflection can be quantitatively determined when using a classical knife edge as schlieren edge. If areas with the same brightness appear on the image, it just means that the light beam was deflected with equal components perpendicular to the edge. A small deflection perpendicular to the edge will result in the same brightness as a large deflection with just a small component perpendicular to the edge, Fig. 3.15.

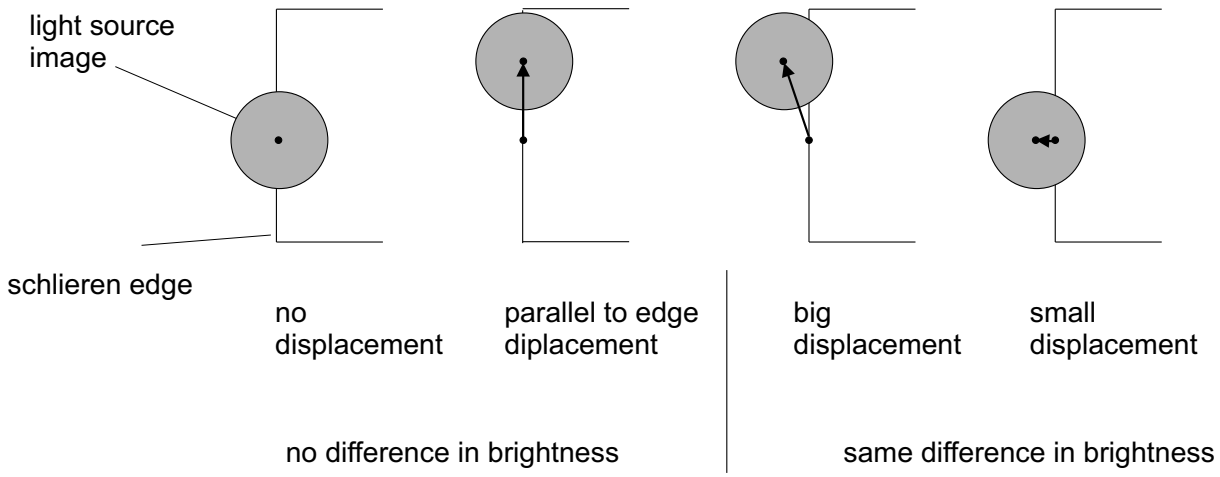

Figure 3.15: Different types of deflections and their affect on the schlieren image.

One method to detect the magnitude of deflection in all directions, regardless of the angle, is to have an aperture (iris) as a schlieren edge. This yields an image with a dark schliere on a bright background. The other possible method is to block out the undeflected light with a small disk (slide with a black dot). In this case, the schliere will appear white on a black background (dark-field technique). For these kinds of edges, the magnitude is known, but the information about the direction of the deflection is lost. A certain maximum displacement exists which can be detected quantitatively with such edges. Displacements over that maximum appear in the same brightness or darkness as that maximum. This occurs if the light source image is completely covered by the schlieren edge.

For larger deflections, another type of technique exists, which is applicable if the light source image is small in comparison to the displacement. This technique is normally used with the parallel light setup, since in this case, a light source with a small spatial extension is required. To distinguish the different directions and magnitudes of displacements at the schlieren edge, different types of gray keys and color slides can be used. The use of white light is a prerequisite for the color schlieren slide. The deflected beam takes on the color corresponding to the displacement on the color slide (schlieren edge), or correctly, all other wavelengths in the white light are filtered out. The color schlieren has the advantage of being able to detect magnitude and direction independently. Hence, two independent coding variables must exist in the schlieren edge. Since the direction is given by an angle, and the magnitude by the distance from the center, it is appropriate to use a polar coordinate system. For example different color segments can be placed over the circumference to obtain the direction of deflection. The magnitude can be detected by a difference in brightness along the radius, Fig. 3.16.

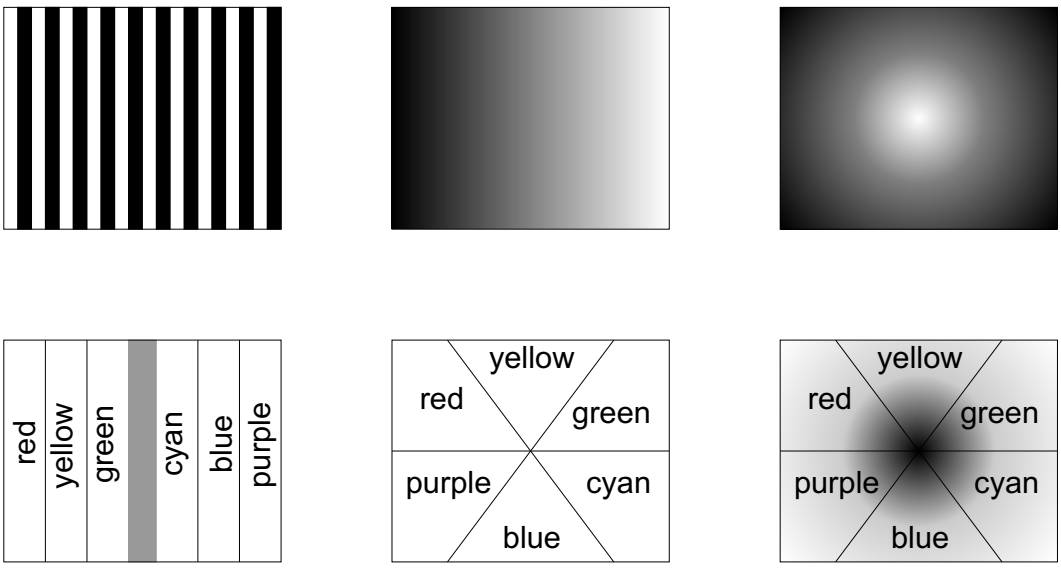

Figure 3.16: Different types of schlieren edges slides.

If the image is not bright enough and a one-dimensional coded schlieren edge (e.g. stripes, knife edge) is in use, it is helpful to change the aperture of the light source from round to rectangular. For example, it is functional to align the spark gap parallel to the schlieren edge when using a spark lamp as light source. It is only important to limit the light source in the direction of the deflection to be detected. The light source dimension can not be enlarged as

desired, since the sensitivity of the setup suffers and aberrations become too large.

3.2.5 Aberrations

Every lens system is affected by aberration. Depending on the setup and the alignment of a system, aberrations, or at least their influence on the resulting image, can be minimized. The index of refraction of a material is a function of wavelength, known as dispersion. Therefore, different light cones appear for each wavelength if white light passes through a lens, Fig. 3.14. Special lenses, so called doublets, made out of two materials with different refraction indices, can minimize that effect, which can result in color rims in the image. Also note that chromatic aberrations increase with increasing illumination of the lens.

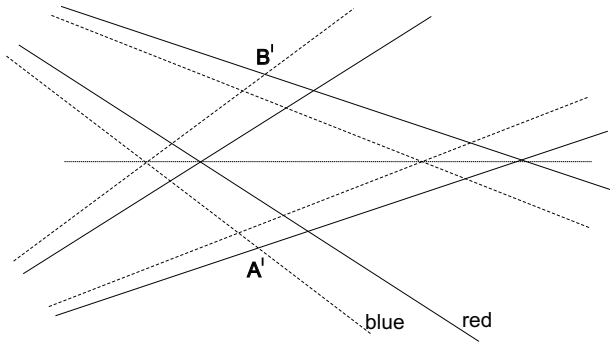

Figure 3.17: Influence of chromatic aberrations on the light source image A′B′.

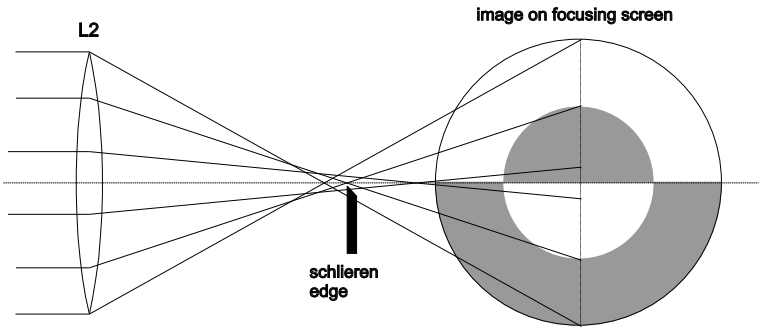

Figure 3.18: Influence of spherical aberrations on the schlieren head.

In a setup with non-corrected lenses for the schlieren head, spherical aberration also appears.

Spherical aberration decreases with decreasing illuminated lens diameter. However, in order to obtain a large field of view, the schlieren head lenses are often illuminated over the whole diameter. If plain convex lenses are used, L_1 should be placed with the plane side toward the light source and L_2 the other way around. By doing this, the light will be deflected on each side of the lens. This minimizes the aberration. The lenses should be spherically and chromatically corrected when white light is used and small deflections are to be detected. When not using corrected lenses, the background might not be of homogeneous luminosity. The spherical aberration results in a black semi-disc (Fig. 3.18), the chromatic abberation in the red and violet half of the background.

The advantage of concave mirrors is that they are more economical (especially in the case of larger diameters) and are free from chromatic errors since the reflection angle is independent of the wavelength. The spherical aberration can be corrected using a parabolic concave mirror. The major disadvantage of mirrors is that they are set up in such a way that the mirror axis does not coincide with the optical axis of the setup. A setup including semi permeable mirrors avoids this problem, Fig. 3.19. As the light beam passes the semi-permeable mirrors and is reflected by them twice, the luminosity of the image is not as high as with the conventional Z setup. The angle α in the Z setup (Fig. 3.11, p.25) causes an error that is known as astigmatism. As shown in Fig. 3.20, this occurs if an off-axis light beam is focused by a lens or mirror.

The natural asymmetry leads to this astigmatism. The plane containing both optical axis and object point is called the tangential plane. The principal ray goes from the object through to the middle of the lens. The plane perpendicular to the tangential plane which contains the principal ray is called the sagittal plane. The bigger the angle α between the optical axis and the principal ray, the bigger is the error that occurs. Besides minimizing these angles, we also have to consider whether to place the light source and edge on the same side or on opposite sides of the line between the two mirror centers (Z-setup or Δ-shaped setup). It is impossible to compensate for the astigmatism completely. However, by choosing the same angles for α_1 and α_2 at each mirror and placing the light source and edge on opposite sides (Z-setup), the asymmetry in the tangential plane vanishes. The Z-setup is therefore preferable, especially when a very sensitive setup is desired. The sagittal and tangential foci still remain, but the

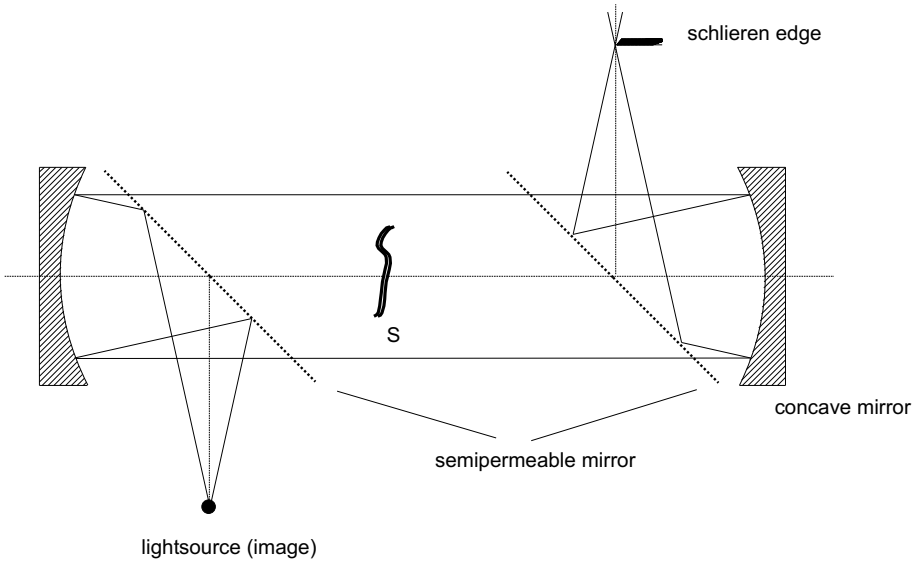

Figure 3.19: Setup with no astigmatism due to two semi-permeable mirrors.

distortion of the light source image is symmetric and one-dimensional in the foci points. The edge is placed on the tangential or sagittal focal line, depending on which deflection direction is to be visualized.

A plane mirror alternates the sides of the parallel beam, and so for a correct Z-setup it looks like the light source and edge are placed on the same side. A relatively easy method to check a setup with an even number of plane mirrors in the parallel light beam is described as follows: When looking from behind the concave mirrors the incoming light beam has to come from different sides (left/right) for each concave mirror. When using an odd number of plane mirrors in the parallel light beam, the light beam should enter from the same side.

3.2.6 Sensitivity of the Setup

The sensitivity is defined here as the smallest deflection that can be visualized. As shown earlier, for a system not involving parallel light beams, the sensitivity depends on the distance s from the schliere to the edge and the distance of the edge from the optical axis, Fig 3.1.

$$\varepsilon_m = \frac{a}{s}\,\alpha \tag{3.17}$$

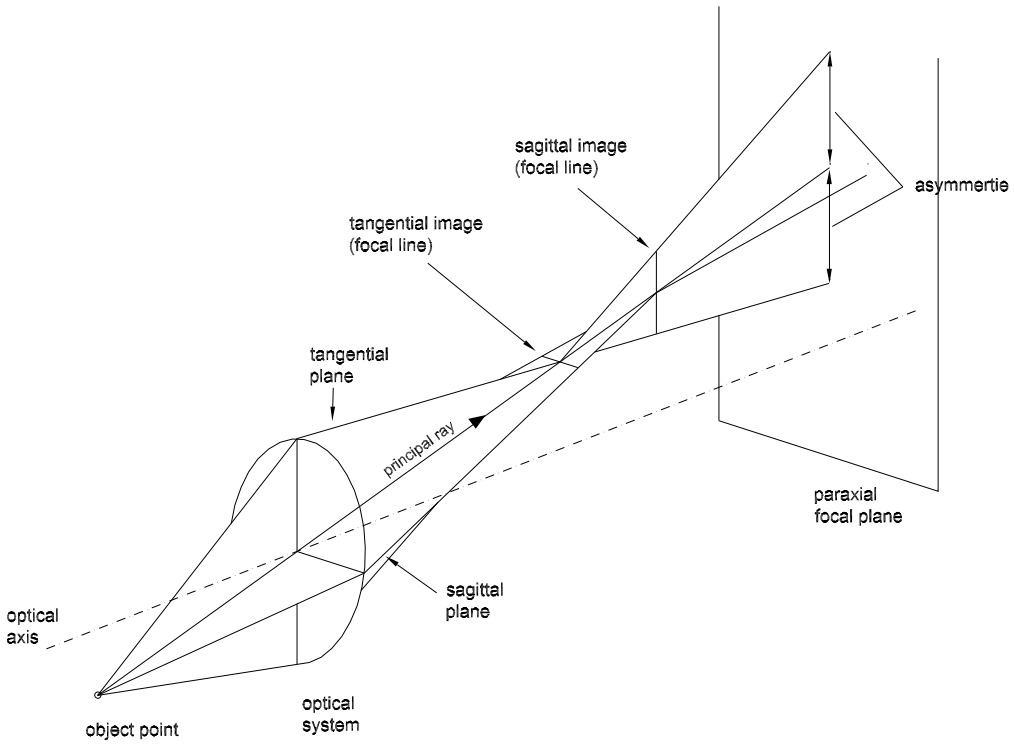

Figure 3.20: Astigmatism represented by sectional view.

ε_m is the smallest detectable angle and α is the smallest discernible difference in brightness. The sensitivity increases with the distance s and also with proximity of the edge to the axis. Theoretically the sensitivity reaches infinity for $a \to 0$. In the experimental setup the sensitivity is limited by the necessary general brightness of the image, the aberrations and the defraction at the edge. Defraction is also responsible for the white rim around the object in the field of view. These white rims appear mainly on edges parallel to the schlieren edge.

For a setup with parallel light (Z-setup), the displacement of a beam at the schlieren edge is calculated differently. Illustrated in Fig. 3.21 is the case where the distance s_k from the schliere to the second lens of the schlieren head is larger than the focal length f of that lens. The derived formulae are valid for any distance.

The image distance is:

$$s'_k = \frac{s_k\, f}{s_k - f}\ , \tag{3.18}$$

and the displacement a at the edge (Fig. 3.21):

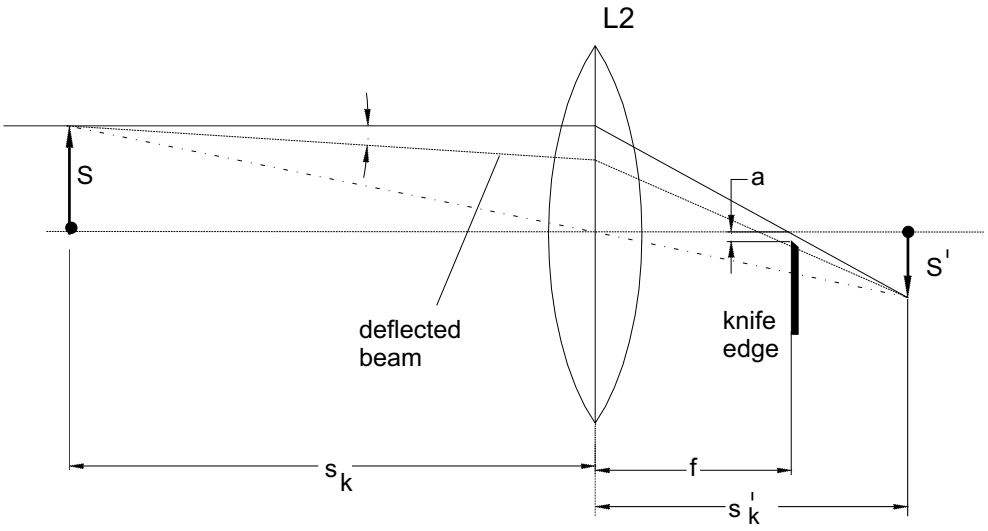

Figure 3.21: Displacement of deflected beam in parallel light setup.

$$a = \frac{\varepsilon s_k \cdot (s'_k - f_{L2})}{s'_k} = \frac{\varepsilon s_k \cdot (\frac{s_k f_{L2}}{s_k - f_{L2}} - f_{L2})}{\frac{s_k f_{L2}}{s_k - f_{L2}}} = \varepsilon f_{L2} \ . \tag{3.19}$$

The displacement is therefore independent of the distance s_k from the concave mirror to the schliere. The sensitivity for that setup is calculated as:

$$\varepsilon_m = \frac{a}{f_{L2}} \alpha \tag{3.20}$$

This calculation is based on the assumption that all of the beam deflections are fairly small and are not blocked by the lens and mirror holders. The aberrations for the outer regions of the lenses and mirrors are also assumed to be insignificant.

3.3 Alignment of Schlieren Setup

Good alignment of the setup is of great importance for the quality of the results. The alignment process and techniques will be discussed in this section. It is worth noting that misalignment can also be caused by temperature changes, vibration, or the creeping of material.

To attain good alignment results the components should be placed on optical benches. The light source, the condensing lens C and the aperture should be placed on one bench. The

schlieren edge, the imaging lens and the camera on another bench. Lenses used for the schlieren head should be placed on the benches as well. The optical bench is especially useful if exactly aligned along the optical axis, as this enables one to adjust the distance of the components without displacing the center of the optical axis. To minimize aberration, lenses and mirrors should always be illuminated exactly in the center. There are different techniques for aligning setups with mirrors than for those involving only lenses. For lenses, one can use the reflection from both surfaces of a lens. This is described in greater detail in Sec. 4.5 for the alignment of a laser light sheet. A common Z-setup with two plane mirrors in the parallel light beam, as used in the experiment, is discussed in this section.

A low-power laser or laser pointer is helpful for the alignment process. First the optical benches and mirrors have to be aligned. All other components (lenses, edges) have to be removed. The alignment laser is then placed on the front of the optical bench containing the light source and is leveled and aligned with the bench. To check this, another aperture can be slid along the benches. Using targets for the concave mirrors ensures that they are illuminated in the center [2]. The optical axis of the whole setup must be in one layer. Therefore, it can be checked whether the unexpanded laser beam coincides wherever the path crosses itself. To avoid asymmetry (Sec. 3.2.5), the angles of the incoming and outgoing beam have to be identical for both mirrors. To verify this, the displacement of the reflected and incoming beam can be measured at a certain distance from both mirrors and compared. Before removing the laser, the position of the optical axis (laser beam) has to be marked. This can be done by placing two small apertures on the optical bench, through which the laser light passes.

The alignment laser can then be substituted with the light source. The light source can be adjusted in such a way that the light passes both apertures. The smaller the apertures, the more precise the placement of the light source will be. Sliding the light source along the bench should not change the path of the passing light beam. The aperture for limiting the light source image can then be placed in the same way. Finally, the lens can be placed to finish the alignment on the optical bench side. To ensure that the condenser lens is located with the center on the optical axis, it can be placed in between the apertures. If the lens is correctly positioned the light will pass through both apertures. This should not alter when sliding the

[2] A paper with a small hole in the middle placed on the mirror is sufficient.

aperture and lenses along the bench. This particular way of alignment has the major advantage of being able to vary the distance of all optical components on the optical benches easily, without changing the optical axis. This helps when optimizing the alignment and focusing the image. The aperture for limiting the light source image can be placed in the focal point of the first mirror. The correct distance can be tested by measuring the diameter of the parallel light beam after it has traveled for a few meters and correcting if it is diverging or converging. If the light beam is diverging the aperture is placed too close to the mirror. The distances of the light source and the lens have to be adjusted following the earlier discussion in Sec. 3.2.3.

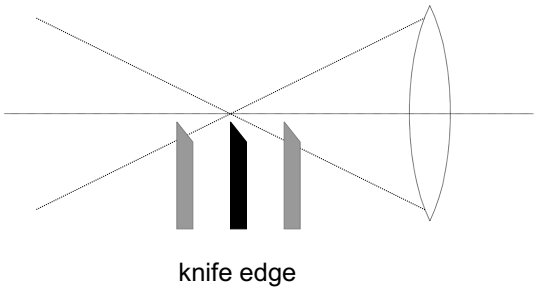

Figure 3.22: Positions of the schlieren edge; the middle one is correct.

The next items to be positioned are the camera and the focusing lens O. The camera (CCD chip) must be perpendicular to the optical axis. Otherwise the distance from CCD chip to lens changes along the CCD chip and it is impossible to get a sharp image all over the field of view. In order to get a sharp image it is helpful if either the lens or the camera is placed on a translation stage. A transparent target, for example a printed slide, can be placed in the layer, where the schliere will appear. Another method is to produce a density gradient[3] and adjust the lens so that no density gradients are visible on the image. Since the schlieren edge is not yet placed, that indicates that a sharp image of that layer is given on the CCD chip. Sometimes it is difficult and inconvenient to place a target in the layer the schliere will appear. It is also possible to get a sharp image by placing the target one time equidistant in front of and one time behind the imaging plane and by then positioning the lens in the middle of these two corresponding positions. A scale on the translation stage is then helpful. This is not exactly accurate but it gives a sufficiently good result. The same can be done by placing the candle light in front of and behind the investigated

[3]e.g. the hot air rising from a candle flame

phenomenon. If adjusted correctly, the hot rising air is not visible on the image. Every density gradient visible at this stage is shadowgraph but not schlieren and will not lead to a crisp image.

Finally the schlieren edge is to be positioned. The schlieren edge has to be placed on a translation stage, which is adjustable perpendicular to the optical axis. If it is placed correctly in the direction of the optical axis, the image should become homogeneously darker when the schlieren edge slowly moves towards the axis. If the darkness appears on one side first, the position along the axis has to be changed.
If, following that, the darkness appears from the other side, the correct position is somewhere in between these two positions. The same procedure can be used for color schlieren edges. Depending on the position of the schlieren edge with respect to the focal point, the sensitivity of the setup can be influenced. The closer the schlieren edge is placed to the focal point, the more sensitive the setup. If the schlieren edge overlaps the focal point of the light source, so that the background illumination of the image is reduced, density gradients will appear as regions of levels of both higher and lower luminosity.

Chapter 4

Laser Induced Fluorescence

One major advantage of most of the laser diagnostics is that unlike the schlieren technique the thermodynamic and chemical properties measured, are not necessarily integrated over a whole volume. Measurements can be obtained along a line or over a certain plane of the region of interest. These "cuts" through the volume give information about the three-dimensional field properties. Another advantage is that laser diagnostics can be selective to certain species involved in the process.

4.1 Classification of Laser Diagnostics

All laser diagnostic methods depend on the interaction between the laser light and the particles or molecules hit by the laser beam. The signals can be detected with a spectrometer resolving the intensities of the different wavelengths of the signal, or with a camera which integrates over a certain wavelength area (adjustable with filters). Two different types of signal beams are possible: incoherent and coherent.

For coherent diagnostic approaches the signal beam is coherent with the incident laser beam. A stronger signal is normally possible than with incoherent approaches. The signal results in a laser-like beam and therefore the majority of the emitted signal can be detected. An example of the coherent technique is the Coherent Anti-Stokes Raman Spectroscopy (CARS) [Eck96]. The setup is normally more complex in comparison to an incoherent approach.

In an incoherent scattering process the signal is sent out from every point of the excited volume in every direction. For this reason it is only possible to detect a certain part of the signal. The laser beam propagates through the medium and generates a signal source along that pass. The

signal is detected at a certain angle to the incident beam (often 90°) over some solid angle Ω. Hence the detected part p of the whole signal is:

$$p = \frac{\Omega}{4\pi} \ . \tag{4.1}$$

By using back-scattering techniques, sometimes one optical access is sufficient. Another advantage of incoherent approaches is that two dimensional measurements can be made. In this case a whole plane in the volume has to be excited. This is done by a laser light sheet. Examples for incoherent approaches are Raman Scattering and Laser Induced Fluorescence (LIF).
The incoherent approaches can be classified as *absorbtion*, *elastic scattering* or *inelastic scattering* techniques.
Absorption techniques are very sensitive but provide measurements averaged over a path and are not strictly point measurements. The radiation emitted by a radiation source towards a detector (e.g. spectrometer) is absorbed in certain wavelength regions along its way to the detector.
In an *elastic scattering* process the frequency of the incoming and scattered light is the same. There is no energy exchange between the incident photons and the molecules. Examples are Rayleigh scattering, where the particle diameter d is small in comparison to the wavelength λ and Mie scattering ($\lambda \ll d$) [Eck96]. The strength of the Rayleigh scattered light is proportional to the fourth power of the light-frequency but independent of the species.
In an *inelastic scattering* process the scattered light is shifted from its incident frequency. The two main techniques are Raman scattering and Fluorescence. Raman scattering can be rotational, vibrational or electronic, depending on the energy exchange between the molecules and the incident light quanta. Fluorescence is a two step process. First the molecule has to get into an excited state. The pumping in the excited state can be reached by electron bombardment, heating, chemical reaction (chemiluminescence) or photon absorption. The second step is the spontaneous emission process detected as the signal, which is only one of the pathways of energy loss available. This is discussed in more detail in sec. 4.3.

4.2 Background Physics

The photon is the quantum of radiation energy. The amount of energy can only reach discrete values and varies in units of $h\nu$, where ν is the frequency of the emitted light and h is Planck's

constant.

$$E = h \cdot \nu \tag{4.2}$$

Radiation is the result of the downward transition of electrons from one energy state to another.

4.2.1 Quantum Numbers

An electron bound to an atom can be characterized by three quantum numbers: The principal quantum number n, the azimuthal or orbital angular momentum quantum number l and the spin quantum number s. The total angular momentum, $\vec{j}$ is given by the sum of the orbital momentum and spin vector $\vec{l} + \vec{s}$. Different electron configurations possess different amounts of energy. A change of configuration results in a change in energy and so in absorption or emission processes. Planck's law connects the different energy amounts with an optical frequency. E_n and E_m are the energies possessed by the atom in configuration n and m respectively.

$$\Delta E = E_n - E_m = h \cdot \nu \tag{4.3}$$

For multiple electron systems each electron has its own momentum $\vec{l_i}$ and $\vec{s_i}$. The resultant orbital angular momentum, denoted by $\vec{L}$ and the resultant total spin, $\vec{S}$, is the sum of the corresponding vectors of each electron. Knowing $\vec{L}$ and $\vec{S}$, the total angular momentum $\vec{J}$ can be calculated as the sum of both.

4.2.2 Selection Rules

Transitions do not occur between all possible states. Certain selection rules exist which can be derived quantum-mechanically and give the allowed changes in certain quantum numbers. There is for example no restriction for the principal quantum number, but for the resultant orbital angular momentum.

· Principal quantum number, n	Δn - no restriction
· Total orbital angular momentum, L	$\Delta L = 0, \pm 1$
· Electron orbital angular momentum, l	$\Delta l = \pm 1$
· Total angular momentum, J	$\Delta J = 0, \pm 1; (J = 0 \rightarrow J = 0)$ forbidden
· Total spin, S	$\Delta S = 0$

4.2.3 Molecular Spectroscopy

Molecules have, in contrast to atoms, the capacity to rotate and to vibrate. There are three modes of excitation: *electronic*, *rotational* and *vibrational*. The system becomes more complex but is basically based on the same principles as the system discussed before. For a multi-electron diatomic system a corresponding total electronic orbital angular momentum quantum number Λ and resultant spin S is defined. The quantum number Λ is the sum of the projections of the orbital angular momentum in the line connecting the atoms. The most important selection rules for transitions are:

- electronic orbital angular momentum quantum number , Λ $\quad \Delta\Lambda = 0, \pm 1$
- resultant spin , S $\quad \Delta S = 0$

Based on these selection rules certain transitions are preferred and have so a higher transition probability.

4.2.4 Line shapes

Since only discrete energy levels exist, the transition should be, due to Planck's law (see equ. 4.2), monochromatic. This infinitely narrow frequency response of the emitting or absorbing oscillator does however not exist. Every peak in a spectrum possesses a certain line width $\delta\nu$, which is here defined as Full Width Half Maximum (FWHM). Spectral lines, defined as transitions between quantified energy levels, may have values for $\nu/\Delta\nu$ which vary from 10^2 to at least 10^{12}. The fact that such a great scale of line widths exist at all, must be attributed to a corresponding variety of physical causes. The two most important ones are *Doppler broadening* and *pressure broadening*.
The frequency shift in radiation received from a moving source is called Doppler effect. The fractional change in frequency is:

$$\frac{\nu - \nu_0}{\nu_0} = \frac{v_x}{c} \ , \tag{4.4}$$

where ν_0 is the frequency sent out, ν is the frequency received, v_x is the velocity of the source (molecule) and c is the speed of light. Depending on the direction of v_x a red-shift or blue-shift can occur. This fact can be used for flow speed measurements, known as Laser Doppler Anemometry [MF01], [DMW87]. The process of line broadening results from the statistical velocity distribution of the radiating atoms. The continuous range of velocity distribution is given for gases by the Maxwell-Boltzmann relation. Only the velocity component towards the receiver contributes to the Doppler effect. A certain frequency shift $\nu - \nu_0$ corresponds to each velocity. The Doppler profile of line intensity follows, therefore, a Gaussian distribution of frequencies of the form $exp[\alpha(\nu - \nu_0)^2]$ [Eck96]. The frequencies for which the intensity I is $I_0/2$ determine the Doppler width

$$\Delta\nu_D = 2\nu_0\sqrt{\frac{2\ ln2\ k\,T}{m\,c^2}}\ , \tag{4.5}$$

where k is the Boltzmann constant, m the molecular (or atomic) weight and T the temperature. Doppler broadening is dominant at lower pressures where the collisions between the molecules have a negligible effect on the line shape.

For higher pressures the influence of collision becomes more important. This leads to an interruption of the wave train sent out by the molecule. Considering the case in which the function $f(t)$, shown in fig 4.1 represents such a single wave train of finite duration τ_0. Taking the Fourier transform [Fow68], leads to:

$$g(\omega) = \frac{1}{\pi}\frac{\sin[\frac{1}{2}\tau_0(\omega - \omega_0)]}{\omega - \omega_0}\ . \tag{4.6}$$

Fig. **??** shows the power spectrum $G(\omega)$. It is defined as:

$$G(\omega) =\mid g(\omega) \mid^2 \tag{4.7}$$

The width of the frequency distributions is given by:

$$\Delta\nu = \frac{1}{\pi\tau}\,. \tag{4.8}$$

This effect is called collision or pressure broadening and increases with shorter wave train

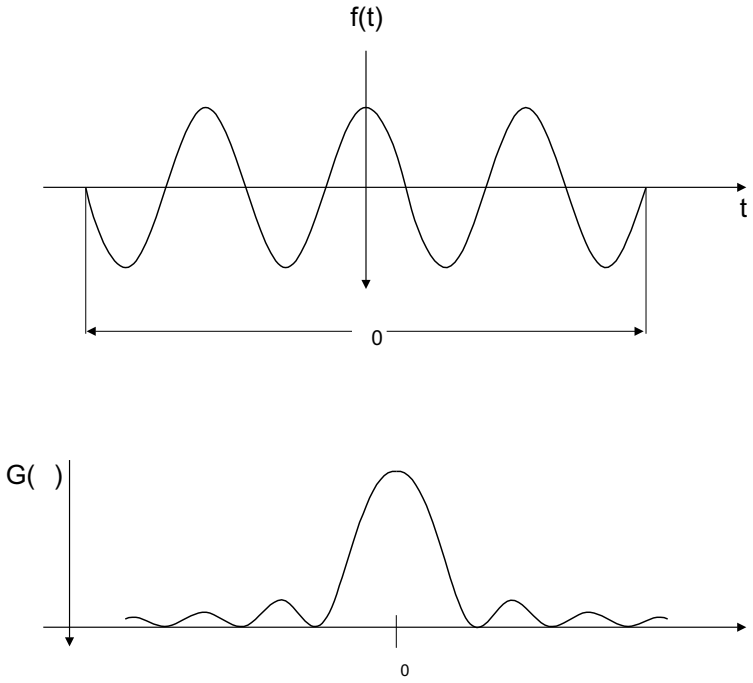

Figure 4.1: Finite wave train $f(t)$ and power spectrum $G(\omega)$.

duration τ. The line shape is determined by the statistically averaged effect of the distribution of collision times. The result is the Lorenzian line shape.
Depending on the strength of collision and distribution of collision times line shift can also occur [Bre61]. For the thermodynamic condition where neither the pressure nor the Doppler broadening is dominant, a mixture between both profiles, called Voigt profile, is used to describe the line shape.

4.3 Basic Principle

Laser induced fluorescence is a two-step process. In the first step the laser beam radiation is absorbed in the region where the beam passes through the gas. The second step is the spontaneous emission from the excited manifold. Since absorbtion and emission is involved, two spectra can be analyzed. To obtain an absorbtion or excitation spectrum, the wavelength of the absorbed source (laser) is varied and the emitted radiation intensity, which is integrated over a broad wavelength area, is detected. For the emission or fluorescence spectrum the wavelength of the laser light is kept constant and the spectrometer is scanned to record the

various emission transitions. If the fluorescence signal is detected at the same frequency as the excitation, it is called resonance fluorescence. For diagnostics this is normally not desirable because the fluorescence signal gets superposed by other scattering processes (e.g. Mie-scattering). Therefore in most LIF-applications the detected fluorescence is frequency shifted from the excitation frequency.

4.3.1 Energy Levels

The total energy of a molecule consists mainly of three parts: The energy in the electronic level, the vibrational level and the rotational level. The total energy E_{total} of the molecule is then approximately:

$$E_{total} \approx E_{el} + E_{vib} + E_{rot} \tag{4.9}$$

Fig. 4.2 shows the energy diagram of two electronic levels, their vibrational and some rotational levels. Each potential curve has a minimum, which indicates the stability of that configuration. Some configurations have no minimum and are for that reason not stable. These electronic states dissociate very fast and are used for Laser Induced Predissociation Fluorescence (LIPF) [Eck96], see sec. 4.3.4.

4.3.2 Nomenclature of Transitions

Each energy level can be characterized by certain quantum numbers. In order to describe a transition between any two energy levels a set of coded abbreviations is used. An electronic energy level with $\Lambda = (0, 1, 2, ...)$ is called a $(\Sigma, \Pi, \Delta, ...)$ state. Additionally a superscript (2S+1) is added on the left side, where S is the total spin number. The spin S determines the multiplicity (2S+1), which gives the number of sub-levels for a given value of J. The symbol "+" as superscript on the right identifies a molecule-function which is symmetrical to the line connecting the nuclei. The vibrational energy level, V, and the rotational energy level, K, can have values beginning with zero. One transition can be described for example as:

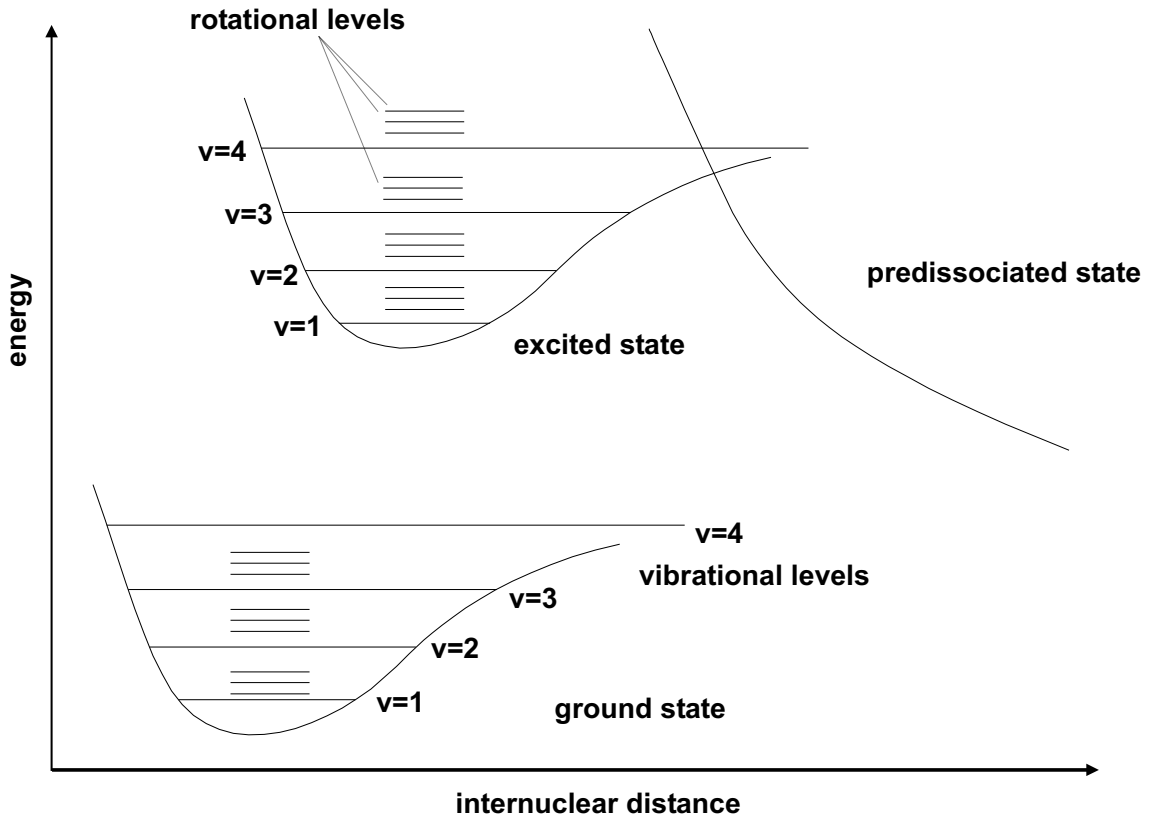

Figure 4.2: Energy diagram of electronic levels.

$$^2\Sigma^+, V = 3, K = 7 \quad \longleftarrow \quad ^2\Pi, V = 0, K = 8$$

The higher energy level is written here on the left and the direction of the arrow indicates absorbtion ($\longleftarrow$) or emission ($\longrightarrow$) . For every transition an abbreviation can be used. The information about the direction of the transition (absorbtion or emission) is thereby lost. The electronic energy levels are not included. The transition mentioned before is written as:

$$(3, 0)\ P_1\,(8)$$

The vibrational levels are written in brackets - the exited state is first. This expression is also called band. The following letter stands for the difference between the rotational levels: For $\Delta K = K_{excited} - K_{initial}$ (= ... -2, -1, 0, 1, 2, ...) the corresponding letters are (... M, N, O, P, Q, ...) and so on. The index at the letter gives the spin of the molecule before and after the transition. The following number in brackets is the rotational level of the ground state.

4.3.3 Two Level Model

Considering a simple two level model the possible optical and collisional processes connecting the two levels are shown in Fig. 4.3:

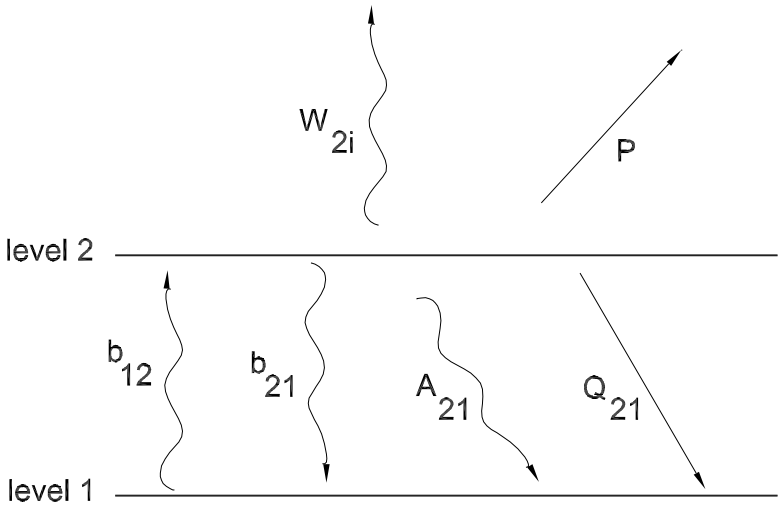

Figure 4.3: Simple two level model with rate constants.

Basically six different physical processes can occur: *absorption* (b_{12}), *stimulated emission* (b_{21}), *spontaneous emission* (A_{21}), *collision quenching* (Q_{21}), *predissociation* (P) and *photoionisation* (W_{2i}). The corresponding rate constants are written in brackets. For stimulated emission a photon with the same frequency as the laser frequency is emitted. The rate constants b are related to the Einstein coefficient B for stimulated emission or absorption:

$$b_{mn} = \frac{B_{mn}\, I_\nu}{c} \ , \tag{4.10}$$

where I_ν is the incident laser irradiance, c the speed of light and n and m are either 1 or 2. The Einstein coefficients are connected by the following equation, where g_i is the degeneracy of state i.

$$g_m \cdot B_{mn} = g_n \cdot B_{nm} \tag{4.11}$$

The rate constant for the spontaneous emission A_{21} is also known as Einstein transition probability for spontaneous emission or for short Einstein A, the transition probability for absorption

and stimulated emission is known as Einstein B. They are linked by:

$$\frac{A_{nm}}{B_{mn}} = \frac{8\pi h\nu^3}{c^3} = \frac{h\omega^3}{\pi^2 c^3} \tag{4.12}$$

In contrast to stimulated emission, the transitions for spontaneous emission can occur to different energy levels than the initial level. The fluorescence subsequently occurs until the original configuration is reached again. The energy of the emitted photons is equal to the difference in energy of the involved levels (Planck's law). A smaller difference in energy results in a longer wavelength of the emitted radiation. Transitions within an electronic level therefore emit radiation in the infra-red region. Transitions between electronic states involve bigger energy differences. The emitted light then occurs e.g. for the OH-radical in the UV region.
If other molecules are present, the excited state loss rate may increase considerably due to collisions involving the excited state and the molecular bath. This increase is known as quenching. Certain excited states may dissociate prior to the emission of a photon, a process known as predissociation, or may become ionized, called photoionisation.
The population density N_i of an energy level can be written as:

$$\frac{d\,N_i(t)}{d\,t} = \sum_{i \neq j} N_j(t) R_{ji} - N_i(t) \sum_{i \neq j} R_{ij} \tag{4.13}$$

R_{ij} are the integral rate coefficients for all the processes involved. Writing the state population densities for the simple two level model leads to:

$$\frac{d\,N_1}{d\,t} = -N_1\, b_{12} \;+\; N_2\,(b_{21} + A_{21} + Q_{21}) \tag{4.14}$$

$$\frac{d\,N_2}{d\,t} = N_1\, b_{12} \;-\; N_2\,(b_{21} + A_{21} + Q_{21} + P + W_{2i}) \tag{4.15}$$

Normally only specifically chosen excited states are predissociative. Also the photoionisation can be ignored in most cases. To simplify matters, the predissociation and photoionisation is neglected for now. In this case the system is a closed system:

$$\frac{d\,N_1}{d\,t} + \frac{d\,N_2}{d\,t} \approx 0\,. \tag{4.16}$$

hence the sum of N_1andN_2 is approximately constant.

$$N_1 + N_2 \approx N_1^0 \tag{4.17}$$

N_1^0 is the population of the lower level prior to the laser excitation. The excited state population can normally be neglected in the initial stage. Another simplification is that the imperfect overlap of the laser line shape and the absorption line shapes are neglected. The rate constant is written precisely as:

$$b = \frac{B}{c} I_\nu^0 \int_\nu L(\nu) g(\nu) d\nu \tag{4.18}$$

I_ν^0 is termed the normalized spectrum irradiance. The integral is termed the line overlap factor ($\leq$ 1). $L(\nu)$ is the laser spectral distribution function and $g(\nu)$ the laser line shape ($\int_{-\infty}^{\infty} g(\nu) = 1$). If the absorbtion line is centered to the laser line shape and the laser irradiance variation is negligible over the absorption line shape, Equ. 4.10 can be written as:

$$b_{nm} = \frac{B_{nm}}{c} I_\nu(\nu_0) \tag{4.19}$$

$I_\nu(\nu_0)$ is the laser spectral irradiance in the line center.
The fluorescence signal is proportional to $N_2 A_{21}$. In order to get qualitative results, N_1^0 is from interest and a relation between N_2 and N_1^0 is required. For the simple system assumed here equ. 4.15 can be solved algebraically for the state population density N_2:

$$N_2(t) = \frac{b_{12} N_1^0}{b_{12} + b_{21} + A_{21} + Q_{21}} (1 - e^{-(b_{12}+b_{21}+A_{21}+Q_{21})\cdot t}) \tag{4.20}$$

For this solution the initial population contribution $N_2(t = 0) = 0$ was used. It is useful to define a time constant τ:

$$\tau = \frac{1}{b_{12} + b_{21} + A_{21} + Q_{21}} \tag{4.21}$$

For $t \ll \tau$ the upper level population builds up linearly with time:

$$N_2(t) = b_{12} N_1^0 t \tag{4.22}$$

If the duration of the laser pulse is longer than τ the system reaches a steady state ($t \gg \tau$):

$$N_2 = b_{12} N_1^0 \tau \tag{4.23}$$

Since in most cases the rate constant for spontaneous emission A is much smaller than the one for quenching, Q, the steady state is mostly influenced by the collisional quenching or stimulated emission/absorption rate constant. For laser pulse lengths between 10^{-8} and 10^{-6} the steady state is a good assumption. N_2 can be so written as:

$$N_2 = N_1^0 \frac{B_{12}}{B_{12} + B_{21}} \frac{1}{1 + \frac{I_{sat}^{\nu}}{I_{\nu}}} \tag{4.24}$$

I_{sat}^{ν} is called the saturation spectral irradiance [1] and is defined as:

$$I_{sat}^{\nu} \equiv \frac{(A_{21} + Q_{21})\, c}{B_{12} + B_{21}} \tag{4.25}$$

For the steady state assumption, the fluorescence signal power F is written as:

$$F = h\nu N_2 A_{21} \frac{\Omega}{4\pi} l A \ , \tag{4.26}$$

where $h\nu$ is the photon energy and Ω the collection solid angle (steradian). Thereby A is the focal area of the laser beam (area of the beam cross section), and l is the axial extent along

[1] If the laser excitation irradiance I_{ν} is higher than the saturation spectral irradiance I_{sat}^{ν} the lower level gets depopulated. This is called laser induced saturated fluorescence (LISF), see sec. 4.3.5.

the beam from which the fluorescence is observed. The product $A \times l$ describes the light sheet volume in the field of view. Substituting for N_2 leads to:

$$F = h\nu \frac{\Omega}{4\pi} l A N_0^1 \frac{B_{12}}{B_{12} + B_{21}} \frac{A_{21}}{1 + \frac{I_{sat}^{\nu}}{I_{\nu}}} \tag{4.27}$$

At low laser excitation irradiance ($I_{sat}^{\nu} \gg I_{\nu}$) this equation can be simplified. The fluorescence power F is then given by:

$$F = h\nu \frac{\Omega}{4\pi} l A N_0^1 B_{12} I_{\nu} \frac{A_{21}}{A_{21} + Q_{21}} \tag{4.28}$$

Since the fluorescence power is linear proportional to the input laser irradiance, it is called the linear regime. The term $\frac{A_{21}}{A_{21}+Q_{21}}$ is termed the fluorescence efficiency. The overall fluorescence is not dependent on the laser intensity but on the laser power. The laser irradiance multiplied by the focal area yields the spectrum beam power.

For qualitative measurements the fluorescence efficiency has to be known. It is difficult to evaluate, since the quenching rate constant Q_{21} is a function of the specific molecular collision partners and their energy. Furthermore the quenching rate depends on the local thermodynamic conditions, especially the temperature. Since the thermodynamic conditions in combustion processes have significant local variations, it is difficult to calculate quenching corrections if the local thermodynamic conditions are unknown. There are two possibilities to avoid the effects of quenching on the fluorescence intensity: laser induced predissociation fluorescence (LIPF) and laser induced saturated fluorescence (LISF)

4.3.4 Laser Induced Predissociation Fluorescence (LIPF)

Certain energy levels have a high predissociation rate constant P. The rate constant P is independent of the background gas composition. The probability of transition to the unstable state is high if the excited energy level is chosen close to the point of intersection of the two potential curves (excited state and unstable state), Fig 4.2. This is known as Frank-Cordon principle. The depopulation of the excited level is then dominated by the predissociation rate constant P_2.

$$P_2 \gg Q_{21} > A_{21} \tag{4.29}$$

The transition to the dissociated state happens typically in 10^{-13} to 10^{-10} s. The lifetime of

the excited state is significantly shortened since the typical times for collisional quenching and fluorescence are 10^{-8} to 10^{-7}s. Assuming predissociation, the two level model is not a closed system anymore.

$$\frac{d\,N_1}{d\,t} + \frac{d\,N_2}{d\,t} = -N_2 P_2 \tag{4.30}$$

The population loss is negligible for smaller pumping rates, because the population of the excited state is then relatively small. To calculate the fluorescence power F the predissociation has to be considered. The fluorescence efficiency (see equ. 4.28) is in that case written as $\frac{A_{21}}{A_{21}+Q_{21}+P_2}$ and termed the Stern-Volmer-factor. Due to the dominance of the predissociation this leads to a fluorescence power F, which is independent of Q_{21}.

$$F = \frac{h\nu}{c}\frac{\Omega}{4\pi} l A N_0^1 B_{12} I_\nu \frac{A_{21}}{P_2} \tag{4.31}$$

The fluorescence power is directly proportional to the species density, which allows qualitative measurement without the knowledge of Q_{21} [AWW+92]. For the OH-radical LIPF can be applied for the (3, 0) band. The excitation wavelength for that transition is near 248 nm. The main problem with dissociative strategies is the very low fluorescence efficiency, which is a result of the shorter lifetime of the excited state.

4.3.5 Laser Induced Saturated Fluorescence (LISF)

The principle of LISF is based on sufficiently fast redistribution. The quenching process itself is not avoided. For high laser irradiance with $I_\nu \gg I_{sat}^\nu$ the fluorescence power (equ. 4.28) becomes

$$F = h\nu \frac{\Omega}{4\pi} l A N_0^1 \frac{B_{12}}{B_{12}+B_{21}} A_{21} \tag{4.32}$$

The fluorescence power is thus independent of both the rate constant for quenching and the laser irradiance. The absorbtion and stimulated emission are dominant in this case. LISF leads to the maximum fluorescence power and therefore to the maximum species detectivety. Problematic is the radiation from other scattering processes, which increase mostly linearly with the rising laser irradiance and occur as noise in the background.

Another problem is the high laser intensity required. Since the laser beam normally has a Gaussian intensity profile, the outer regions called wings, have a lower intensity. Due to lack

of saturation in the wings, the signal therefore may exhibit a dependence on the quenching rate.

4.4 Experimental Considerations

The experimental setup for LIF-measurements consists normally of three main parts: the laser, the light sheet optics and the detection-system. The laser beam is formed by the light sheet optics into a thin light sheet. The emitted fluorescence is captured by collection optics and imaged on to the CCD-chip of a camera. The timing of the laser and the camera-shutter is carried out by a delay-generator. Depending on the internal delays of the laser and the camera the delay of the trigger-pulses have to be adjusted for each system individually.

4.4.1 Laser

The laser has to be tunable to different wavelengths and have a small spectral line width in order to excite a single transition efficiently. The required line width is dependent on the beam intensity and the sensitivity of the camera system. If the profile of the laser is too broad, the line overlap factor may be insufficient. The intensity of the laser in the regions beside the overlap of absorption-line and laser profile contributes to all other scattering processes and leads to a worse signal to noise ratio (SNR). For OH-fluorescence the laser has to be able to operate in the UV region. The transitions used for LIF diagnostics involving the OH-radical for example are in the region of around 250 - 310 nm wavelength. Another criteria for the laser is the intensity, which is required for a high excitation efficiency.
Tuneable dye lasers or tuneable excimer lasers are often used. The strongest lines for excimer lasers are at 248 nm (KrF) and 308 nm (XeCl). Dyes, either as solutions or vapors, are the active medium in pulsed dye lasers. They are tuneable in a spectral region of around 60 nm. Thus a variety of dyes is necessary in order to cover the entire spectral range. Dye solutions for excimer lasers are available for wavelength down to 320 nm. To reach the deep UV-regions the dye output has to be frequency doubled. This leads to an energy loss in the order of 75%.

4.4.2 Light Sheet

The output profile of dye-lasers is normally circular. The aim is to get a thin light sheet in the order of 10^{-1} mm. Therefore two lenses have to be used. Due to losses by reflection and absorbtion by the lenses, no more lenses than necessary should be used. First the beam-profile has to be stretched in one direction and then collimated in the perpendicular direction. Fig. 4.4

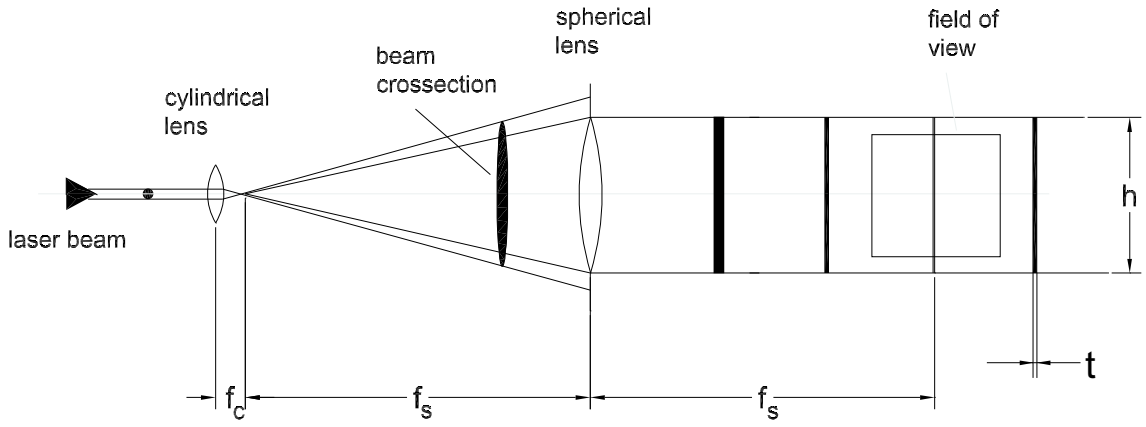

Figure 4.4: Typical setup of lenses for forming a light sheet. Light sheet cross section t × h.

shows a possible setups where one cylindrical lens and one spherical lens are used. In order to get a constant irradiance, the ideal light sheet is a parallel light beam. The limiting factor for the extension of the light sheet height, h, is then the lens diameter of the cylindrical lens. If h varies along the field of view the detected fluorescence power will decrease reciprocal with h. This has to be considered for quantitative measurements, as well as the Gaussian divergence of the laser beam. A diverging light sheet is (depending on the field of view dimensions) sometimes unavoidable in order to cover the whole field of view. Due to the Gaussian profile of the laser the intensity will vary along h. Only the center part of the profile can be used for the light sheet and the laser "wings" should not be visible in the field of view. If the light sheet thickness t varies along the field of view the fluorescence power stays the same, but the picture will become increasingly blurred because a bigger volume is excited by a smaller energy density. To avoid large distances between the lenses the cylindrical lens can be chosen with a negative focal length. For tuneable excimer lasers, the light output profile is often rectangular, such that the use of one cylindrical lens might be sufficient, depending on the light sheet height desired.

4.4.3 Detection System

Due to the extremely short process to be detected the camera should be a short-gateable ICCD camera system with a high quantum efficiency photocathode. The gate-width should be in the order of 100 ns. A further point to consider for the photocathode is the spectral response range. For single shot applications, the phosphor screen should have a slow decay time and be fiber coupled to the CCD to get maximum gain. For quantitative measurements the functional dependence of the intensity on the input illumination has to be known. For certain wavelengths and especially for higher fluorescence intensities a linear dependency is not always given. The lens-system for the camera has to be UV-transmissive (e.g. UV-Nikor from Nikon). Due to the high temperatures the combustion process sends out radiation. To minimize the background noise due to the natural fluorescence, the temporal gate for the LIF-detection should be as short as possible and overlap at the same time completely with the fluorescence signal.
In order to detect the radiation of the fluorescence wavelength a filter has to be used which limits the wavelength interval to be detected. Sets of color-filters are an insufficient solution. Interference filters offer a good selection of different wavelength gates. Also reflection filters can be used. These kind of filters are coated and the transition maxima are given by the thickness of these coatings. By turning the filter the effective length of the light through that coating-layer is varied. Ideally the angle between the incoming and outgoing beam is 90°. By slightly varying this angles the transmission wavelengths interval can be shifted and therefor the SNR optimized. The wavelength shift can be e.g. up to 20 nm for a filter interval centered at 300 nm with a FWHM of 20 nm.

4.5 Alignment of PLIF Setup

Besides the internal alignment of the laser, which will not be discussed here, the alignment of the lenses, which are forming the light sheet, is important for the quality of the results. Here the alignment of the system shown in Fig. 4.4 consisting of one cylindrical and one spherical lens is described.
To achieve a thin intensive light sheet the beam has to pass through the lenses perpendicularly and through its center. This minimizes losses and prevents aberrations. A small fraction of the light beam passing through lenses normally get reflected on the front and rear surfaces, unless the lens is specially coated. This reflection effect is used to get the lens in the right position.

First both lenses are removed and the laser beam adjusted in such a way that it passes through the center of the field of view. The the cylindrical lens is placed first on the optical bench, which is aligned with the laser beam. The light sheet height in the field of view can be adjusted easily, if the alignment of optical bench and laser beam is exact. If the beam passes the lens perpendicularly in the center, both reflections coincide with the laser beam. A good way to see the reflections is to position a business card with a small hole in front of the lens. The laser beam has to pass the hole and the reflections should coincide exactly with the hole.

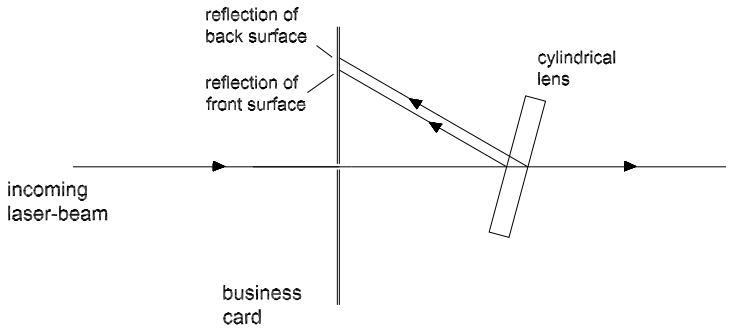

Figure 4.5: Tilting the cylindrical length in order to identify the reflections on front and back surface; top view.

The lens should be in a lens holder which is tiltable and adjustable in height. To aid in the identification of the front- and back reflected beam, the lens can be tilted a little bit around the vertical axis (Fig. 4.5). By changing the height of the lens the front reflection should be the same height as the hole. Doing so ensures that the front surface is perpendicular to the incoming beam. If the back reflection is not the same height the lens has to be tilted around the horizontal axis perpendicular to the beam. If the reflected beam occurs lower than the hole, the lower part of the lens has to be tilted towards the incoming beam, Fig. 4.6. Then the height has to be newly adjusted and the procedure started again.

The cylindrical lens is placed at a distance equal to its focal-length from the center of the field of view. This ensures that the light sheet thickness t is at its minimum in the middle of the field of view. The spherical lens is adjusted in the same way as the cylindrical one by placing the business card between these two lenses. The reflected beam of the front surface will appear broader, because the convex front surface has a diverging effect on the beam. For

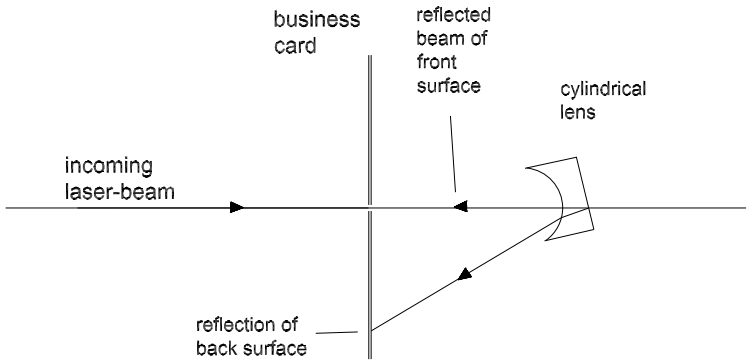

Figure 4.6: Position of the cylindrical lens after first step of adjustment; front surface reflection coinciding with incoming beam; side view.

the spherical lens the procedure described above has to be carried out in the vertical and horizontal directions, since the lens is curved in both dimensions.
Moving the cylindrical lens along the optical axis changes the intensity distribution along the light sheet height h. The bigger the distance between the two lenses the lower the total energy of the light sheet but the smaller the intensity variation over the light sheet height.

Chapter 5

Experimental Setup

5.1 Detonation Tube

The test facility consists of three tube sections and a test section and is 8 m in length overall. The inner diameter is 279 mm. The sections are connected by flanges and sealed with O-rings, Fig. 5.1. The test section has a square 150 × 150 mm cross-section. In order to minimize the influence of this cross sectional area change a "cookie-cutter" is used to effectively cut out a wave of square cross-section from the incident detonation wave.

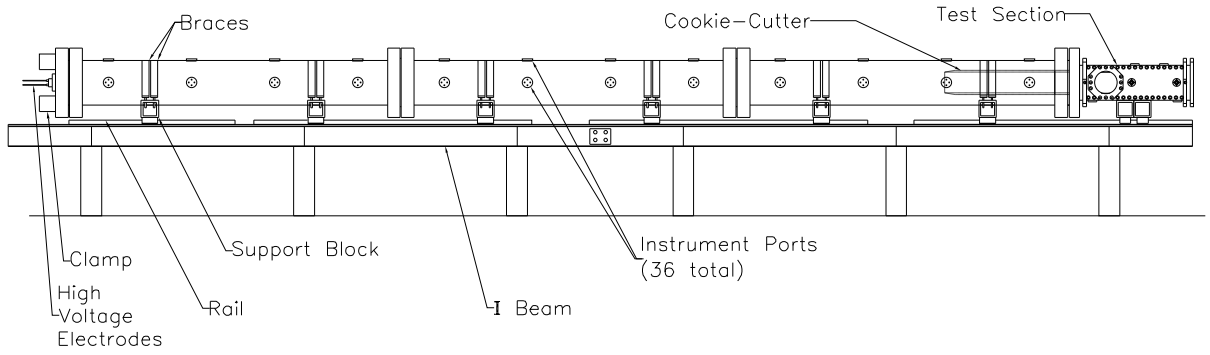

Figure 5.1: Side view of the Gas Dynamics Tube (GDT). Courtesy of Tong Wa Chao.

The tube is initially evacuated to approx. 0.04 mbar prior to each filling procedure. The filling procedure is based on the partial pressure of each gas species the mixture contains. The gauge accuracy is 0.13 mbar. In order to get a homogeneous mixture the whole volume is circulated with a bellows pump through an circulation line, not shown in the image, for five minutes. The

ignition mechanism consists of an exploding copper wire at the fire-plug. The fire plug is removable and has to be "loaded" with a thin copper wire before each shot. The wire is connected to the high voltage circuitry. High voltage capacitors (2 μF) are charged to 9000 V. The discharge across the copper wire is triggered by a high-voltage pulse from a trigger module. To promote the initiation of a detonation a "driver" is used. Directly before the ignition by the exploding wire a slug of acetylene-oxygen mixture is injected in the vicinity of the firing-plug. The filling pressure prior to the injection is equal to the final target initial pressure, less the partial pressure of the driver gas injected. This ignition system enables a direct initiation of the detonation.

5.2 Schlieren Set up

The light source for the schlieren setup is a Q-switched ruby laser [Akb00]. The laser components (rear cavity mirror, polarizing beam splitter, pockels cell, ruby rod with flash lamp, output coupler) have to be aligned with a autocollimator in order to get sufficient illumination of the schlieren image. The pulse width of the laser is approx. 50 ns. The laser beam is directed by a plane beam steering mirrors onto the beam expansion lens, Fig. 5.2. The previously diverging beam leaves the first concave mirror of the schlieren head (f_{M1} = 1000 mm) as a parallel light beam and is directed perpendicularly through the test section. The parallel light beam with a diameter of 150 mm is collimated by the second concave mirror (f_{M2} = 1000 mm) and focused onto a 83×108 mm black and white Polaroid 667 (3000 ISO). An electronic capping shutter and a laser band filter avoid fogging of the film by light in the room and light emissions from the reacting flow.

The trigger scheme for the ruby laser is shown in Fig. 5.3. The flash lamp of the ruby laser has to be charged first and then fired around 1 ms before the Q-switch is switched. When switching the Q-switch the actual laser-light-pulse occurs. The flash-lamp has to be fired around 1 ms prior the Q-switch in order to reach the population inversion in the laser medium.

The positions and number of schlieren edges was varied. When only a vertical edge was used, the details behind the leading shock were not visible (shot 1365, p.115). A horizontal edge resolved more details behind the leading shock, but the leading shock was not imaged sharply. A vertical edge with increased distance to the focus together with a horizontal edge, which was placed very closely to the focal-point, led to acceptable results: a crisp edge from the leading

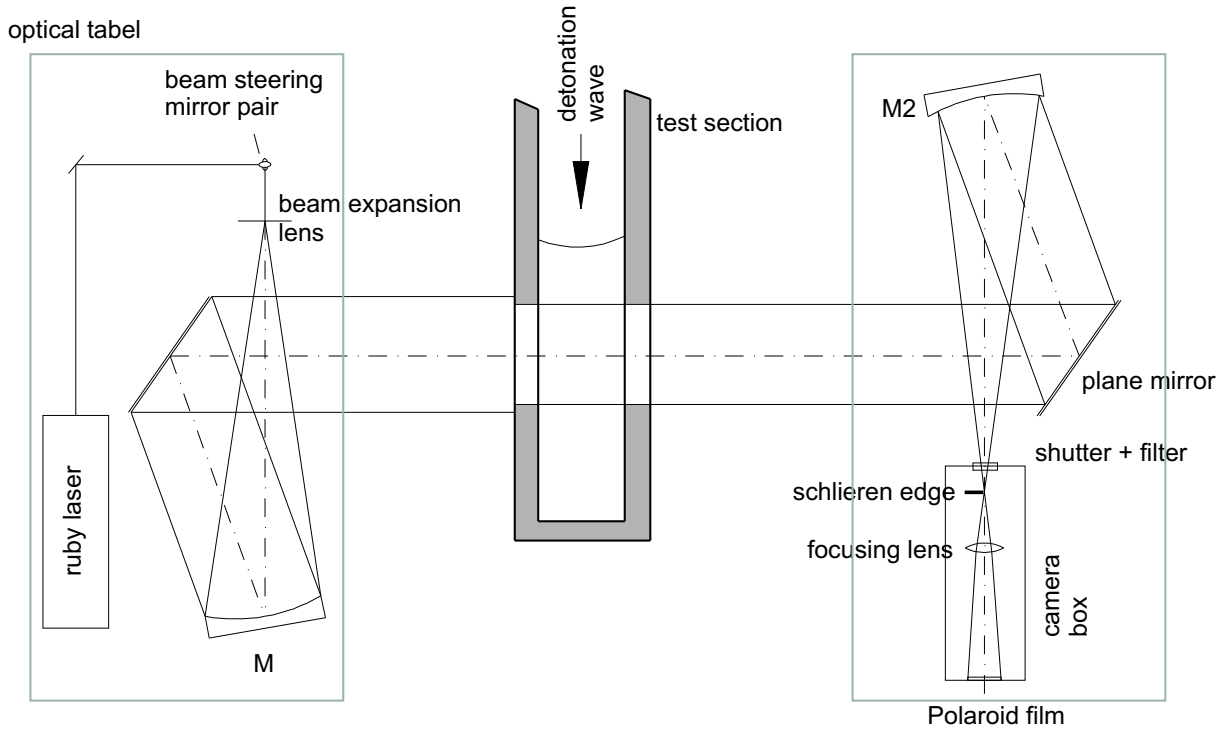

Figure 5.2: Z-setup of the schlieren imaging system.

shock and details in the region behind the shock. If the vertical edge was placed too close to the focal point, the leading shock appeared too strong on the image, covering details directly behind the shock front. The sensitive position of the horizontal schlieren edge led to problems: The flash lamp of the ruby laser moves the ruby rod slightly when fired. So the focus-point at the schlieren edge moves slightly from shot to shot, which can result in unwanted dark-field schlieren technique (see shot 1367, p.115).

For the simultaneous PLIF-Schlieren images the setup was modified. Two schlieren edges were used, both placed approximately 5 mm away from the foci. In order to get a larger field of view, a different lens was used, and the distances slightly adjusted as a shadowgraph setup. By doing so, the leading shock was still visible as a clear edge and more details were shown behind. Without the schlieren edges the leading shock appeared blurred, which is disturbing when superposing with the PLIF-image, where the distance between shock and reaction zone is of interest.

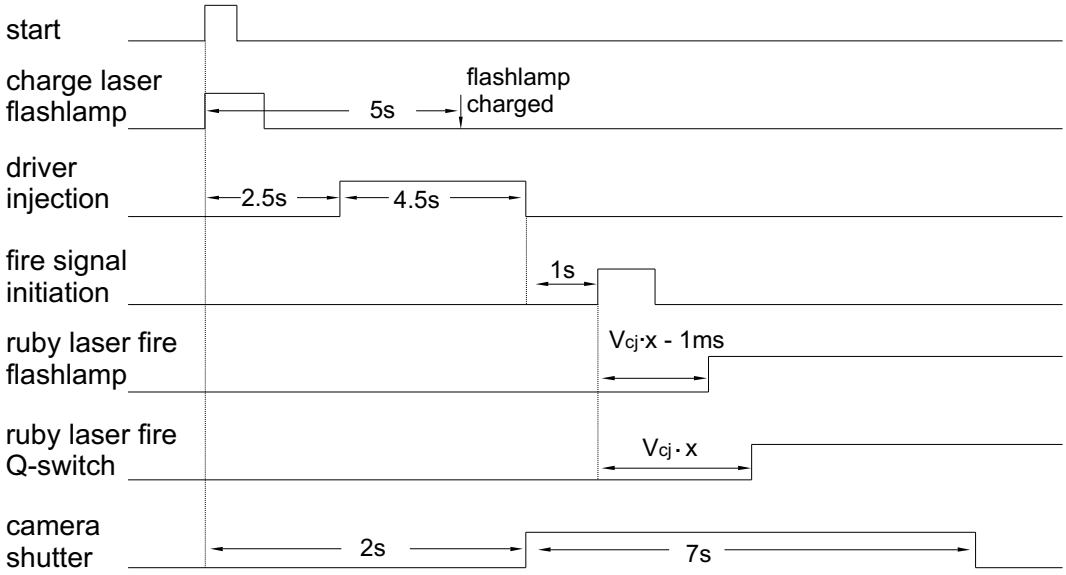

Figure 5.3: Timing scheme for ruby-laser-schlieren-setup, where x is the distance from the initiation point to the canter of the observation window.

5.3 PLIF Setup

For the PLIF setup optical access to the combustion process from two directions, perpendicular to each other, is necessary. For the fluorescence detections, the same window as for the schlieren setup is used. Special UV-transmitting windows of either quartz-glass or UV-grade fused silica (63 mm thickness, 155 mm in diameter) have to be used. The optical access for the light sheet is a 3 mm broad and 125 mm long slit at the end plate of the tube, Fig. 5.4. The glass window mounted over that slit is 50×180 mm and 25 mm thick. The detectable intensity of the fluorescence is therefore lowered by the absorbtion of excitation energy by the laser inlet window and the absorbtion of the emitted fluorescence radiation by the observation window.

5.3.1 Laser

The laser system consists of an excimer laser (COMPex102, Lambda Physik) and a dye laser (Scanmate2E, Lambda Physik) with a frequency doubling unit. The excimer laser filling gas

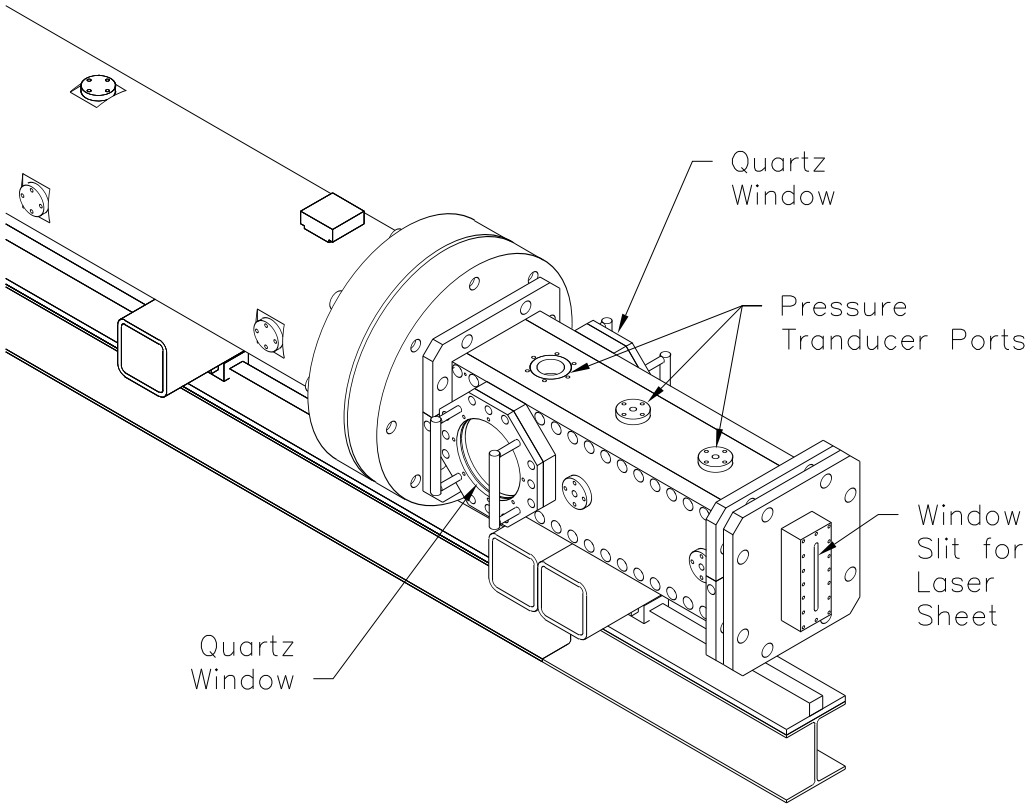

Figure 5.4: Test section with its optical access for schlieren and PLIF technique. Courtesy of Tong Wa Chao.

is XeCl and so the output-wavelength is 308 nm [1]. The pulse energy is approximately 250 mJ. The exit beam is 24×7 mm and the pulse duration is approx. 20 ns. Since the maximum repetition rate is 20 Hz, only the single shot mode will be applied in the experiment. The dye laser is pumped by the excimer laser. In the current system LambdaChrome Coumarin153 ($C_{16}H_{14}NO_2F_3$) is used as a dye. The dye has to be dissolved in a dye solution, which in this case is ethanol. The dye laser consists of four main components: oscillator, grating, pre-amplifier and amplifier. By turning the grating, the output wavelength in the particular range of the dye can be selected.

The tuning range reaches for the dye used from 522 nm to 600 nm. The peak output is found at 540 nm. The bandwidth is in the order of 0.15 cm^{-1}. When tuning the wavelength

[1]The COMPex102 is a multi-gas laser and therefore other filling gases, like ArF (193 nm), KrF (248 nm) and XeF (351 nm), can be used alternatively.

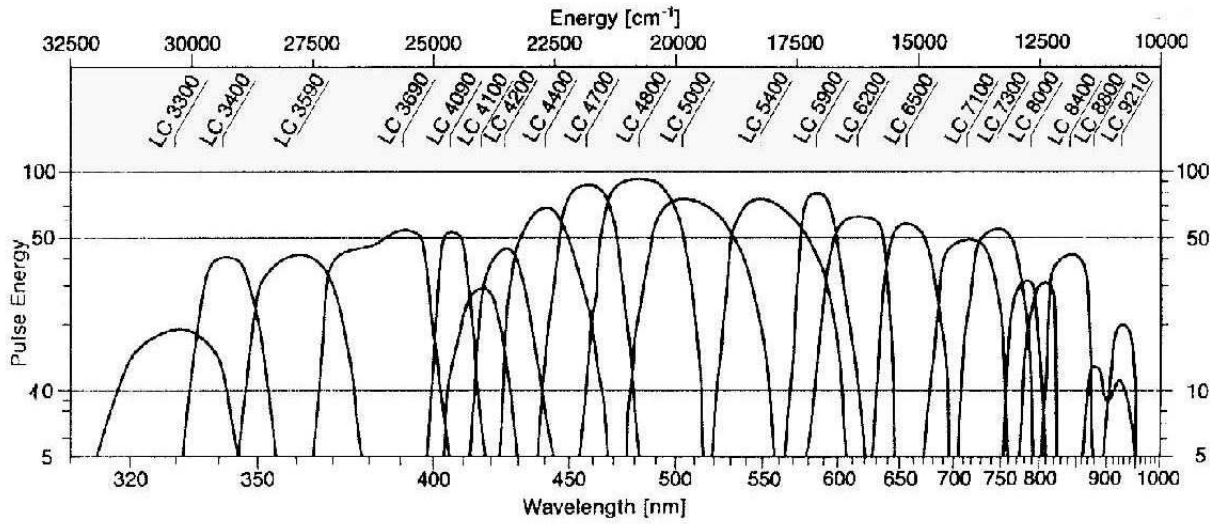

Figure 5.5: Dyes for Excimer Laser pumped dye lasers ([Bra97]); The LambdaChrome product number shown on top for Coumarin153 is LC5400; The pulse energy scale has only relative units, because it depends on the pump laser energy.

the minimum step width is 10^{-3} nm. The oscillator, pre-amplifier and amplifier curvet are pumped transversely. With the frequency doubling unit, wavelength can be set in the range of 261 nm to 300 nm. The bi-refringent crystal is responsible for the output of the second harmonic wavelength and is turned when tuning the wavelength to keep the optimum angle to the incoming beam. The compensator keeps the axis of the outgoing beam at the same place during the tuning process. The pulse energy before the frequency doubling is around 35 mJ, after the frequency doubling around 7 mJ.

The laser-beam is then directed by three coated 45°-mirrors in such a way that it coincides with the axis of the tube, Fig. 5.6. At the end of the tube is an optical bench for the light-sheet forming components. A plano-concave cylindrical lens with a focal-length of -25.4 mm and a spherical lens ($f_s = 1000$ mm) is used to form a light sheet of approximately 80 mm in height h. The light sheet does not cover the whole field of view (150 mm) possible. The intensity of detectable fluorescence intensity increases for decreasing light sheet height for two reasons: the light sheet has a higher intensity ($\sim h^{-1}$), and the camera is placed closer to the light sheet, which results in a bigger steradian of detection (h^{-2}) but a smaller field of view. The

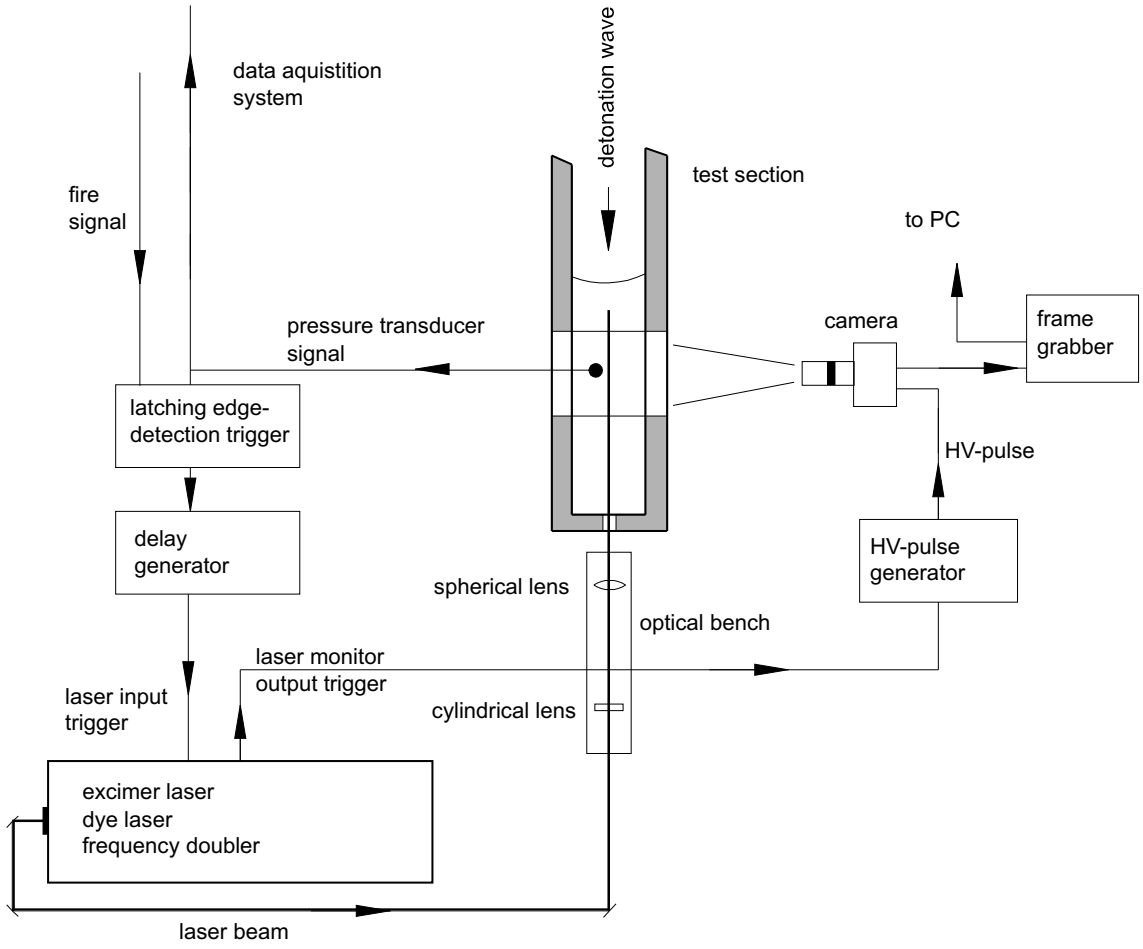

Figure 5.6: Experimental setup and triggering of the PLIF system.

detectable fluorescence intensity increases therefore ideally cubically with decreasing light sheet height, h, as long one is not operating in the saturated fluorescence regime.

For the simultaneous schlieren and PLIF setup the camera was moved out of the parallel light beam of the Schlieren-setup and focused in an 12° angle to the optical Schlieren axis on the light sheet plane. The field of view of the camera was thus horizontally distorted by around 2%. This was corrected with digital image postprocessing. A schematic of the simultaneous setup is shown in Fig. 5.7.

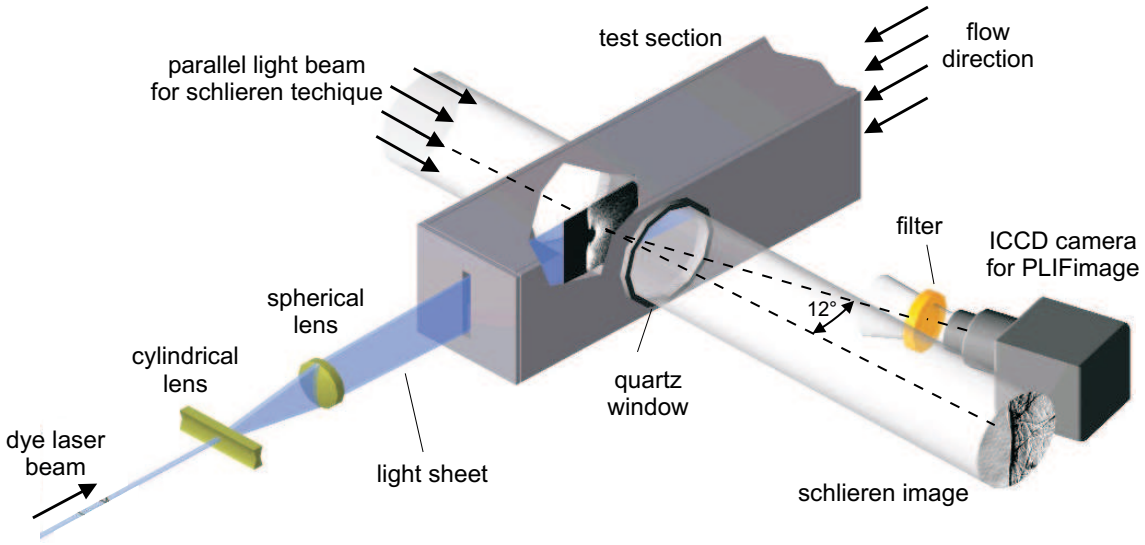

Figure 5.7: Simultaneous schlieren and PLIF setup.

5.3.2 Laser Calibration

The laser calibration is performed by measuring the fluorescence signal intensity of a test flame while scanning in laser wavelength. A hydrogen-air diffusion flame is placed in the test section. The delay time from the laser-input trigger signal gating-pulse signal to the camera has to be adjusted, so that the fluorescence occurs in the gate-width of the camera system. The time where the main fluorescence occurs is in the order of 20 ns and only slightly later than the laser pulse. Theoretically the gate width could be set that short. The delay from the laser input trigger signal to the actual laser light pulse is not constant and varies from pulse to pulse, known as time base error or jitter. To reduce the jitter a so called monitor output for the excimer laser exists, which can be used as a time base for the laser light pulse. However, the time base error of the light pulse in the system used has a random shot to shot variation (≈50 ns) and an average drift component (≈200 ns), which might be caused by small temperature changes. A qualitative function of the jitter is shown in Fig. 5.8.

Since for a scan in wavelength for calibration up to 250 images in a row are obtained the gate-width has to be set to 200 ns to ensure that the laser pulse occurs during the time the gate is open, and the entire fluorescence is detected. For the experiment with a detonation the gate-width is set as short as possible in order to minimize the influence of chemiluminescence

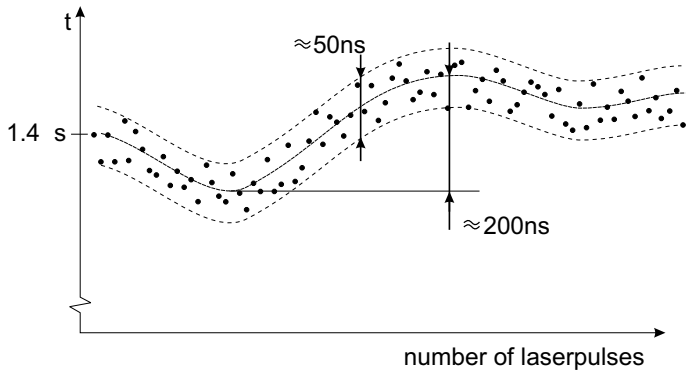

Figure 5.8: Qualitative function of time base error of laser light pulse for a 1 Hz pulse frequency. Δt is the time between the laser trigger input and the actual light pulse.

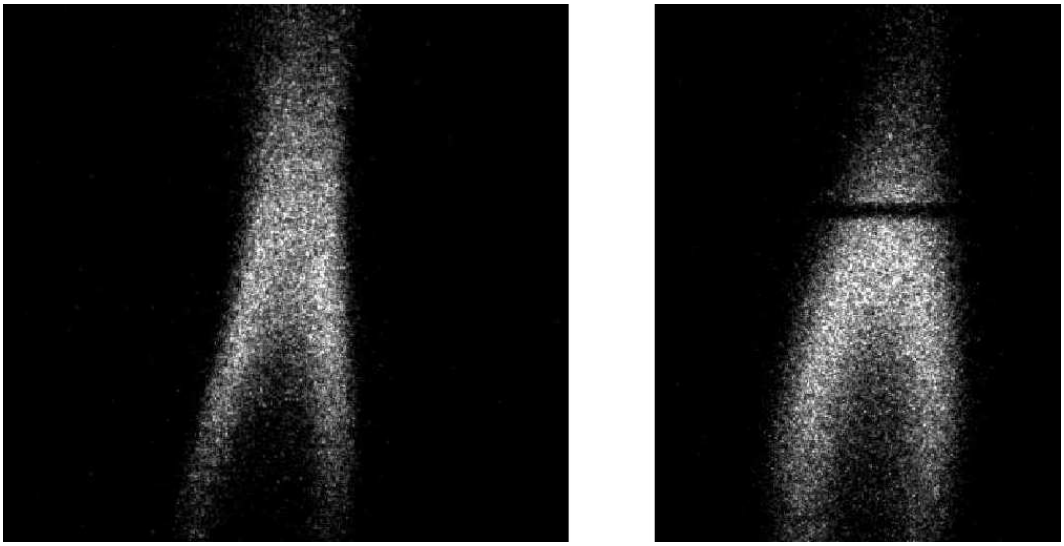

Figure 5.9: PLIF image of test flame in test section. The right image shows the light sheet partially blocked out by a dirt particle on the inlet window.

on the obtained image (sec. 5.3.3). Since the chemiluminescence increases linearly with the gate-width, the signal to noise ratio is inversely proportional to the gate-width as long the entire fluorescence occurs within the gate-width. The step width for the scanning is $5 \cdot 10^{-4}$ nm and the step frequency is 1 Hz. The chemiluminescence of the test flame is relatively small so that a small signal to noise ratio is given.

A image of the diffusion test-flame is shown in Fig. 5.9 on the left. The reduced energy density

in the wings of the light-sheet lead to the reduced fluorescence intensity on the top and bottom of the image. The light sheet enters from the left. If the light-sheet is blocked out by dirt-particles on the light-sheet inlet window a black stripe occurs on the image, Fig. 5.9 right. This shows that the detected luminosity is not chemiluminescence but PLIF. For detonation experiments, PLIF experiments with a partially blocked light sheet were conducted to compare the PLIF- with the chemiluminescence-intensities, sec. 6.5. The theoretical absorbtion lines can be calculated with the "LIF-base" - program [LC99], a simulation tool for spectral analysis. This simulated spectrum was then compared with the experimental one to evaluate the offset of the real wavelength output to the one shown on the laser control unit, which the laser seems to be set to, Fig. 5.10. The offset is in this case around 87^{-3} nm. Once that offset is known it enables relatively precisely changing to different absorption lines, since the wavelength of the absorbtion lines can be calculated. The obtained offset is not exact, due to several reasons:

- The energy output of the laser changes from shot to shot by up to 15 %.
- The flame moves slightly and the area hit by the light sheet changes for that reason.
- The exact spectral profile of the dye output beam is unknown.
- The FWHM of the absorption lines are due to pressure broadening under 1 atm relatively large.

Therefore it is still necessary to fine tune the laser to the center of a certain absorbtion line. This is done by scanning over a small wavelength interval in the order of 10^{-2} nm and setting the wavelength so that maximum fluorescence yield is achieved. In order to increase the SNR for the experimental scan the average fluorescence signal intensity of a manually set region, which covers around the section of the flame, was calculated.

With the simulation-tool LIF-base several excitation lines with higher fluorescence yields were preselected and then studied in detail experimentally with the test flame. Even though the thermodynamic conditions and mixtures of the test flame differ from the ones occurring in the detonations the results were sufficient. Two transitions were found to be adequate for OH-PLIF: a) $Q_1(6)$ (283.011 nm), b) $Q_1(9)$ (284.007 nm). Close to both are further strong lines: a) $Q_{12}(3)$ (283.012 nm), b) $Q_2(8)$ (284.009 nm). Due to the earlier mentioned broadening effects these line will overlap for the thermodynamic conditions behind

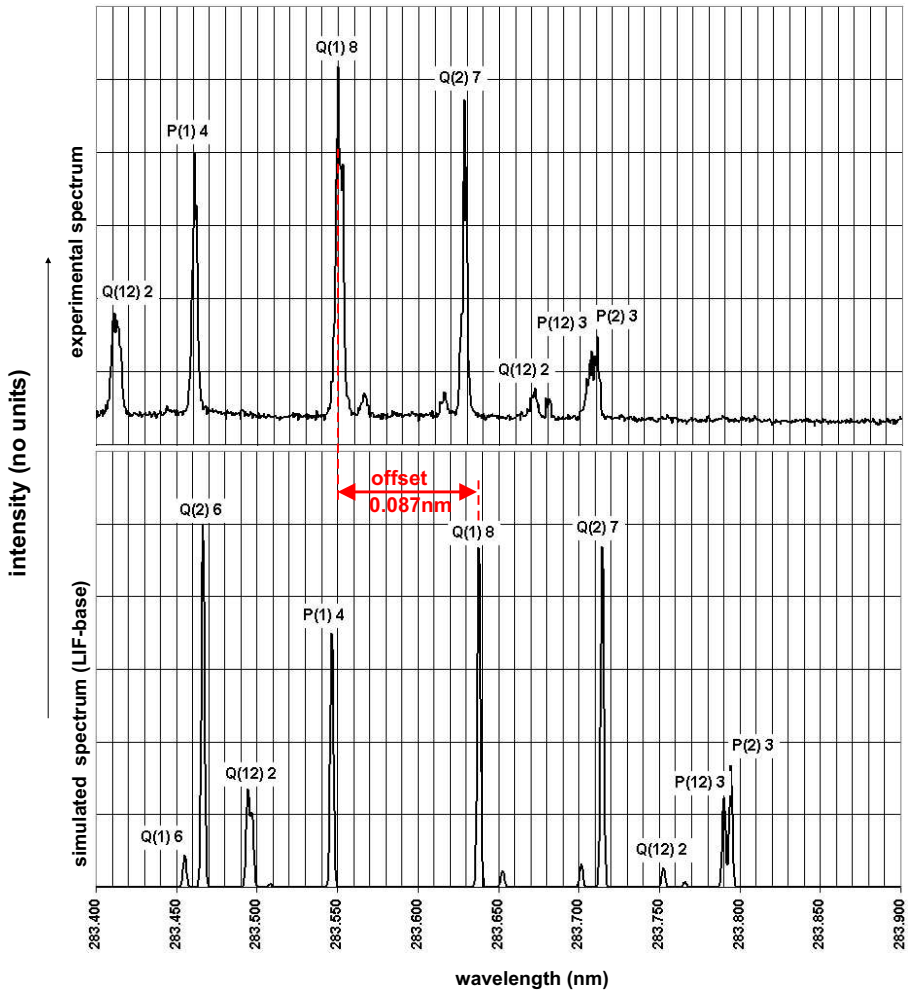

Figure 5.10: With hydrogen-air flame experimentally obtained spectrum and with LIF-base simulated spectrum. Step width: 5^{-4} nm, one image per wavelength.

detonation waves. The calculated CJ-conditions were around 300 kPa in pressure and 2500 K in temperature for the mixtures used. In the simulations the $Q_{12}(3)$ had a much smaller fluorescence intensity than the $Q_2(8)$ line. The expected overlap of $Q_1(9)$ and $Q_2(8)$ occurring at higher temperature and pressure is therefore more efficient. For the detonation experiments the wavelength was therefore tuned to 284.008 nm. The idea was that the laser line is centered in between $Q_1(9)$ and $Q_2(8)$. The spectral width of the laser is sufficient to overlap with the existing peaks on both sides. Since the obtained offset of the wavelength for the laser calibration is not precise, it is difficult to determine the exact wavelength of the output-beam and the actual excitation wavelength might differ slightly from 284.008 nm.

5.3.3 Triggering and Timing of the Imaging System

Since the conditions during the detonation are different from the diffusion test-flame, only a guess for the gain setting of the camera could be made from the test flame experiments. To avoid damage of the CCD-chip the gain should be set lower than this, because the intensity of the detonation image can be much higher. The optimum gain, set by the MCP voltage, for the camera is set if the maximum fluorescence yield is slightly below the overexposure limit of the camera. By doing so the full intensity resolution of the camera is used.

The camera is an intensified 12 bit CCD detector (Princeton Instruments ITE/ICCD-576). The CCD has a resolution of 576×384 pixels. Imaging optics include a Nikon UV-Nikkor 105 mm f/4.5 camera lens which transmits in the UV-region. The camera contains a high-voltage pulse generator (PG-200), providing the gate pulse, which enables shutter times down to 3 ns. In most of the experiments the gate width was set to 100 ns. The previously described jitter required that the delay between the laser monitor output and nominal light output had to be set individually prior to each experiment. By doing so one eliminates the "average" jitter component and is only left with the "shot to shot" jitter component. The pulse generator for the camera includes a delay generator, which allows the direct triggering of the camera system by the laser monitor output. The entire PLIF system is thus triggered by the laser-input trigger.

The laser input trigger signal is provided by the pressure transducer, which is located at the window-center in the top plate of the test-section. Since the noise of the capacitor for the exploding wire used for initiation would trigger the laser too early, the laser input signal has to be processed. This is done by a gate, which sets the output to "no signal" (TTL-low) until 2 ms after the firing signal regardless of the input. After this period a comparator provides a rising edge (TTL-high) if the pressure transducer output signal rises over the trigger level. The pressure transducer signal may oscillate around the trigger-level and cause the comparator to trigger several times. To avoid this, a single-shot device is included, which resets itself 10 ms after the first trigger-pulse. The processed pressure transducer signal functions as the laser input trigger signal. After around 300 ns the laser monitor signal is provided, which is used to trigger the delay generator of the camera system, Fig.5.11. After the delay time (≈1.2μs), which is set directly before the experiment, the pulse for gating the camera is provided. While the camera gate is open the laser light pulse

is sent and within approximately 30 ns the fluorescence is occurring and detected by the camera.

A paper target positioned exactly at the light sheet location is used to focus the camera. Since a low f-number of 4.5 is used, the adjustment has to be done very carefully. The filter in use is an interference filter with a transmission in the region between 303 nm and 323 nm (FWHM). That is the wavelength region where the transitions (0,0) and (1,1) occur. These transitions have a high transition probability.

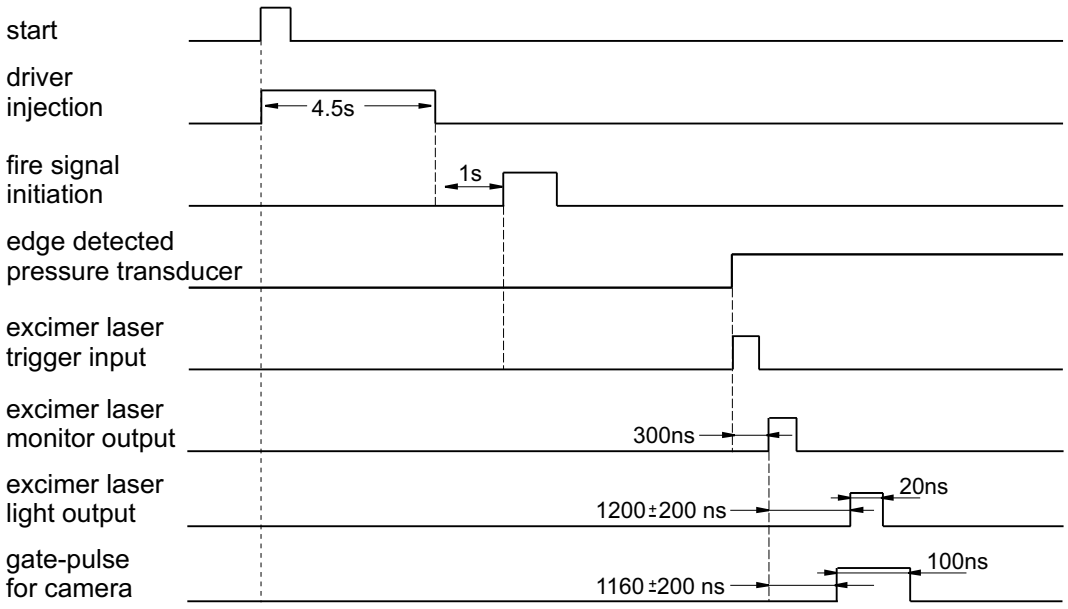

Figure 5.11: Timing diagram of the PLIF-system.

5.4 Soot foils

Square 150×150 mm soot foils were mounted on the end walls of the test section. Soot foils were also mounted on the sidewalls of the test section replacing the glass windows. To soot the surface the foils are placed into a sheet metal cylinder with a lid on top. Strips of cloth, dipped in jet-fuel, are lit at the bottom of the cylinder and ensure a homogeneous thin soot layer on the aluminum sheet. The soot foils are sprayed with "Krylon Crystal Clear Acrylic Coating", which prevents any smearing of the recorded traces. Then a digital image is taken and processed. With a 2-dimensional Fourier analysis of the image the average cell size can be evaluated [SMMT86]. These soot tracks were not of a high quality, so the cell size had to be

determined manually.

5.5 Mixtures

All experiments were conducted at a initial temperature of 21° C and an initial pressure of 20 kPa. All mixtures were stoichiometric hydrogen-oxygen-diluent systems. Argon and nitrogen were used as the diluent gas. The argon dilution was varied from 80 to 90 % and nitrogen dilution varied between 45 and 75 %. Velocity-measurement exist for all mixtures. Soot foils, schlieren-technique and PLIF were used parallel to the velocity measurements.

Chapter 6

Experimental Results and Discussion

Each shot is identified by its shot number. Around 80 shots have been performed. A complete shot list is shown in appendix F. Simultaneous schlieren-images where performed in some experiment to verify the origin of the features seen in the PLIF images.

6.1 Velocities

Five pressure transducers, mounted along the tube record the detonation pressure and time-of-arrival which is used to calculate the wave-speed. Pressure transducers P_1 to P_3 are placed at a distance of 2.75 m, 4.58 m and 6.43 m measured downstream of the fireplug. Pressure transducer P_4 is located in the test section at the center of the window-line (7.49 m) and P_5 is 0.19 m downstream of P_4. The measured velocity U, shown in Fig. 6.1 and 6.2, is normalized with U_{CJ}, where U_{cj} is the calculated velocity for a CJ-detonation. The data points of the calculated detonation wave velocity are thereby centered between the two corresponding locations of the pressure transducers, since only the average between two pressure transducers could be measured. Since all mixtures studied were close to the initiation limit of the facility, an overdriven wave was observed between P_1 and P_2, followed by a decay to sub CJ velocities between P_2 and P_3.

The velocity deficit is in the cookie-cutter- and the test-section the highest. The detonation velocity was, except for the highly (75 %) nitrogen dilution mixture, within 94% of the CJ-value. The CJ-velocities were calculated with the STAN JAN thermodynamic equilibrium program ([Rey86]). The shot to shot differences in the velocity might arise from the tube filling

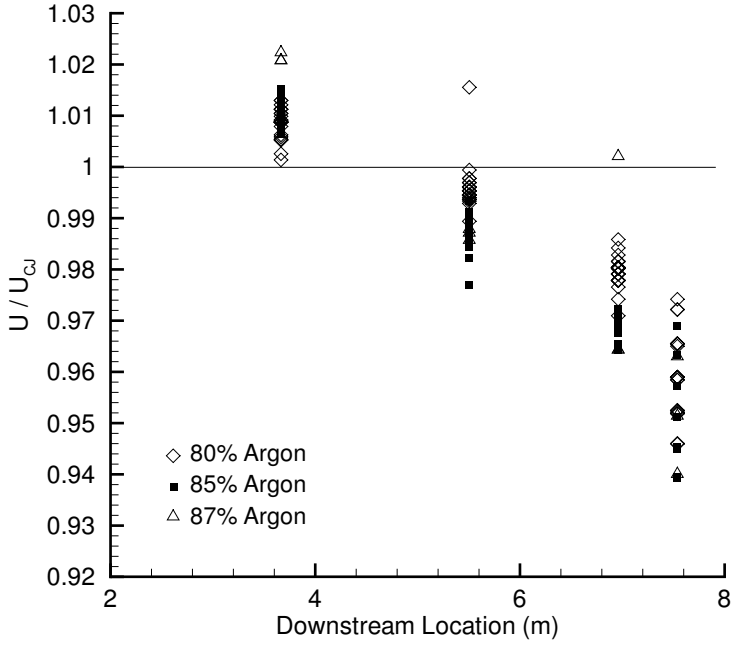

Figure 6.1: Averaged velocity deficit between the pressure transducers (P_{1-5}) of Argon-diluted mixtures.

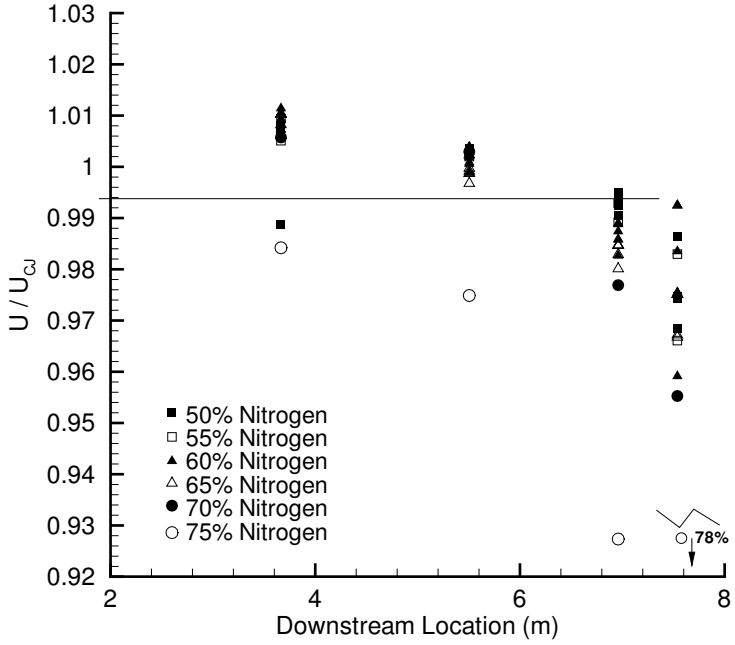

Figure 6.2: Averaged velocity deficit between the pressure transducers (P_{1-5}) of Nitrogen-diluted mixtures.

procedure uncertainties. The digital data acquisition system for the pressure transducers is sampling at 1 MHz, which matches the pressure transducer response time of 1 μs. The typical time of arrival measurement error is $\pm$ 1 μs. The measured transit time error is therefore $\pm 2\mu$s. The detonation waves studied were propagating with an velocity of approximately 1500 m/s, which leads for to a velocity uncertainty of 2% at the maximum. This maximum is calculated for the smallest distance between two pressure transducers (P_4 and P_5) in the setup. This might as well explain the bigger scatter of the velocity data points in the test section.

6.2 Soot foils

The soot foil at the test section endplate is a good indicator of whether the detonation transitioned to an orthogonal geometry in the test section. If a detonation is rectangular, the soot tracks on the endplate show a grid of slapping and principal waves which are perpendicular to each other and parallel to the side walls (Sec. 2.8). In equivalent mixtures the detonation front structure did not develop repeatable an orthogonal geometry. Figure 6.3a shows a good example for a rectangular detonation, whereas in Figure 6.3b the transverse wave are not aligned in an orthogonal grid.

It appears that the square cross section is not long enough to ensure the development of a rectangular detonation. The soot foil in Fig. 6.3b shows the presence of slapping and principal wave structures, which reach from wall to wall but they are not parallel to the walls or perpendicular to each other. Argon diluted mixtures showed, as expected, more regular cells and developed a rectangular detonation more often than nitrogen diluted mixtures. Mixtures with larger cell size did not develop a rectangular detonation as far as mixtures with smaller cell size until reaching the endplate. An example of a perfectly rectangular detonation (Shot 1385) together with all other obtained soot foils is shown in appendix. A, p. 110.
The strong transverse wave structure as described in Chapter 2.5 (p.14) with three triple point tracks was observed neither on endplate nor on side wall soot foils in any of the shots. It is possible that the quality of the soot foils at the side walls was not good enough to resolve such detail. The double lines observed on some endplate soot foils seem to be two slapping or principal waves moving in opposite directions. They are close to each other shortly before and

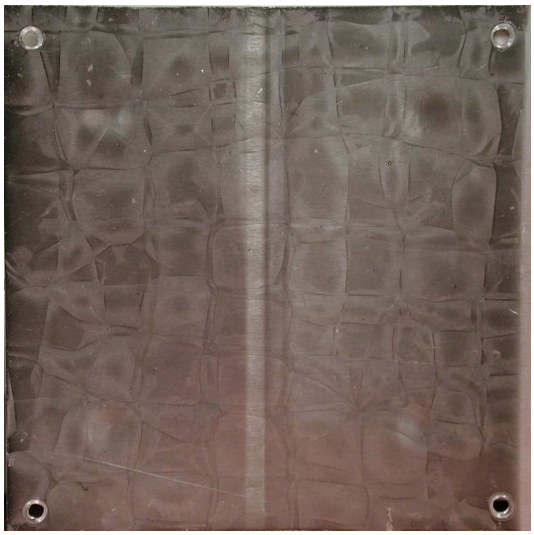

(a) Shot 1382, 80% Argon

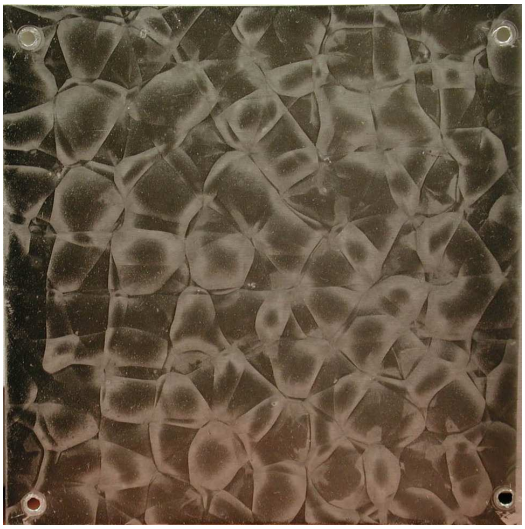

(b) Shot 1383, 80% Argon

Figure 6.3: Endplate soot foils of two experiments with identical mixtures. Different stages in the development of a rectangular detonation. a) Completely developed; b) First coherent transverse wave structures reaching over the whole soot foil.

after the triple line collision.

Generally, there are three different types of cells, which can be observed when looking at one time-instant at an oncoming detonation front, which are shown in Fig. 6.4: Cells expanding at all borders (type 1), cells closing at all borders (type 2) and cells expanding at some and closing at some borders (type 3). Here a perfectly rectangular detonation is discussed. Even though the transverse wave configurations in the experiments are distorted in comparison to this ideal perpendicular grid, they in principle exhibit the same characteristics. The endplate soot-foils also show different three types of cells: Cells with bright (soot free) borders, ones with dark (soot covered) borders and ones with bright and dark borders. The borders of the cells show a clear orientation (sooted↔soot free), which could be corresponding to the direction in which the transverse/slapping wave is propagating. Even though the principle of the soot foils is not completely understood one possibility is that the shear layers wipe off the soot at certain parts of the soot foil. According to this assumption, the shockwave is running in the direction of the darker region (Fig. 6.5). In Fig. 6.6 the three corresponding types of cells

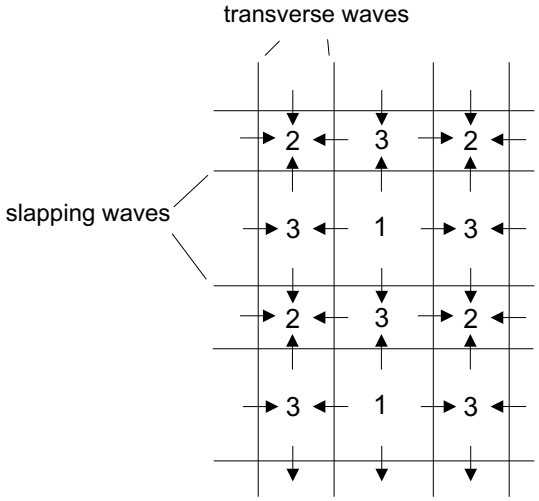

Figure 6.4: End view of a detonation with an orthogonal wave structure. The different types of cells are labeled by numbers 1 to 3.

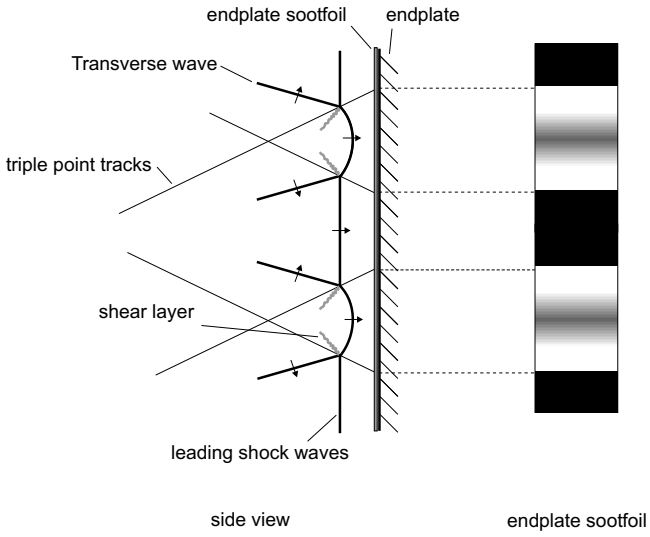

Figure 6.5: Side view of a detonation close to the endplate soot foil and the possible corresponding 1-dimensional soot foil pattern.

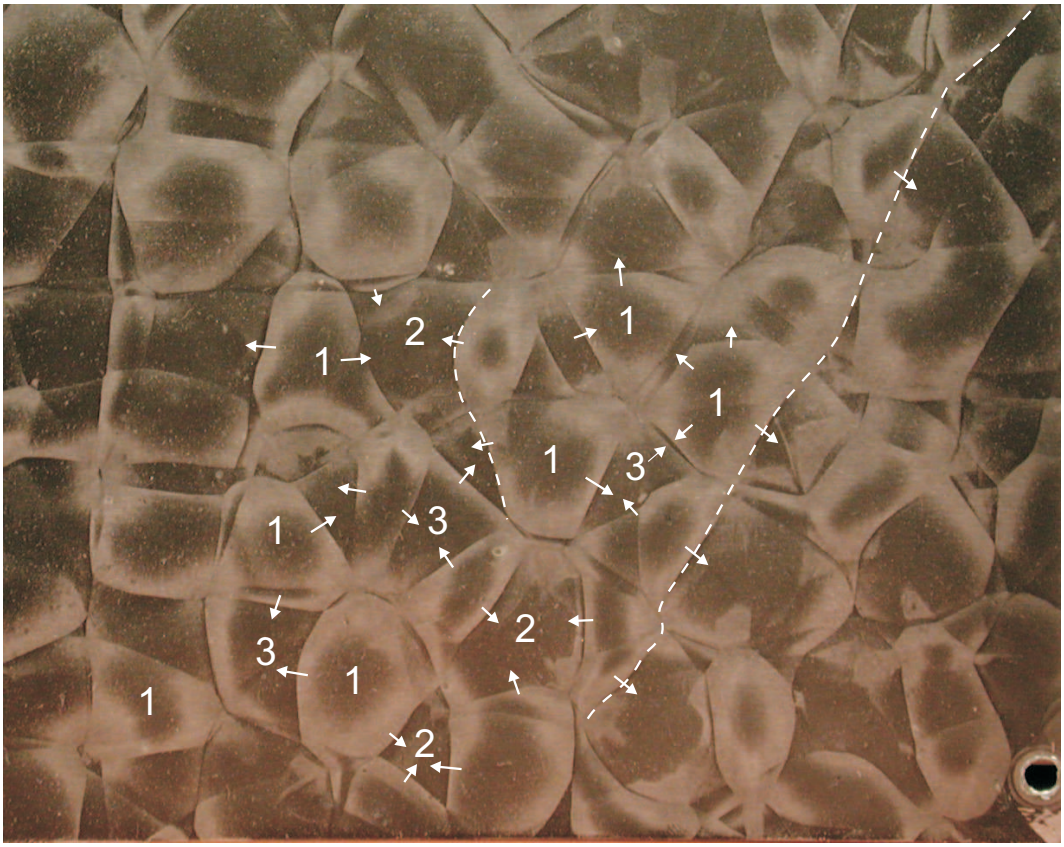

Figure 6.6: Different types of cells observed on endplate soot foil and the assumed direction of transverse wave structures.

observed experimentally and the direction the transverse waves are assumed to be running in are illustrated. To verify this theory a simultaneous side-soot-foil, which joins the endplate soot-foil is useful. Due to problems in mounting the side-soot-foils, this could not be realized in the current setup.

6.3 Cell Size Measurement with Soot foils

Soot foils were also mounted on the side walls of the test section. The foils were 150 mm in diameter so for some shots only 5 cells were visible on the soot foils. In these cases, several shots were done to obtain a sufficient number of cells in order to evaluate the cell size. By measuring the cell sizes manually from the soot foil, the measurements are always afflicted with an observer error. To minimize this influence the cell size was obtained by measuring 12 different cells for one mixture, canceling the biggest and smallest, and averaging. The error bars shown correspond to the largest and smallest cell size measured, Fig. 6.7. In case the detonation showed an orthogonal geometry, the endplate soot foil could also be used to determine the cell size, since the distance of the slapping waves, which is equal to the cell size, was recognizable. The error bars for the nitrogen diluted mixtures are bigger than for the argon diluted ones, a fact which indicates the higher regularity of the argon diluted mixtures.

6.4 Schlieren Images

On the schlieren images obtained one transverse wave family was significantly more visible - either the transverse waves moving upwards or the ones moving downwards. The propagation direction of the transverse wave can be inferred for the Ar-diluted mixtures from the inclination angle. Transverse waves inclined downwards in flow direction are moving upwards and vice versa. The whole schlieren setup, except the schlieren edge, is symmetric to the plane given by the optical axis. Changing the side (left, right, top, bottom) of the schlieren edge with respect to the focal point of the system had no reproducible influence on which wave family was visible. If the transverse wave as a three dimensional object is nearly planar in the direction perpendicular to the flow direction and is aligned with the optical axis of the schlieren set-up it is visible best on the schlieren image. This has the following reasons: The deflection of the light beam is then largest, since the optical density gradient is perpendicular to the incoming

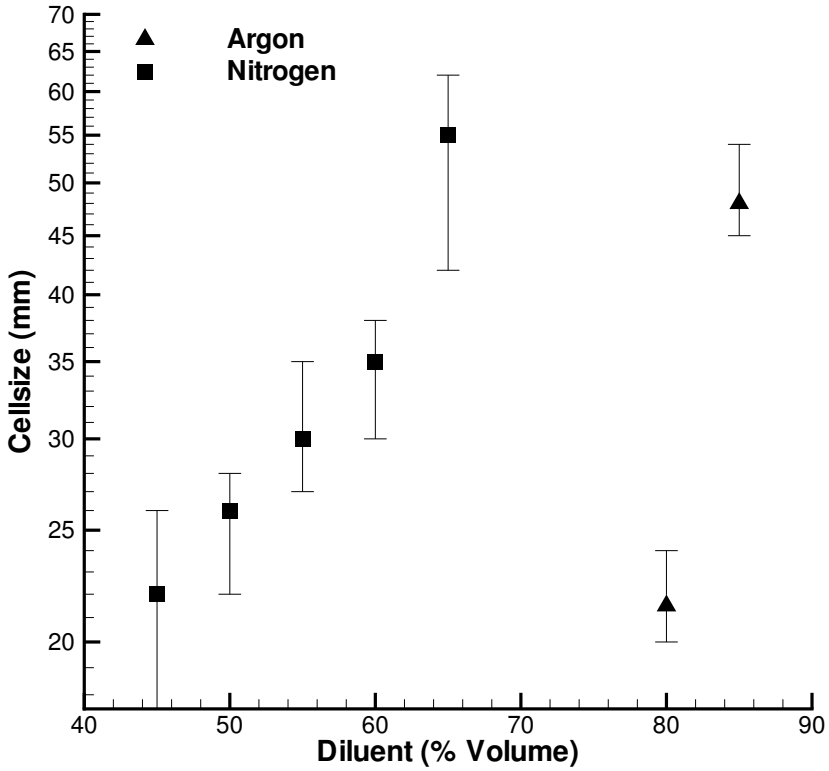

Figure 6.7: With soot foil obtained cell sizes for argon- and nitrogen-diluted mixtures in the 150×150 mm test section.

light beam and this large deflection gets integrated for the whole distance traveling in the measurement volume, see sec. 3.1.3, p. 20. It is unlikely that only the transverse waves of one family shows such an alignment. Further studies are required to understand the phenomenon observed on the schlieren images.

The periodic inflection points along the front and the visible transverse wave spacing allows the cell size to be determined from the schlieren image for some shots, Fig. 6.8, 6.9. These shots are mostly Argon diluted mixtures, which are characterized by having a higher cellular regularity and greater tendency to develop an orthogonal structure. The cell sizes determined from the schlieren images are smaller than those obtained from soot foils, because due to the integrating nature of the schlieren technique, the transverse waves seen are not necessarily in the same plane parallel to the paper plane of the schlieren images. Therefore an out-of-plane transverse wave can appear in between the two in-plane transverse waves, leading to a

reduced, incorrect transverse wave distance measured. Also the curvature of the transverse wave perpendicular to the flow direction has to be considered as a possible error source when measuring the transverse wave distance.

For the mixtures investigated here the cell sizes could only be determined for a few mixtures with the schlieren technique. In the current setup, where an orthogonal structure is not ensured, the schlieren technique is not an alternative for the soot foil method.

Nitrogen diluted mixtures showed the alternating curved parts at the shock front connected to the cellular structure not as clearly as the argon diluted mixtures. The leading shock seems to be much less smooth and planar for nitrogen diluted mixtures. In the ideal case the Mach stem appears as a stronger curved section whereas the incident shock corresponds to the straight section. Due to the more irregular structure of nitrogen diluted mixtures and the resulting missing alignment of the transverse waves, the schlieren technique masks the alternating curvature for these mixtures much more strongly. The transverse wave structures were observed more than around one cell size behind the front and occurred approximately as straight lines. In this region the transverse waves are for all nitrogen diluted mixtures nearly parallel to the flow direction, whereas for argon diluted ones they appear at an angle of around 12° to the flow direction (Shot 1396 p.117, Shot 1373 p.116). Also the curvature of the transverse waves observed for nitrogen diluted mixtures in a region of around one cell-size behind the shock appeared much stronger. In general the transverse waves in nitrogen diluted mixtures were not as striking on the schlieren images. This is probably due to the previously described missing alignment of the transverse wave.

6.5 Chemiluminescence

The chemiluminescence images of a detonation were taken to estimate the background signal present in the PLIF images. The experimental setup was exactly the same as for a PLIF-experiment, but the laser light sheet was completely blocked. For one shot the laser-light sheet was only partially blocked to see the different intensity levels in one image. Even though the difference between the intensity levels is not as significant as for the atmospheric test-flame

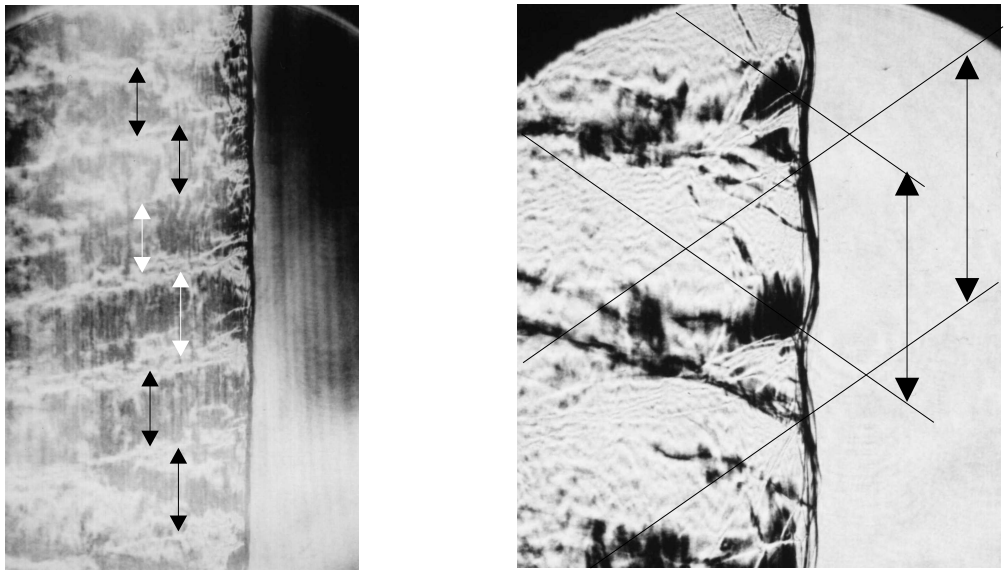

(a) Shot 1367; 80% Argon

(b) Shot 1373; 85% Argon

Figure 6.8: Cell size determination by analyzing schlieren images; a) Transverse wave spacing; b) Curvature of the front and assumed triple point trajectories.

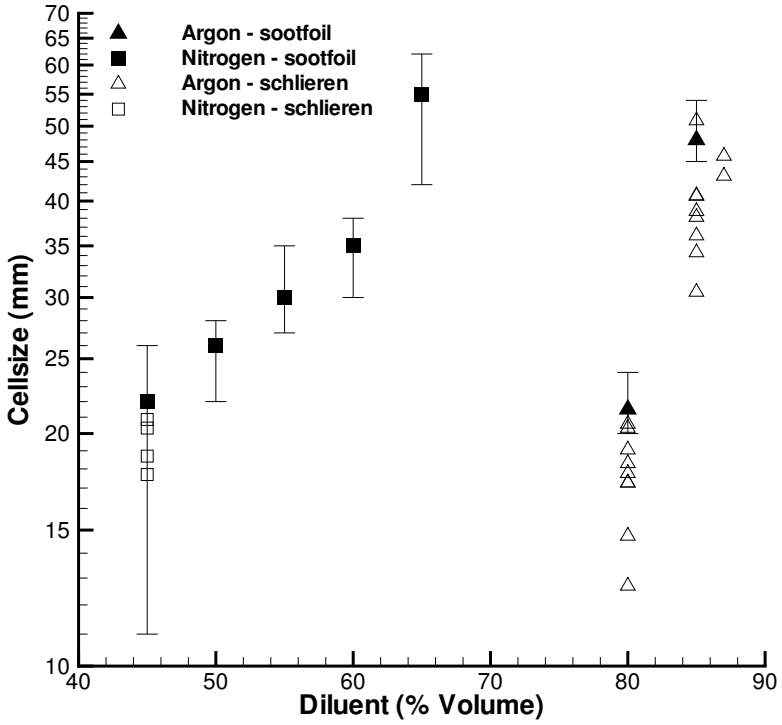

Figure 6.9: Comparison of cell sizes determined from schlieren images and soot foils.

(Fig. 5.9, p. 67), the PLIF intensities are clearly dominant. The background noise of the camera is around 450 ±10 counts. The maximum chemiluminescence intensities were measured for the 80% Ar-diluted mixture to be approximately 700 units, the PLIF intensities around 2500 units, depending on the mixture. Note that the images shown here are not intensity clipped but contrast adjusted. A linear function remains between the counts per pixel by the camera and the intensity of that pixel shown in the image here. The maximum and minimum counts per pixel within one image set thereby the endpoints on that gray scale. Therefore chemiluminescence signals seen in one image might occur with the same brightness as PLIF-signals in another image, even though the number of counts are significantly different.

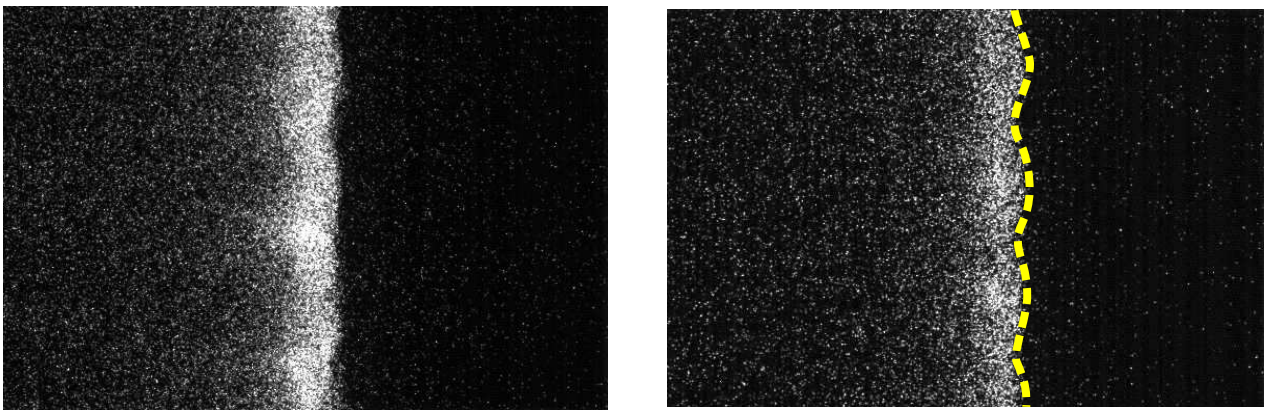

(a) Shot 1362; 80% Argon

(b) Shot 1363; 80% Argon

Figure 6.10: Chemiluminescence image of 80% diluted Argon mixture. Gate width 100 ns. Maximum intensity: 700 counts.

Fig. 6.11 shows a picture of a shot in which the light sheet of the laser was blocked out in the bottom half. This gives a good comparative estimate of the PLIF relative to the chemiluminescence intensity. The curved but unresolved fuzzy front with its cell structure is still visible in for chemiluminescence images, Fig. 6.10b. These periodic oscillations along the front indicate probably a nearly rectangular detonation since chemiluminescence is, such as the Schlieren-technique, an integrating visualization technique. In shot 1362, Fig. 6.10, the oscillations in intensity and curvature at the front do not seem to be periodic which could be due to a lack of alignment and orthogonal geometry of the transverse wave system.

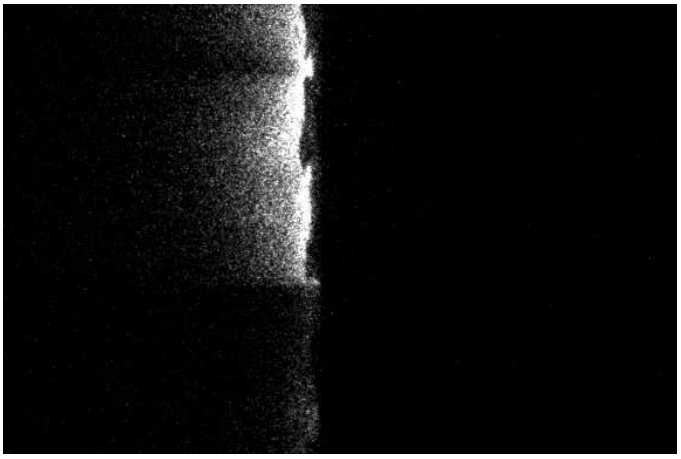

Figure 6.11: Blocked laser light sheet on the bottom half. Upper half PLIF, lower half chemiluminescence (Shot 1411). Maximum intensity: 2500 counts

6.6 Planar Laser Induced Fluorescence

All PLIF-pictures show a 75 × 112 mm field of view. One OH-fluorescence image is obtained for each experiment. In all images the detonation wave is traveling from left to right.

6.6.1 Qualitative considerations

For all experiments a distinct OH concentration front can be observed. The fluorescence intensity was higher for argon diluted mixtures than for nitrogen diluted mixtures. Since the chemiluminescence signal demonstrates a similar intensity for both diluents an improved signal to noise ratio for the Ar-diluted mixtures was seen. The signal intensity varies from shot to shot. This is due to two main reasons: The output energy of the pump laser varies from shot to shot influencing the fluorescence yield. Also timing uncertainties between laser and camera due to the laser jitter may lead to a non-complete temporal overlap of the camera-gate and the fluorescence signal.

A discontinuous keystone structure is revealed in the PLIF images. The reaction front is clearly lagging behind in these locations. These are the parts of the reaction front behind the incident wave , in the closing half of the cell (Sec. 2.5). Other sections of the reaction-front, which are ahead, represent a shorter induction length and therefore a stronger shock, which

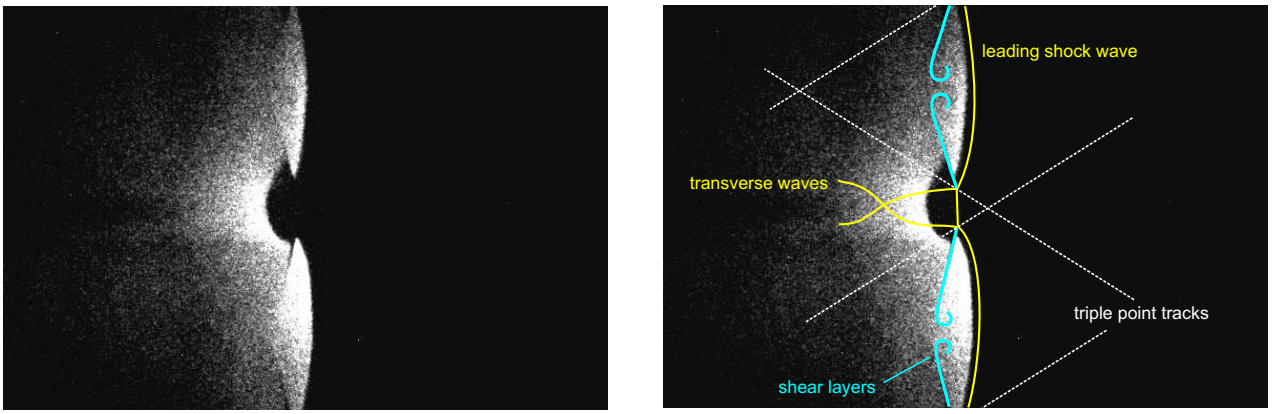

(a) (b)

Figure 6.12: Experimental observation of OH distribution. (a) Symmetrical keystone geometry (Shot 1419, 85% Argon). (b) Corresponding location of leading shock, transverse waves and shear layers.

exists in the first half of a cell oscillation cycle. Only one endplate-soot foil (Fig. 6.3, p.76) showed a completely rectangular detonations and therefore it is unlikely that the light sheet is always intersecting the transverse wave perpendicularly. For that reason the orientation of the light sheet regarding the wave structure is varying from shot to shot. This and the random variations of the transverse waves position and phase are the reason why the PLIF-image show non-identical reaction front structures, and no coherent time series can be constructed. Qualitatively the same features are observed on all the images.

The keystone geometry with low OH-fluorescence is present for all shots. One particularly pronounced feature can be seen in Fig. 6.12. One can also interpret the feature seen in that particular image as two keystones of higher fluorescence. One dimensional simulations of the reaction-zone behind the shock-front shown in sec. 6.6.2, indicate, that there is a sharp rise in the OH-concentration at the end of the reaction zone. The PLIF-signal obtained is not a strictly linear function of the OH number density. This is due to the locally changing thermodynamic conditions. The front seen on the PLIF images however, can clearly be associated with that sharp rise. Figure 6.13 shows the triple point structure with its theoretical area of high OH-concentration. The location of the leading shock is unknown in the PLIF images, but the shock can be assumed to be right ahead of the reaction front. This is confirmed

by the simulations of the reaction-front and the simultaneous schlieren-PLIF images. The keystone geometry of lower fluorescence is bordered upstream by the incident shock, on the side by the slip streams and downstream by the reaction front. One half of the keystone geometry of higher OH-fluorescence intensity is always pointing in the direction, in which the attached triple point is moving. The triple point is most likely be located slightly upstream from the keystone corner in direction of the shear layer. This is also confirmed by simultaneous schlieren images. The lines with reduced fluorescence intensity leading into the region with high fluorescence seem to correspond to the shear layers.

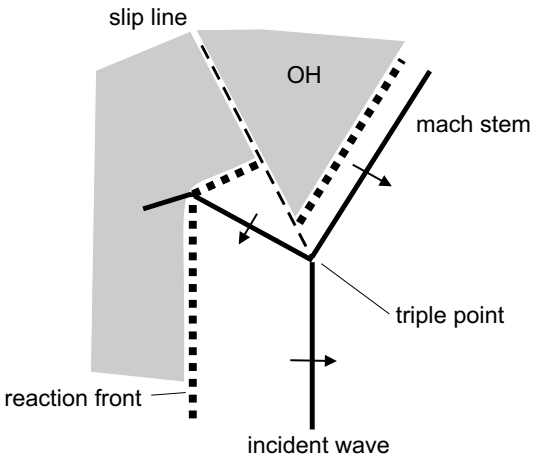

Figure 6.13: Detail of the triple-point structure: Regions of chemical reaction taking place, and therefore high OH concentration, are shaded in gray.

Figure 6.14: Configuration of case A and case B observed experimentally, corresponding to the light sheet orientation shown in Fig. 6.15

Two types of configurations seen on the PLIF images can be distinguished: Discontinuities at the OH-front in the form of keystone halfs of higher fluorescence pointing to each other along the front (case A, e.g. shot 1419, 1420), which lead to the keystone shaped geometry of lower fluorescence, and discontinuities in form of keystone halfs of higher fluorescence pointing in the same direction (case B, e.g. shot 1417, 1428), see Appendix C, p.119. Two cases of light sheet orientation with respect to the transverse waves can be distinguished, which may correspond to the cases A and B (Fig. 6.15). Case A: The light sheet subsequently intersects

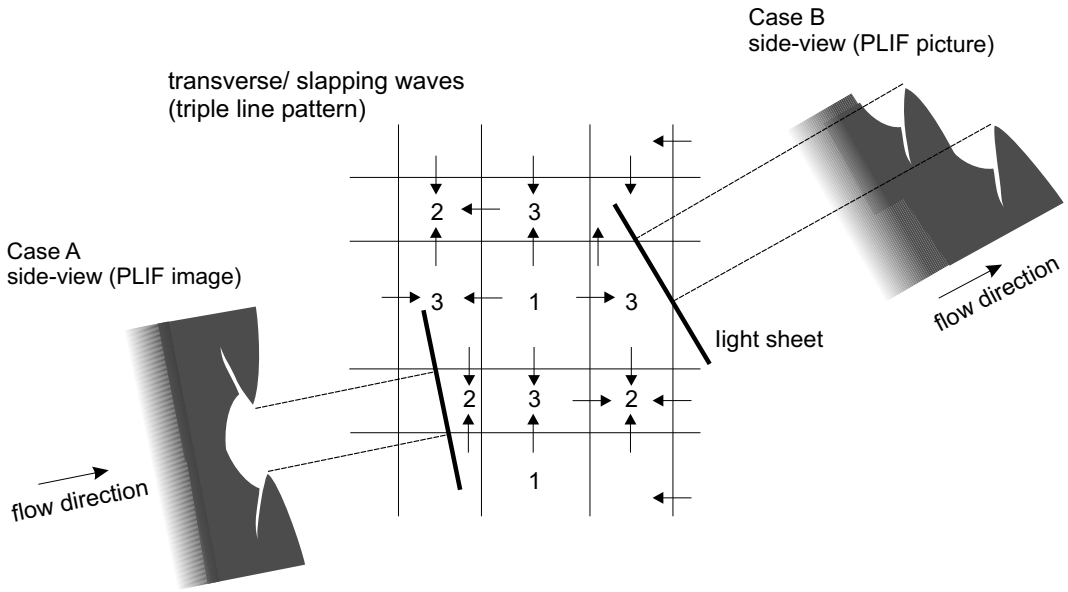

Figure 6.15: Different types of possible geometries (case A and B) observed on the PLIF images and corresponding light sheet orientation with respect to the transverse waves.

two transverse/slapping waves, whose velocity components parallel to the light sheet plane have different orientation. Case B: The velocity components have the same orientation. In case B a cell of type 3 has to be intersected by the light sheet. Combinations of cases A and B were also observed, Fig. 6.14. It is worth noting, that the copped geometries in case B are mostly observed close together, e.g. Fig. E.3, p.132. For that reason the geometries seen on the PLIF images might also arise in case B as well from the strong triple point structure (Fig. 2.9(b), p.14).

The feature seen in the enlarged images in Fig. 6.16 represents the stage in the cell cycle where two triple points collide and a new cell begins, see Fig. 2.7, p.10. In an ideal case this stage in the cell cycle would be observed for all cells along the front, since for a perfectly regular cellular pattern, half of the cells along the detonation front are closing and half of them are opening at the same instant. In the experiment this was not observed due to disturbances in the regular cell structure and the three dimensional behavior of the detonations. In some cases the reaction-front of the opening cell is seen already, before the reaction-front behind is completely closed. The keystone of lower fluorescence is in this way closed by the triple point colliding ahead leaving a closed region of lower fluorescence behind. These regions appearing

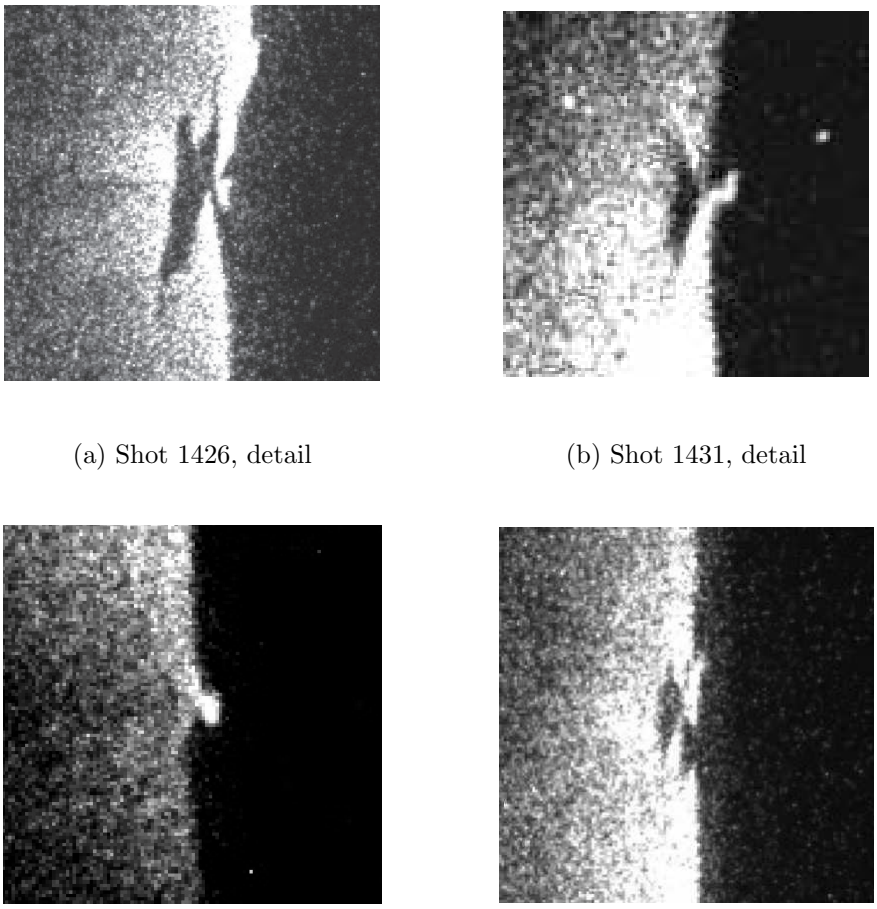

(a) Shot 1426, detail

(b) Shot 1431, detail

(c) Shot 1417, detail

(d) Shot 1421, detail

Figure 6.16: Collision of two triple-points.

on the PLIF images must not be necessarily completely three-dimensionally enclosed unreacted volumes. This can, due to the unknown light sheet-orientation with respect to the wave system, with this setup not be determined.

Depending on the angle between the light sheet and the intersected transverse wave, the detailed triple point geometry appears stretched in the vertical direction. In the limiting case the propagation direction of the transverse wave is perpendicular to the light sheet. In this case the keystones can not be observed anymore. Vertical coherence e.g. in the form of stripes occur in the image instead, Fig.6.17. The configuration seen in Fig. 6.18a can be interpreted as such a case where the slapping wave is sweeping in transversely in the direction perpendicular

to the plane of the image. The reaction zone behind that wave appears as a vertical line. Whether the island of lower fluorescence is three dimensionally closed or whether is connected to the unburned gas ahead of the reaction front in a plane in front or behind the light sheet layer can not be determined from that image.

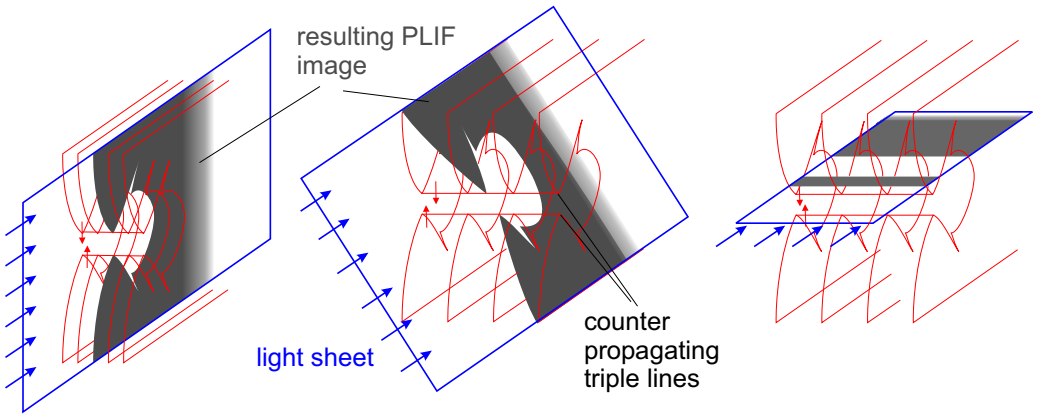

Figure 6.17: Effect of angle between propagation direction of transverse wave and light sheet. The angle is increasing from left to right, respectively $0°, 45°, 90°$. The angle between the triple line and transverse wave is the complement of 90°.

For nitrogen diluted mixtures the reaction zone appeared to be more distorted, which was expected considering the larger range of cell sizes measured by soot foils. The keystone features are still observed even though the smooth parts of the separation line between regions of higher and lower fluorescence are sometimes interrupted by smaller discontinuities. These could be a result of weaker wave structures within a cell. This is observed to be most pronounced in mixtures with higher amounts of nitrogen dilution, Fig. 6.18b. It might also arise from a three dimensional effect of the wave structure. These discontinuities can also be interpreted as signs of cellular substructure, where cells within a cell can occur.

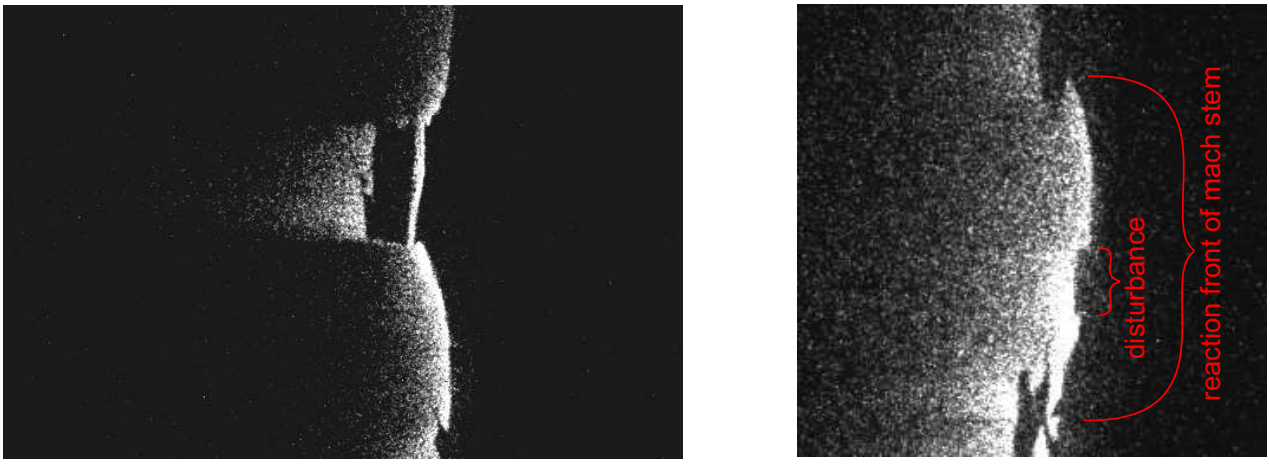

(a) Shot 1427

(b) Shot 1426, enlarged detail

Figure 6.18: a) 60% N_2, possible constellation where transverse wave is sweeping in perpendicular to the light sheet. b) 65% N_2, interrupted smooth reaction front of a Mach stem within a cell.

6.6.2 Simulations and Quantitative Considerations

One dimensional numerical calculations have been performed in order to quantify the features observed in the PLIF images and verify the interpretation of the experimental results. All calculation were done with the one dimensional ZND-code [She86] based on the reaction-kinetics of CHEMKIN II [KRM89]. Of main interest here are the OH-concentration and the induction period, since they are connected to the fluorescence intensity and geometry seen in the PLIF images. The OH concentration profiles calculated for a CJ detonation in the mixtures experimentally investigated together with the pressure and temperature profile are shown in Fig. 6.19 - 6.21. The temperature and the pressure profile rise abruptly through the shock wave. In the induction zone the thermodynamic conditions stay constant. The temperature continues to rise behind the induction zone due to the energy release while the pressure is constantly decreasing. The absolute and relative OH-concentration profile shows a sharp rise at the end of the induction zone and reach their maximum shortly after the end of the induction zone. The relative OH-concentration decays after reaching the flat maximum only slowly. The OH number density is, due to the falling pressure and rising temperature, decreasing faster after reaching a comparatively sharp maximum, reaching for the lower diluted

mixtures after 2 cm 60% of the maximum value. The decrease for higher amounts of diluents is slower. The calculated OH number density maximum increases for all mixtures studied super-proportional to the amount of fuel. Comparing the 45%-N_2 with the 65%-N_2 mixture, the maximum increases by 118% whereas the fuel amount only increased by 71%.

The PLIF images are more qualitative then quantitative, since there is no strictly linear functional dependence between the local fluorescence yield and the local OH number density. The main reasons are:

- The fluorescence intensity is not exactly proportional to the OH-concentration, since locally varying quenching effects influence the signal strength. For a quenching independent signal LIPF has to be used, (4.3.4, [Eck96]. The changing thermodynamic conditions behind the reaction-front influence the fluorescence intensity in the here applied PLIF.
- Absorption of light sheet energy by OH-molecules lowers the energy in the upstream-direction, since the light sheet enters from the downstream-direction.
- The population of the ground state varies with the changing thermodynamic condition.
- The incident light sheet gets refracted, especially due to the large refractive index near the UV region. Depending on the direction in which the light sheet gets deflected this can lead to a more fuzzy image, corresponding to a bigger light sheet thickness, or to shadows and regions of higher fluorescence, corresponding to deflections within the light sheet plane. Due to the absence of caustics and shadows this seems to have a minor influence.

A precise quantitative comparison of the calculated profiles with the experimentally obtained PLIF images is for the above mentioned reasons not possible. In order to obtain a qualitative comparison of the OH profile along the flow direction the intensity profile was measured by averaging the intensity of the PLIF-pictures vertically in a 40 pixel wide, horizontal stripe. This stripe was vertically adjusted such that it only intersected smooth parts of the reaction front. Two positions of the vertical stripe can be distinguished: Either the stripe intersects a keystone of lower (stripe on top in Fig. 6.6.2) or of higher fluorescence (stripe on bottom). These measured intensity profiles were averaged for each type of mixture and are shown in Fig. 6.24. Qualitatively the profiles correspond largely with the calculated profiles. They both

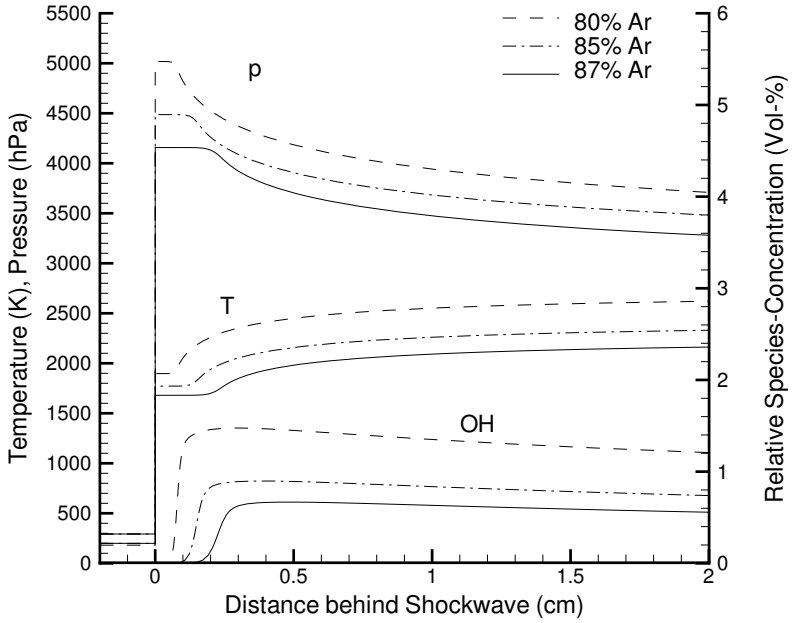

Figure 6.19: OH concentration and thermodynamic conditions for the experimentally investigated Argon-diluted mixtures behind the shock of a CJ detonation.

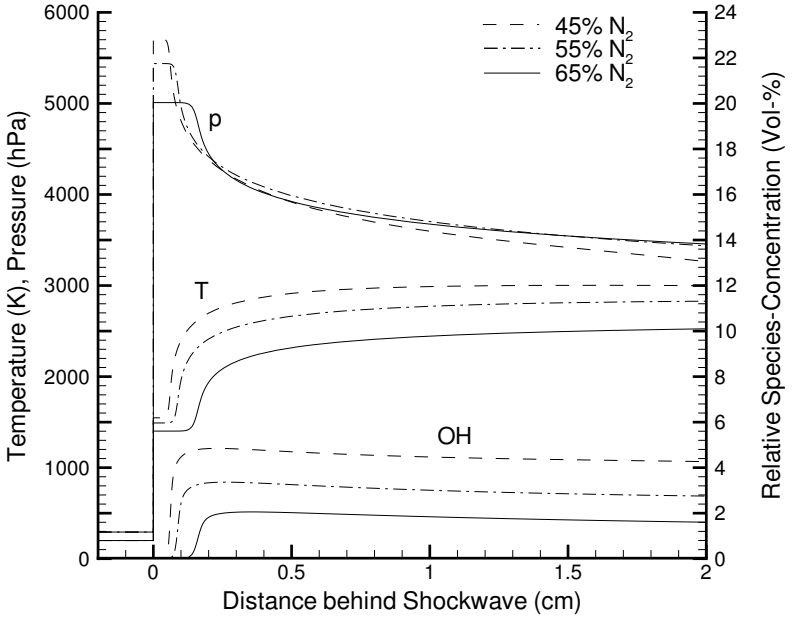

Figure 6.20: OH concentration and thermodynamic conditions for the experimentally investigated Nitrogen-diluted mixtures behind the shock of a CJ detonation.

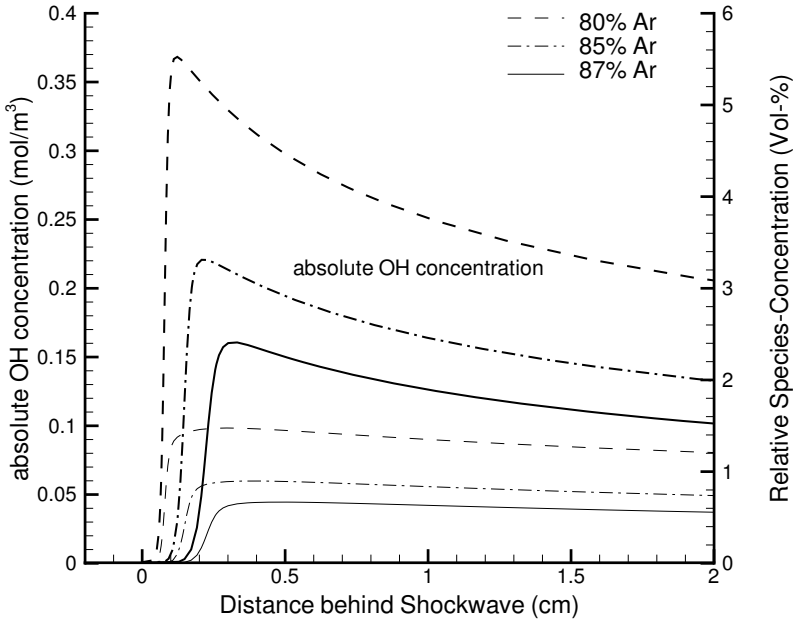

Figure 6.21: Absolute and relative OH concentration for the experimentally investigated Argon-diluted mixtures behind the shock of a CJ detonation.

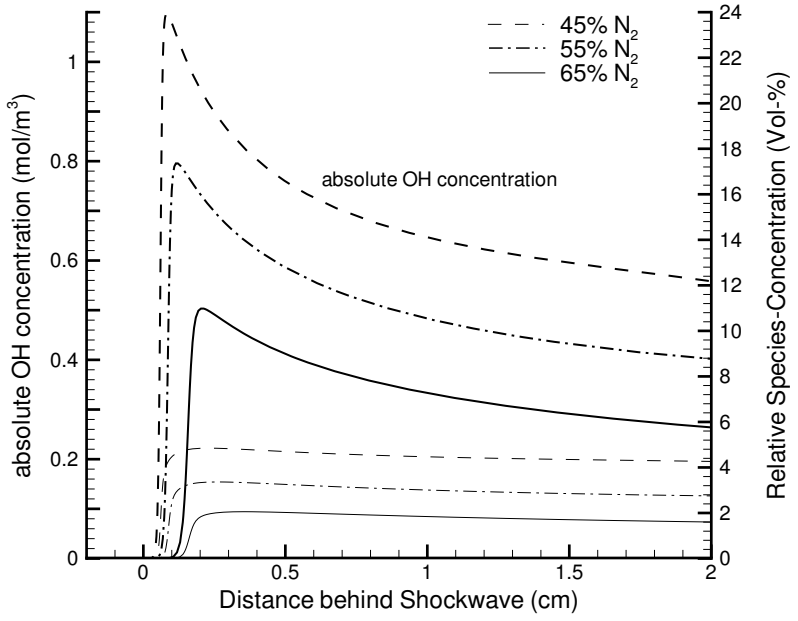

Figure 6.22: Absolute and relative OH concentration for the experimentally investigated Nitrogen-diluted mixtures behind the shock of a CJ detonation.

rise sharply to their maximum, and then slowly decay. The decay of the fluorescence intensity profile is stronger and reaches values close to the background noise, whereas the calculated profile still shows values of about 60% of the maximum OH-concentration. This can be caused by the gradual absorbtion of light sheet energy. Noteworthy is also that the ratio of the peak OH concentrations for 80% and 85% argon diluted mixtures are, neglecting the background noise, in reasonable agreement. This could be due to the fact that the light sheet intensity is the same, since nearly no absorbtion took place, and the thermodynamic condition are comparable at this point.

In general interactions of transverse waves with the reaction zone behind the leading shock are neglected in the calculated profiles. This also has to be considered when comparing the calculated and measured profile. The intensity-profiles measured for each stripe are shown in appendix. D (p.129). The intensities profiles obtained from each stripe vary strongly. This probably originate from the timing uncertainties and the varying output energy from the laser, which lead to an over-all decrease in fluorescence intensity and the particular position of the stripe. If the stripe located in the wings of the light sheet, the fluorescence intensity measured is much lower than in the center region of the light sheet. Furthermore, the OH-profile varies with the leading shock velocity. For shock-velocity slower than the CJ-velocity the OH-profile is gradually flattened out. For overdriven waves the OH profile shows an sharper rise and higher maximum, Fig 6.6.2. Since the leading shock velocity depends on the stage in the cellular cycle, the measured intensity profile for each stripe depends also on the cellular cycle stage of the front section intersected by the stripe. The maximum fluorescence intensity profiles measured might for that reason be measured in stripes intersecting keystones of higher fluorescence. The averaged intensity profile shown in Fig. 6.24 corresponds not to the average of detonations at CJ-velocities, but to the average of the range of velocities in a cellular cycle. The dependence of the stage in the cellular cycle and the geometry revealed on the PLIF images is discussed further on.

Some fluorescence intensity profiles measured show a small rise in intensity already ahead of the previously described sharp rise, Fig. 6.25. This might be chemiluminescence occurring mainly in layers outside the light sheet layer since the reaction front elsewhere can be ahead of the one in the light sheet layer. It could as well be weak OH-fluorescence within the induction

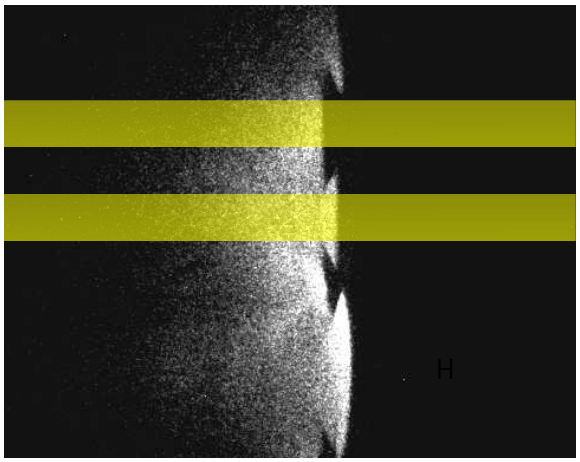

(a) Measurement of intensity profile in PLIF images by vertically averaging the intensity obtained in a thin strip, located on smooth parts of the reaction front.

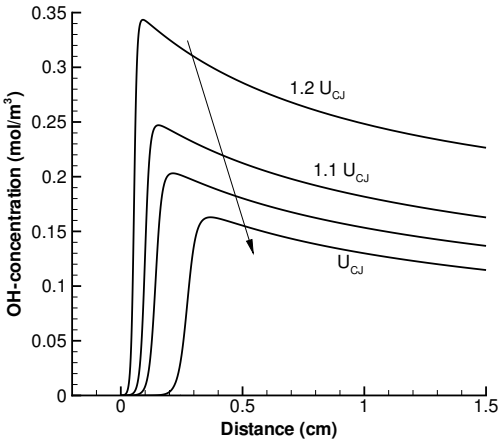

(b) OH profile for 85% Argon diluted mixture with varying leading shock velocity.

Figure 6.23:

zone between the incident shock and the sharp OH fluorescence front at the beginning of the reaction zone, since radicals are build up already in the slightly endothermic induction zone. The distance of around 4 mm between the initial small rise and the bigger sharp rise in fluorescence intensity seen in that particular profile (Fig. 6.25), corresponds to the calculated induction zone length at CJ conditions (6.34). Never the less according to the ZND simulation the OH concentration rising in the induction zone is four orders of magnitude smaller than the maximum OH-concentration. Therefore it is unlikely that the OH number densities in the induction zone get detected at all, and more likely that the detected signal is chemiluminescence - especially since the signal intensity of about 580 counts is similar to the ones measured in chemiluminescence experiments.

Despite the missing proportionality of the fluorescence signal and OH number density the sharp boundary between regions of higher as lower fluorescence seen in the PLIF images matches in a good approximation the sharp rise in the OH profile seen in calculations. This enables to analyse the geometry of the reaction zone boundary observed on the PLIF images.

The distance between two transverse waves, moving in the same direction is called transverse wave spacing (sec. 2.5, 8). Since the transverse waves are joining the triple points, in the

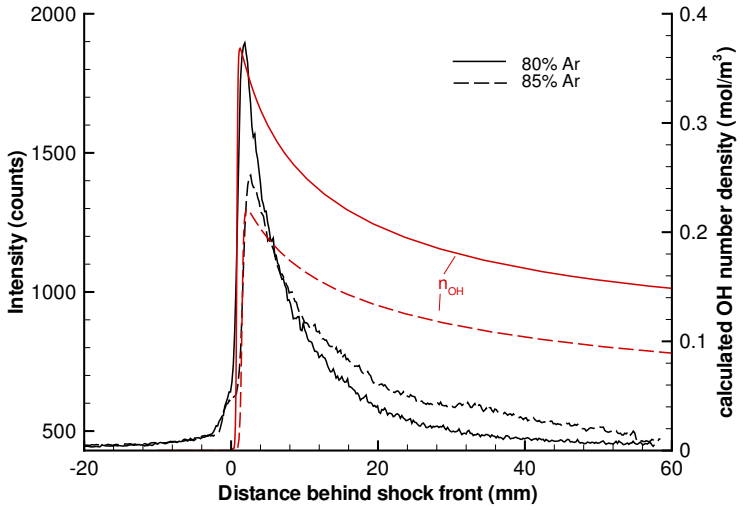

(a)

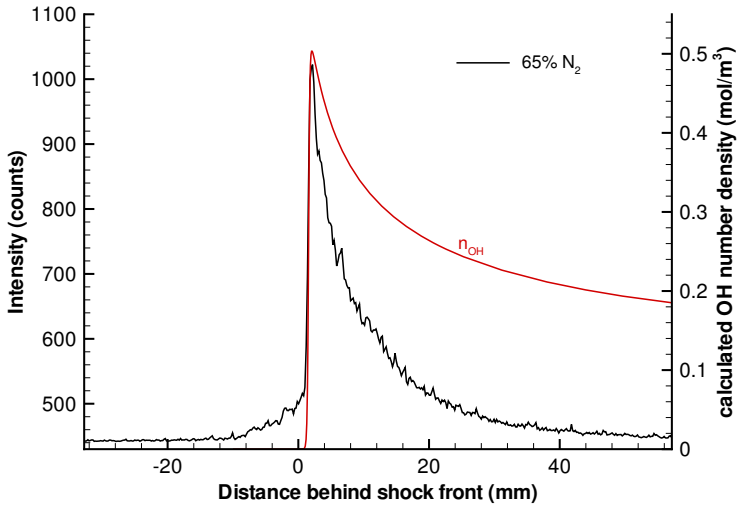

(b)

Figure 6.24: Measured signal intensity averaged over all shots of one mixture in comparison to the calculated OH number density. Since the shock location of the PLIF images is unknown, the distance scale for the measured intensity profile is set in such a way that the distance between maximum fluorescence increase and the assumed shock front is the induction zone length at CJ conditions.

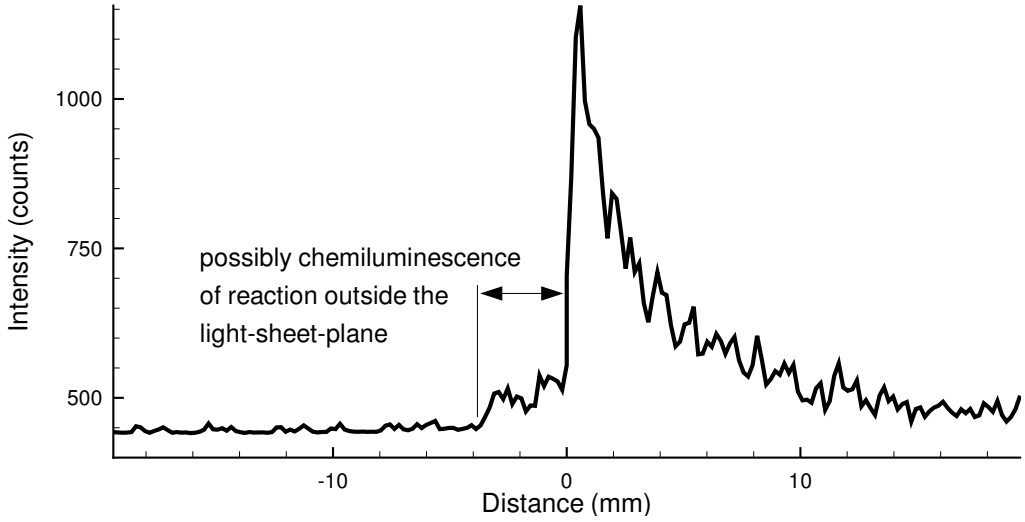

Figure 6.25: Single profile of shot 1428 (65% N_2). The increased intensity ahead of the front could be due to chemiluminescence.

context of the PLIF images it can be seen as the distance between two triple points moving in the same direction, Fig.6.6.2. In an ideal case (perpendicular grid of triple lines) the transverse wave spacing is constant at any time and equal to the cell width λ.

For obtaining the transverse wave spacing from the PLIF-pictures the distance of two non-adjacent tips of keystone corners pointing in the same direction was measured, Fig 6.6.2a. The triple points are not exactly located at the corner of the keystone, but slightly ahead in the direction of the shear-layer, see Fig. 6.13 p.85. This is a source of error for this kind of measurement, but the error arising from both triple points are not accumulated errors, since the shift takes place in the same direction. This transverse wave spacing measured from the PLIF images in that fashion is for nearly all shots smaller than the cell size λ and obtained by the side soot foils and show a much larger scatter than the soot foil measurements, Fig. 6.28. That is most probably due to the three-dimensional behavior of the front, visualized in only the light sheet plane. Only if the triple lines, which are intersected by the light sheet, have no velocity component out of the light sheet plane the real distance of the transverse wave spacing can be measured, Fig. 6.27, neglecting the previously mentioned source of error. As shown by the endplate soot foil the transverse waves system in much more unstructured than shown in Fig. 6.27, making an orthogonal alignment unlikely. The orientation of the triple lines with respect to the light sheet plane is unknown in all PLIF-pictures, and can only be

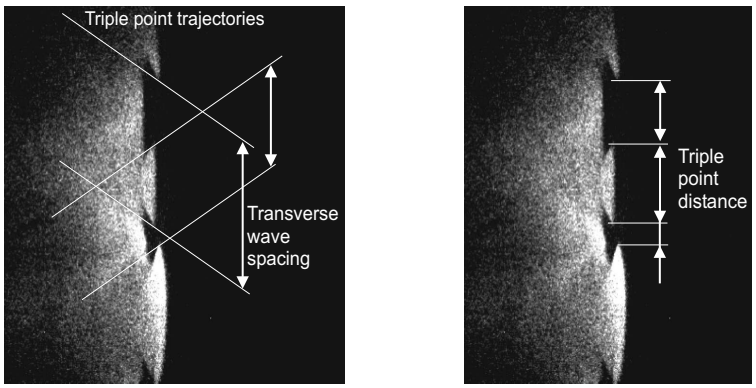

(a) (b)

Figure 6.26: Nomenclature of distances obtained from PLIF images.

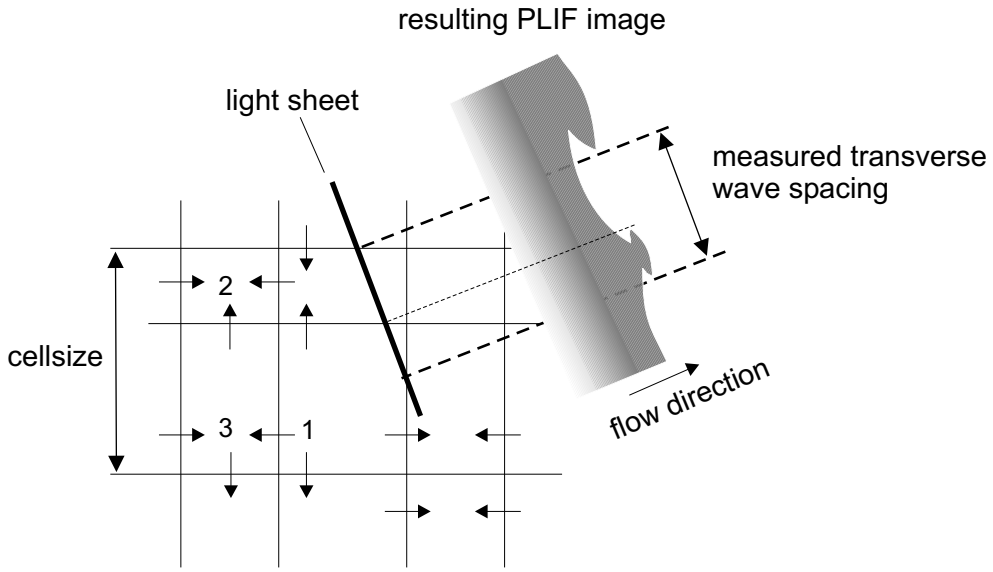

Figure 6.27: Possible effect resulting in differences of measured transverse wave spacing and actual cell size.

qualitatively estimated (see Fig.6.17).

In order to quantify the changing induction zone length caused by the variations of the shock-velocity along the front ZND-computations were carries out. The distance between the shockwave and the location of maximum OH-production ($\delta OH \,/\, \delta x \;=\; max.$) [She86] is here

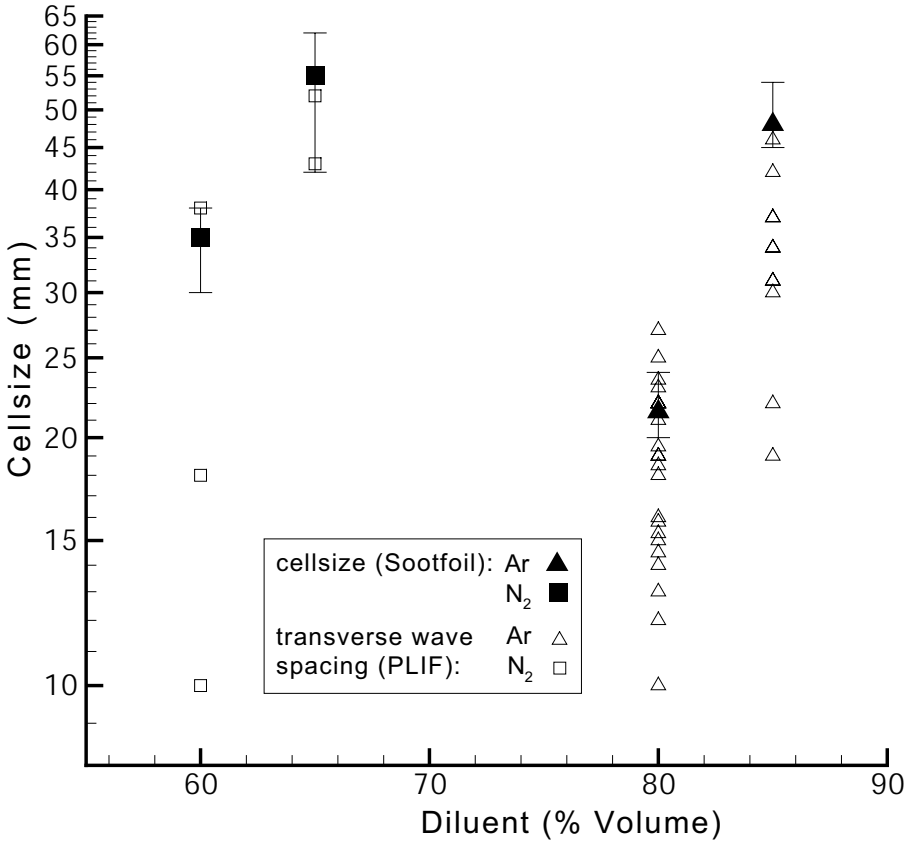

Figure 6.28: Comparison of cellsize obtained by side soot foils and transverse wave spacing obtained by PLIF images.

defined as the induction zone length. Two different detailed reaction mechanisms (*Warnatz*, *Baulch*) [SS99] were used, which gave very similar results for both diluents, Fig. 6.29 and Fig. 6.30. For slower shock velocities the induction zone length increases rapidly, Fig. 6.31 - 6.34. This can be explained by the squared dependence of the temperature in the strong shock limit and assuming for the reaction time an Arrhenius relationship [SS99]. Note the logarithmic scale for the induction zone in the plots.

The aim of the following qualitative analysis of the front geometries on the PLIF images is to quantify the induction zone and the stage in the cell cycle. Afterwards the results are normalized and compared to a two dimensional numerical simulation of a similar mixture.

The vertical distance between two adjacent triple points moving in opposite directions is here

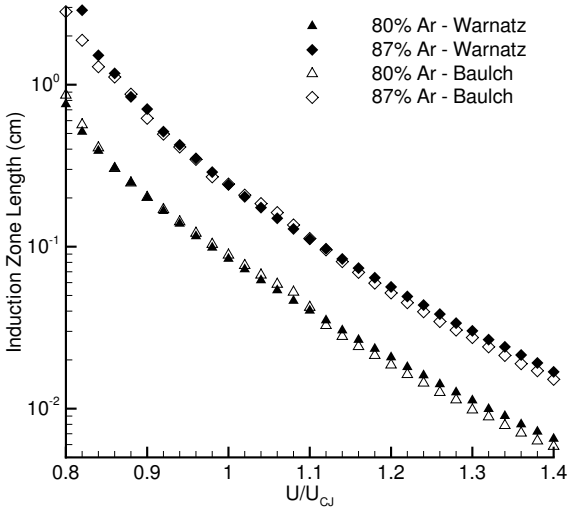

Figure 6.29: Comparison of Warnatz and Baulch reaction mechanism for Argon-diluted mixtures.

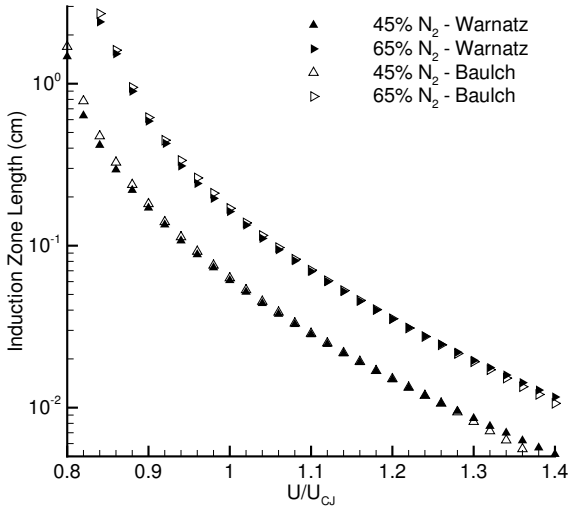

Figure 6.30: Comparison of Warnatz and Baulch reaction mechanism for Nitrogen-diluted mixtures.

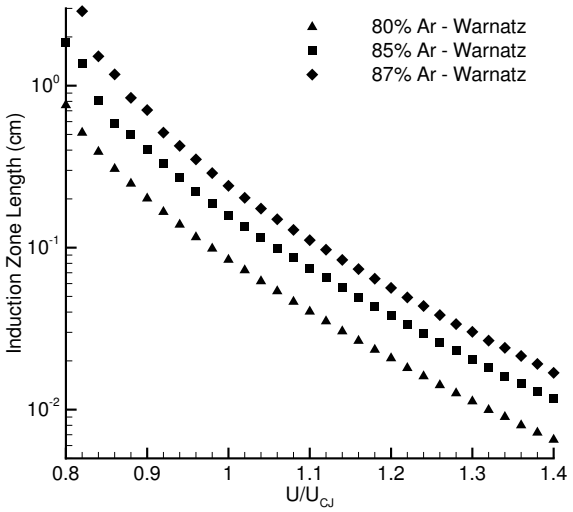

Figure 6.31: Induction zone length (Warnatz) for all Argon-diluted shots.

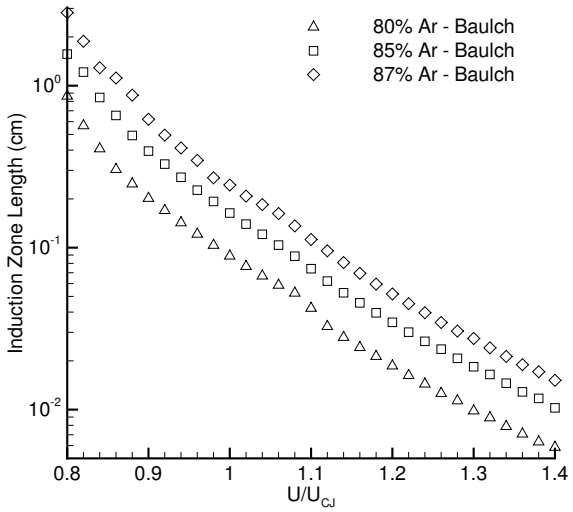

Figure 6.32: Induction zone length (Baulch) for all Argon-diluted shots.

called triple point distance. The triple point distance, in contrast to the transverse wave spacing, changes during one cellular-cycle: It is equal to 0 at the beginning of the cell and half way through the cell it reaches the maximum λ, the cell width. The triple point distance is measured from the PLIF images as the distance between two keystone corners pointing in

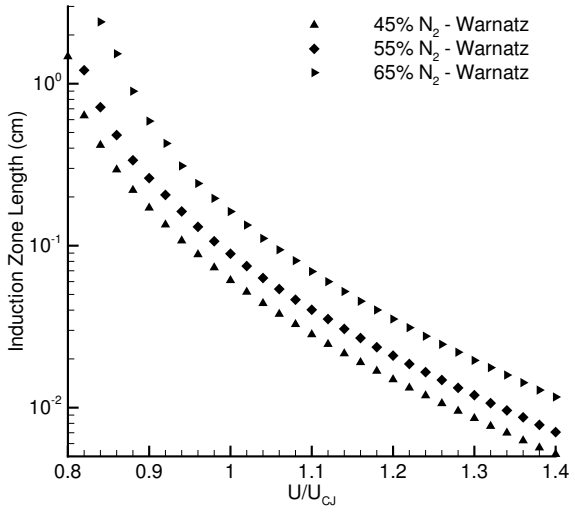

Figure 6.33: Induction zone length (Warnatz) for all Nitrogen-diluted shots.

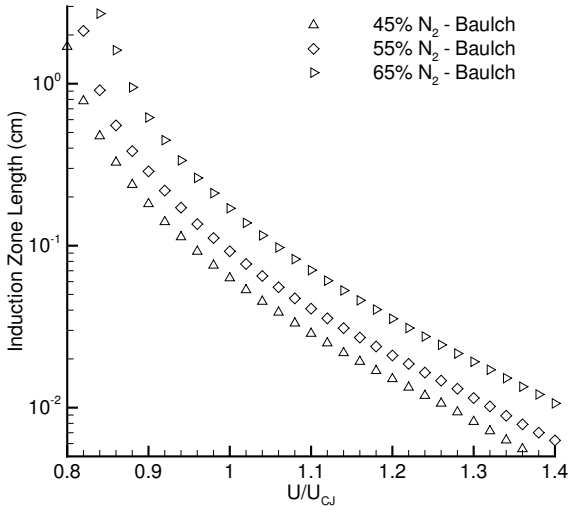

Figure 6.34: Induction zone length (Baulch) for all Nitrogen-diluted shots.

opposite directions. As previously mentioned in the context of the transverse wave spacing the mismatch of keystone corner seen on the PLIF-image and triple point lead to an error source, see also Fig. 6.13 p.85. The error made in the measurement of the triple point distance is larger, since the shift at each keystone corner is in this case an accumulative error. The in such a way quantified measured triple point distance is for closing cells always larger than for the effective triple point distance. The magnitude of that error depends all well on the stage in the cell cycle of the adjacent cell since the shift between keystone corner and triple point is a function of the induction zone length of the adjacent cell and the track angle. For smaller triple point distances and closing cells the error is likely to be largest, since the induction zone length of the adjacent cell is largest.

The measured triple point distance is normalized by the cellsize measured from soot foils for each mixture. From the normalized triple point distance the normalized distance within a cell can be derived. The normalized distance in a cell is defined as $(x - x_0)/l$, with x the absolute distance, x_0 the cell origin and l the cell length. Assuming a track angle which is not changing significantly in a cell-cycle, as seen on side wall soot foils, the normalized triple point distance is linearly connected to the normalized distance. For the closing half of the cell a normalized triple point distance of 1 (0) corresponds with a normalized distance of 0.5 (1). With this assumption the stage in the cellular cycle can therefor be calculated for cells marked by keystones of lower fluorescence and analog for higher fluorescence (normalized cell length

between 0 and 0.5). For reasons given further on only the keystones of lower fluorescence will be considered in the further analysis.

The majority of the PLIF images were acquired without simultaneous schlieren imaging. Therefore the distance between shock and OH-front cannot be measured directly. To estimate the induction zone length a line between the keystone corners was assumed, Fig. 6.35 dashed line. The actual incident shock is a certain distance ahead (downstream) of this line. This distance changes depending on the cell cycle stage and is in a good approximation equal to the induction zone length of the adjacent cell cut by the light sheet, visible on the PLIF image on the top and/or bottom. The maximum distance measured parallel to the flow between the dashed line and the OH-front lagging behind is here called key stone depth, see Fig. 6.35. This quantity can obviously only be measured for keystones of lower fluorescence. These cells analysed were therefore assumed to be in the closing half of their oscillation cycle with a normalized distance between 0.5 and 1, calculated from the triple point distance measured. A plot of the keystone depth measured over the normalized cell distance is shown in Fig. 6.36. The normalized cell distance calculated was for nearly all data point bigger than 0.75, which indicated that the triple point distance measured was mostly smaller than half of the cell size measured. This tendency to smaller triple point distances compared to the cell size was also seen in the transverse wave spacing measurements from the PLIF images (Fig. 6.28), and can be probably explained by the light sheet orientation with respect to the cell (Fig. 6.27).

The key stone depths measured for the 85% Argon diluted shots were in general bigger than the ones for 80% Argon. That is probably due to the increasing induction zone length with increased amount dilution seen as well in the calculations, see Fig.6.31 p. 99. The scatter for the keystone depth measured is very large and a trend line is difficult to determine. For the 80% Argon diluted mixture the scatter is smallest and the data shows tendency to larger key stone depth for higher normalized cell distance.
The following has to be considered for the analysis:

- The normalized distance within the cell is not measured directly but calculated from triple point distance measurements, which includes the previously described errors. Further more the triple point distance is due to the oblique transverse wave orientation with respect to the light sheet not necessarily representative of the stage in the cell cycle and

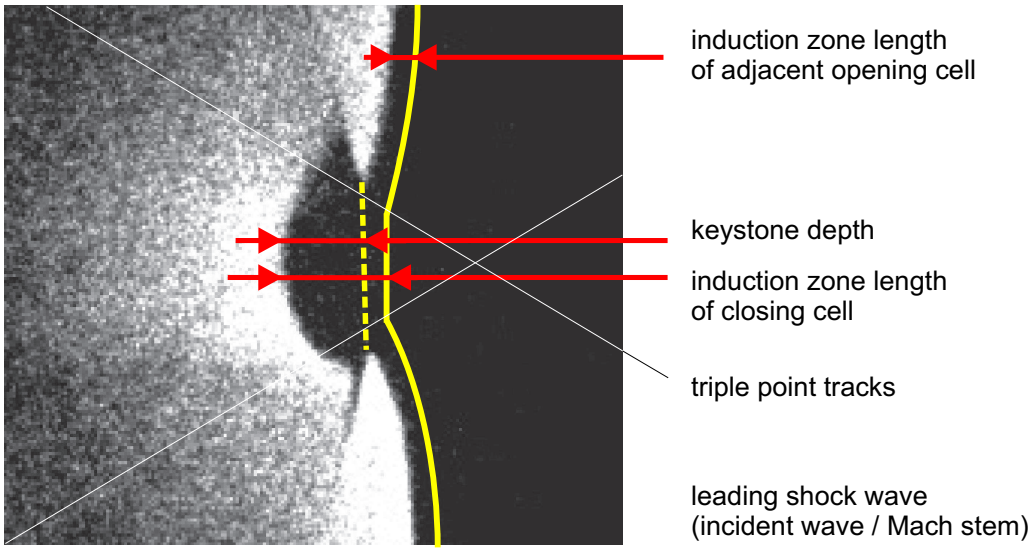

Figure 6.35: Keystone depth measured on the PLIF images. The transverse waves are not sketched, but reach back from the triple points.

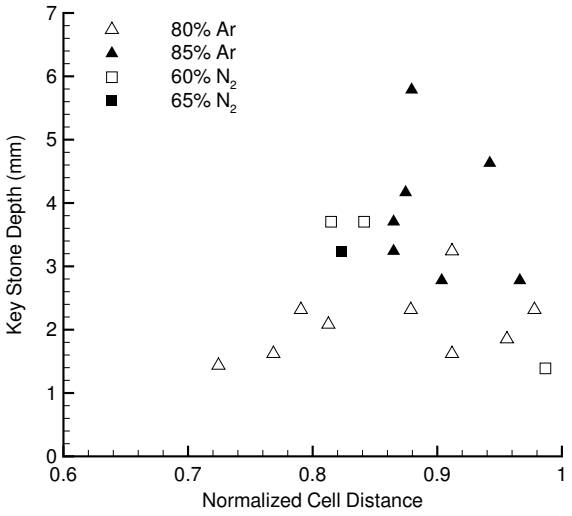

Figure 6.36: Keystone depth measured over the normalized cell distance. The normalized cell distance was calculated from the triple point distance measured as described in the text.

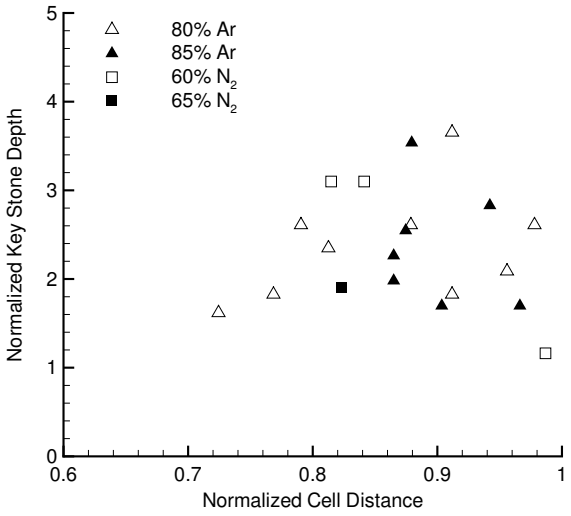

Figure 6.37: Keystone depth normalized by induction zone length at CJ condition.

therefore for the normalized cell distance, Fig. 6.27. These three dimensional effects and the mentioned sources of errors are the main reasons for the large scatter in the plot seen in Fig. 6.36.

- Only cells in the second half of their oscillation cycle or, in other words, only keystones of lower fluorescence, can be analysed.
- The induction zone length for a certain stage in the cell cycle can neither be measured directly, nor deducted. The only information gained is the key stone depth distribution over the normalized cell length. However, the results can be compared to a two-dimensional numerical simulation.

To compare these results with a two dimensional numerical simulation, the keystone depth for the numerical simulation has to be calculated. Since the mixture used in the numerical simulation is not identical to the mixtures used in the experiment, and to compare the different mixtures used in the experiment, the key stone depth can be normalized by the induction zone length calculated at CJ conditions for each mixture. A plot of the measured normalized keystone depth is shown in Fig.6.37.
A two dimensional numerical simulation for a stoichiometric $H_2 - O_2$ diluted with 70% Ar at 6.7 kPa was carried out by Eckert [Eck00]. A plot of the shock velocity through one cell cycle is shown in Fig. 6.38. The shock-velocity decreases sharply and reaches at 0.25 normalized cell length already CJ conditions. The velocity decay is from then on much slower and reaches close to the end of the cell a value of 90% of the CJ-velocity. The induction zone, also plotted, is accordingly increasing steeply at the beginning of the cell and further on flattening. For a normalized cell distance over 0.75 the induction zone length stays approximately constant. The main change of the induction zone length happen in the first half of the cell cycle.

To calculate from this simulated induction zone length the keystone depth of the simulation, one has to consider the induction zone of the adjacent cell. In an ideal case, as in the simulation, the normalized distance of the adjacent cells is shifted by 0.5, since the cell on the top and bottom of a certain cell starts, when the cell itself is in the middle of the cellular cycle. The induction zone length for the adjacent cell is thus known. The keystone depth can be calculated by subtracting the induction zone length of the adjacent cell from the induction zone length of the cell investigated, which is closing, Fig. 6.39. The in that fashion

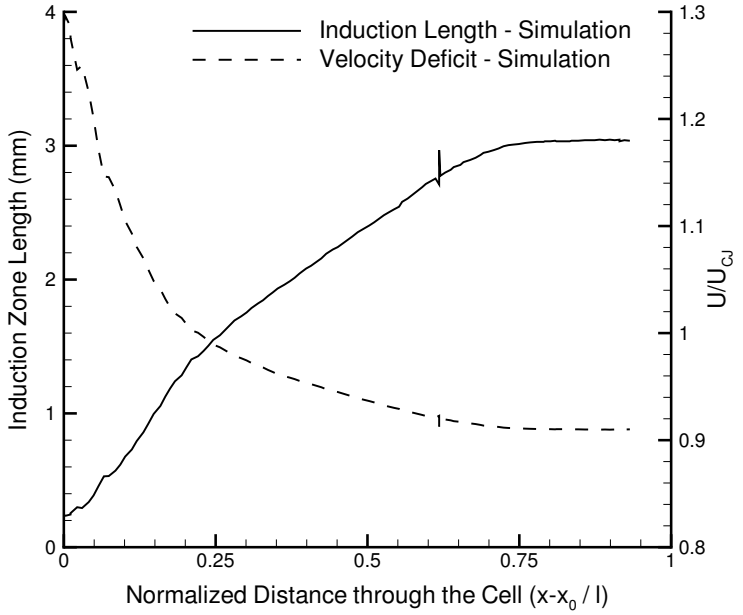

Figure 6.38: Velocity and induction zone length for $2H_2 + O_2 + 7Ar$; 6.7 kPa, [Eck00].

calculated keystone depth, which can be only calculated for normalized distances between 0.5 and 1 is shown in Fig. 6.40. It is noteworthy, that the calculated keystone depth decreases with increasing normalized distance, since the induction zone length of the adjacent cell is increasing more steeply than the then the induction zone length of the cell under consideration. This could also influence the likelihood of the island formation with lower fluorescence after a triple point collision. If the decrease of the keystone depth is rapid enough, the formation of unreacted islands, which where shocked by the incident wave, is unlikely.

Due to the steep increase of the induction zone length of the adjacent cell the stage of the adjacent cell has an major influence on the keystone depth of the closing cell. In the analysis of the experimentally measured keystone depth in the PLIF images, the stage of the adjacent cell could not be taken into consideration - only the stage of the cell itself. In other words: The measured keystone depth is according to this calculation more dependent on the stage of the neighboring cells than on the triple point distance measured. This is a further reason for the large scatter of the experimentally obtained keystone depth plotted against the normalized triple point distance. A plot of the calculated normalized keystone depth and the measured normalized keystone depth is shown in Fig. 6.40.

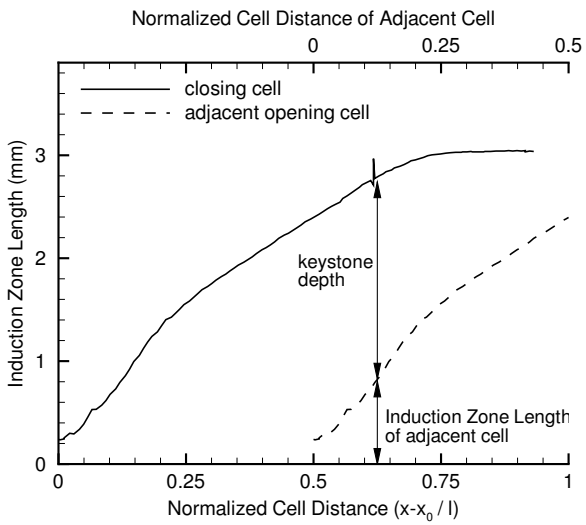

Figure 6.39: Induction zone length obtained from two dimensional simulation (70% Ar, 6.7 KPa) for closing cell and adjacent opening cell. The keystone depth is the difference between both.

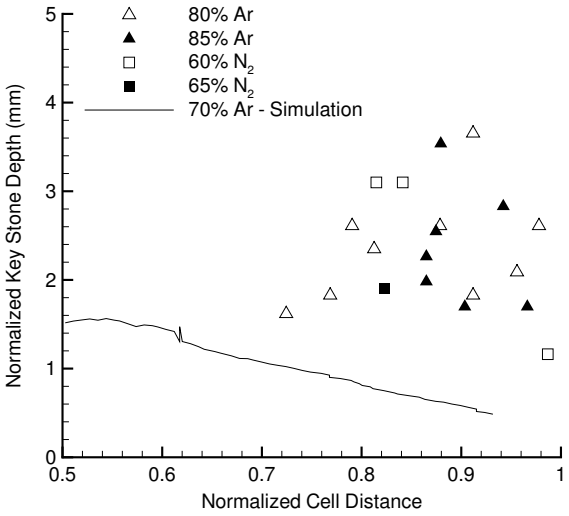

Figure 6.40: Normalized keystone depth calculated from the numerical two dimensional simulation and the experimentally obtained normalized keystone depth.

To conclude: The main problem in the quantitative analysis of the obtained PLIF-pictures is, that the investigated detonations are not rectangular. For this reason the triple-points (triple lines) are mostly moving with a velocity-component perpendicular to the light sheet plane, Fig. 6.27. The triple point distance measured is therefore, including the pointed out shift between triple point and keystone corner, not proportional to the normalized cell distance anymore. This and the mentioned drawbacks of the quantitative analysis explain the big scatter in the plot of the quantities derived from the images. Fore comparison between the experimental results from different mixtures and calculated results, one has to additionally consider that the mixture use in the numerical study had lower initial pressure, and the normalization of the key stone depth by the induction zone length at CJ condition is an approximation. Furthermore, the numerical calculation is two-dimensional where only cell-type 1 and 2, which correspond to cells with cell boundaries (triple lines) all opening or closing respectively (Fig. 6.4, p.77). In the three dimensional detonation cell type 3 occurs on average as often as cell type 1 and 2 together. Therefor its likely that some of the cells observed experimentally are type 3 cells.

However, the shock velocity profile through one of these cells, cannot be derived from the two-dimensional simulation.

6.6.3 Simultaneous Schlieren PLIF images

The simultaneous schlieren and OH-PLIF images confirm the assumed location of the leading shock wave, which is just downstream of the leading fluorescence front. It can also be seen that the discontinuities observed in the OH front on the PLIF images are directly associated with the instability of the detonation front, leading to the cell structure of the front, sometimes called "multi-front". The wave system revealed on the schlieren-image can be correlated with the position of the OH-front seen on the PLIF images, Fig. 6.41. All simultaneous PLIF-schlieren images are shown in Appendix E.

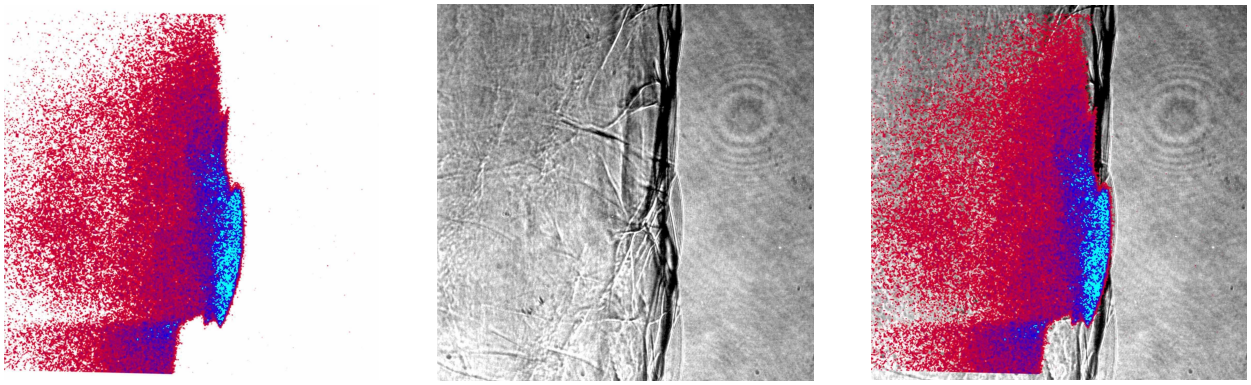

(a) PLIF image

(b) Schlieren image

(c) Superimposed PLIF-schlieren image

Figure 6.41: Simultaneous schlieren and OH fluorescence images behind detonation fronts; Shot 1434, 85% Argon.

Even though the distance of OH-and sock front seem to be measurable on the overlayed schlieren-PLIF images, this observed distance must not necessarily correspond exactly to the induction zone length. On the schlieren image only the over-all leading part of a curved shock front is visible as a sharp line, interpreted commonly as the "shock front". The three dimensional shock front, if curved as confirmed by the schlieren images, can be also located in

regions behind that leading line. The shock-front seen on the schlieren image does therefore not necessarily coincide with the location of the shock in the light sheet plane, leading to a discrepancy between the induction zone and the distance of the OH-front and "shock-front" measured on the overlayed schlieren-PLIF image, Fig. 6.42. The effective induction zone length might be smaller than the distance apparent on the overlayed image. A qualitative analysis of the overlayed images in therefore not possible with the current setup. The three dimensionality of the wave system causes too many unknown variables in both the schlieren and PLIF images to correlate them qualitatively.

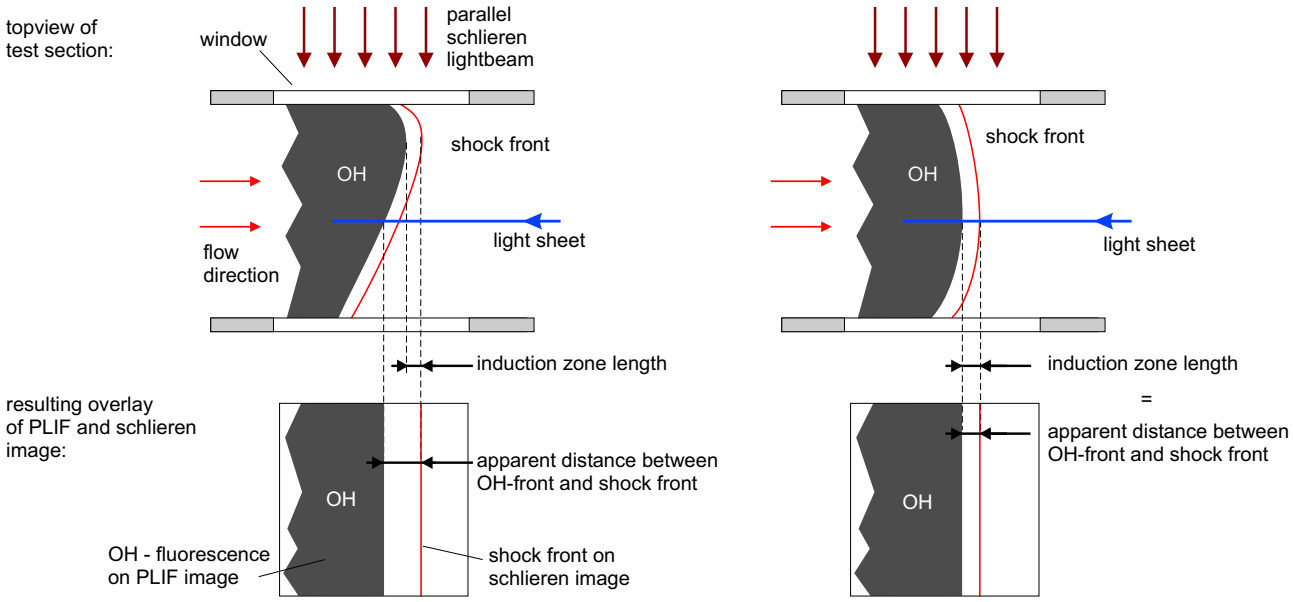

Figure 6.42: Influence of a horizontally curved shock wave on the apparent distance between shock front and OH front on an overlayed PLIF-schlieren image. On the right, the ideal case of no mismatch is shown.

Chapter 7

Summary and Future Work

The reaction zone structure of propagating detonations in nitrogen and argon diluent stoichiometric hydrogen-oxygen have been studied qualitatively with soot foils, schlieren technique and Planar Laser Induced Fluorescence.

For all PLIF-images a distinct OH-concentration front was visible. The OH fluorescence intensities were high enough to neglect chemiluminescence, shown in a simultaneous comparison of chemiluminescence and PLIF technique. For nitrogen diluted mixture the signal to noise ratio was lower than for argon diluted mixtures. The pictures obtained allow detailed qualitative analysis of the OH-distribution with sufficient spatial resolution at the detonation front. The discontinuities in the reaction front are caused by the cellular structure and the corresponding varying shock strength along the detonation front. This is confirmed by simultaneous schlieren and PLIF-images. The creation of keystone shaped regions of lower and higher OH fluorescence intensity in the second half and first half respectively of a cell oscillation is the most outstanding feature, observed experimentally for the first time.

The images obtained are qualitative other than quantitative, since the fluorescence signal is not directly proportional to the OH number density. The fluorescence intensity for LIPF is much smaller [Eck96] than for PLIF, and therefore the signal to noise ratio was too low to apply LIPF as a quantitative OH-concentration measurement technique with the described setup. The limiting factor is the chemiluminescence. The influence of chemiluminescence can be decreased further by a more precise filter-system or by modifying the test section dimensions towards a more rectangular and thinner cross section. Also a reduced jitter from the laser-pulse would allow a shorter gate width for the camera and lower the chemiluminescence intensity on the image.

For quantitative experimental studies of the induction zone length the existing setup has to be modified. The cross section of test section is too big in the lateral direction for a detailed study with schlieren optics. The part of the tube with rectangular cross section should be long enough to ensure mode locking in both dimensions and the development of an orthogonal wave system. The unknown orientation of the transverse wave system with respect to the light sheet is, in the current setup, a too big an error source of error for a quantitative in depth analysis.

Appendix A

Sootfoils

The field of view for all sootfoils shown is 150mm x 150mm. The round sootfoils where placed on the side of the tube, the square ones where placed at the endplate of the testsection.

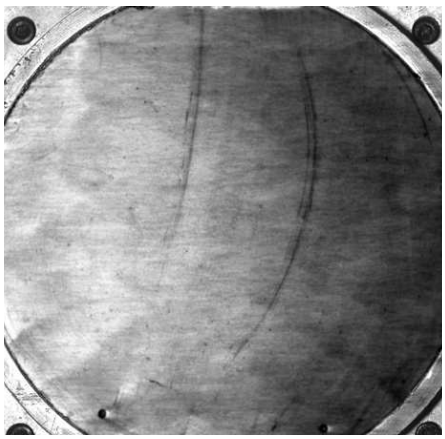

A.1: Shot 1380, 80% Argon

A.2: Shot 1381, 80% Argon

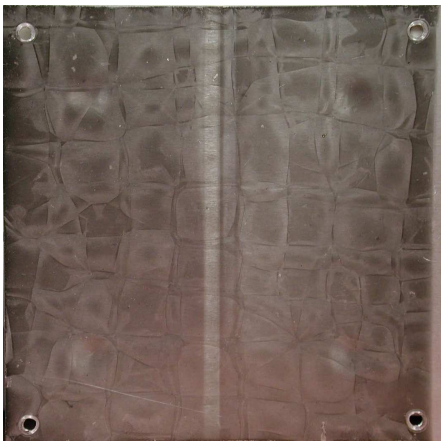

A.3: Shot 1382, 80% Argon

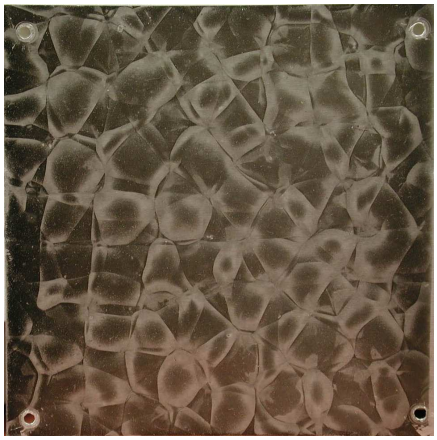

A.4: Shot 1383, 80% Argon

A.5: Shot 1384, 85% Argon

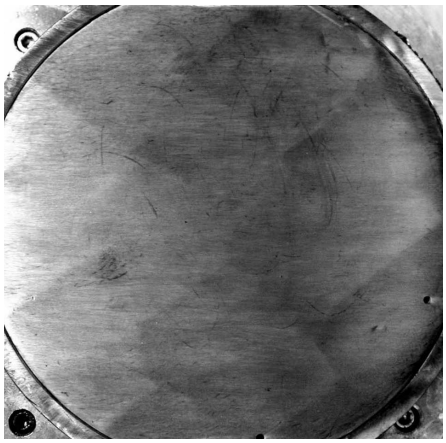

A.6: Shot 1384, 85% Argon

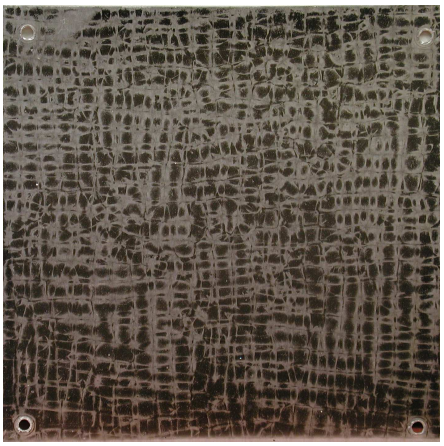

A.7: Shot 1385
$70Ar + 4C_2H_2 + H_2 + 18O_2$

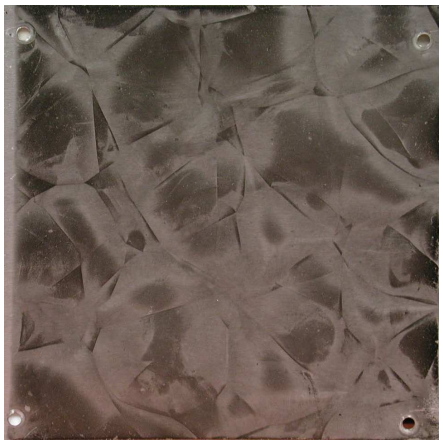

A.8: Shot 1386, 85% Argon

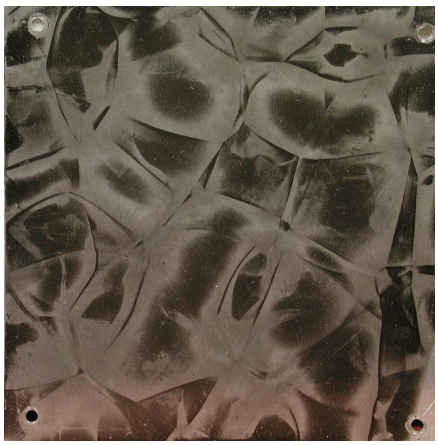

A.9: Shot 1387, 85% Argon

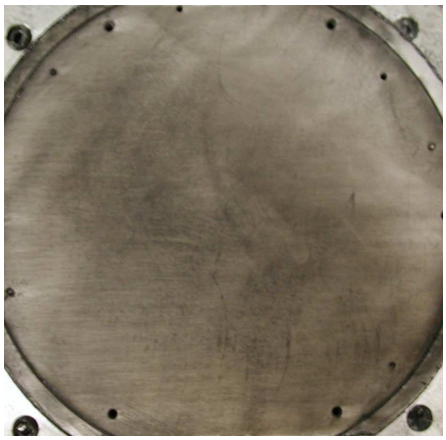

A.10: Shot 1387, 85% Argon

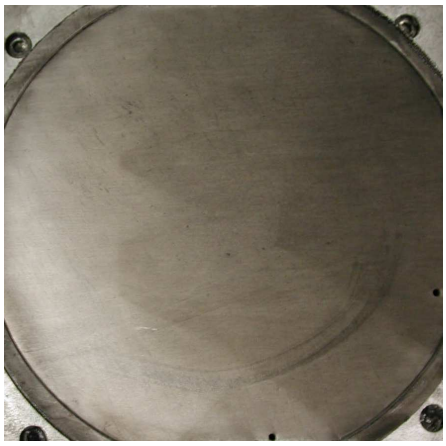

A.11: Shot 1387, 85% Argon

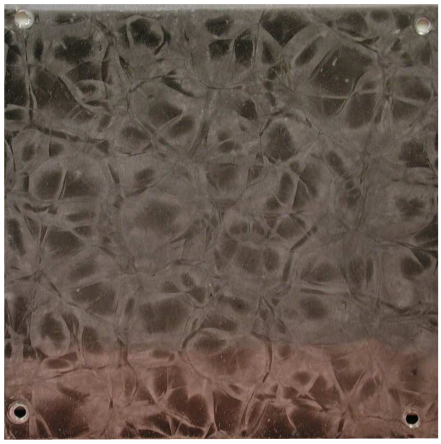

A.12: Shot 1388, 55% Nitrogen

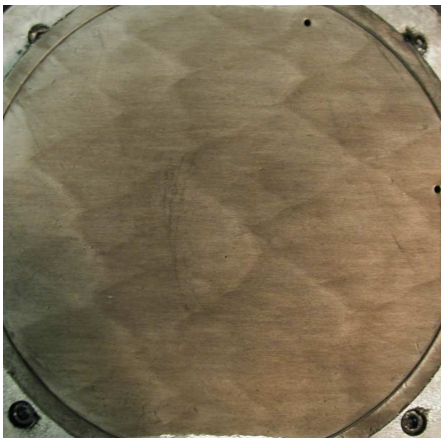

A.13: Shot 1388, 55% Nitrogen

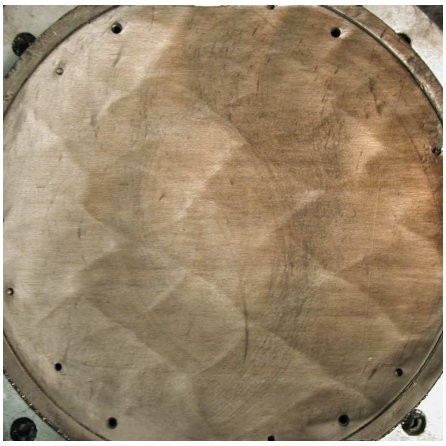

A.14: Shot 1388, 55% Nitrogen

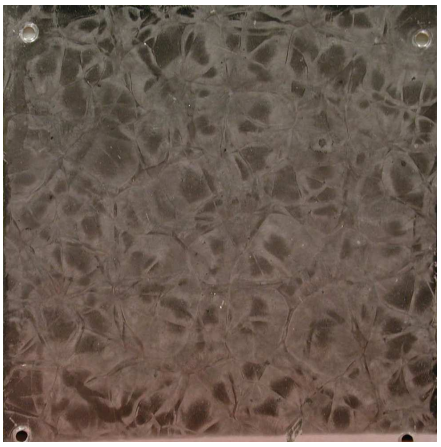

A.15: Shot 1389, 50% Nitrogen

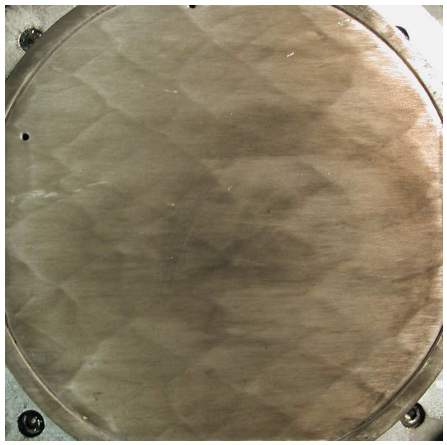

A.16: Shot 1389, 50% Nitrogen

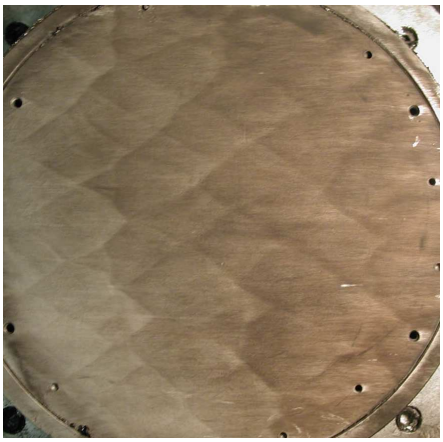

A.17: Shot 1389, 50% Nitrogen

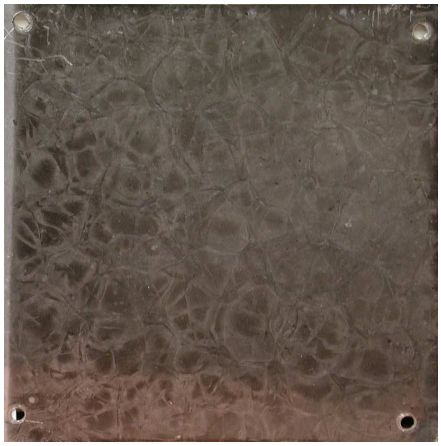

A.18: Shot 1390, 45% Nitrogen

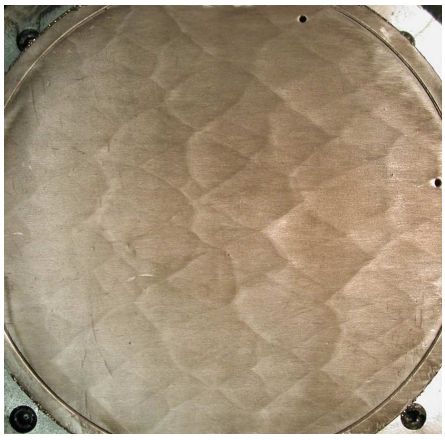

A.19: Shot 1390, 45% Nitrogen

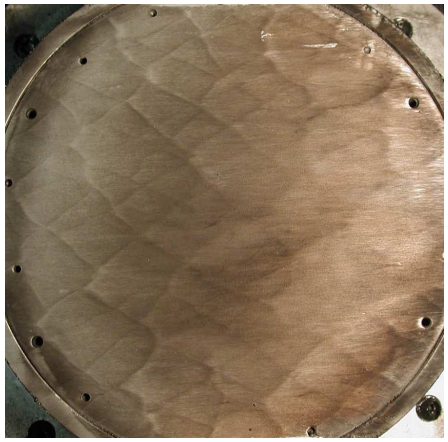

A.20: Shot 1390, 45% Nitrogen

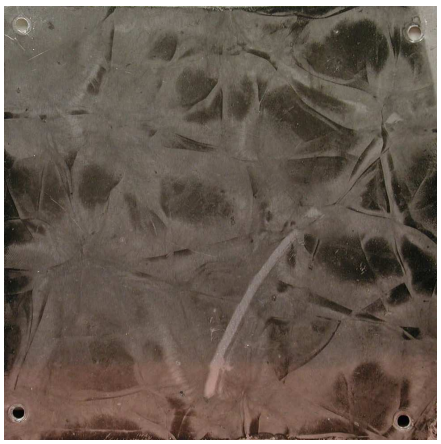

A.21: Shot 1391, 65% Nitrogen

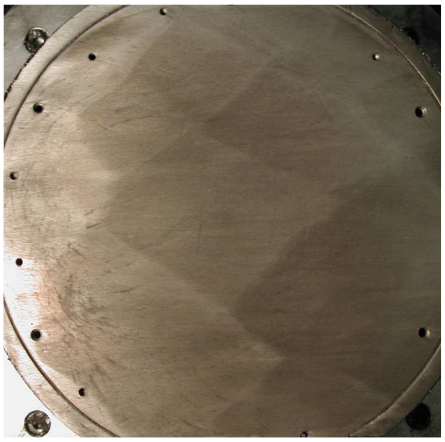

A.22: Shot 1391, 65% Nitrogen

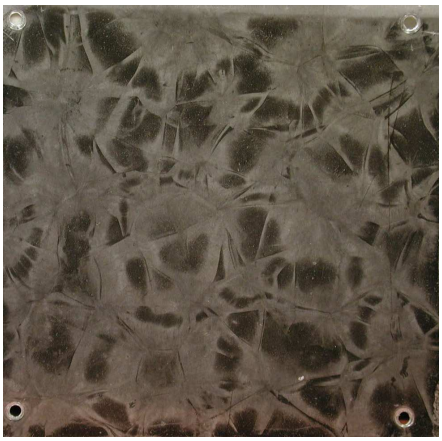

A.23: Shot 1392, 60% Nitrogen

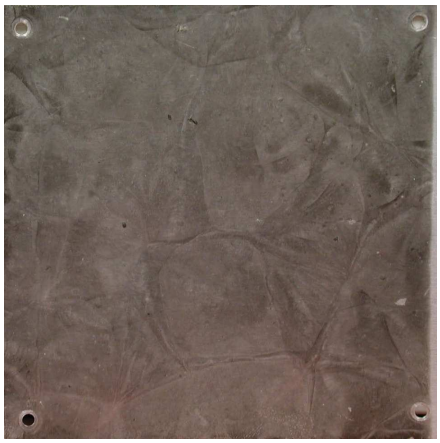

A.24: Shot 1394, 65% Nitrogen

Appendix B

Schlieren-photographs

The field of view for all Schlieren-photographs shown is 150mm x 150mm

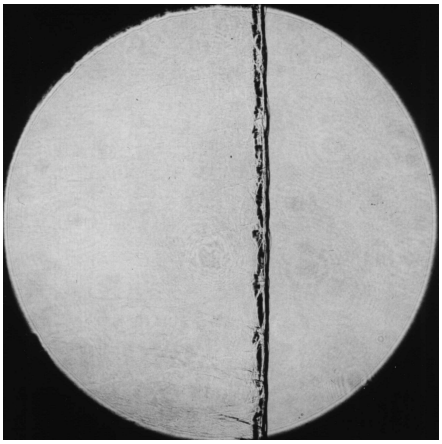

B.1: Shot 1365, 80% Argon

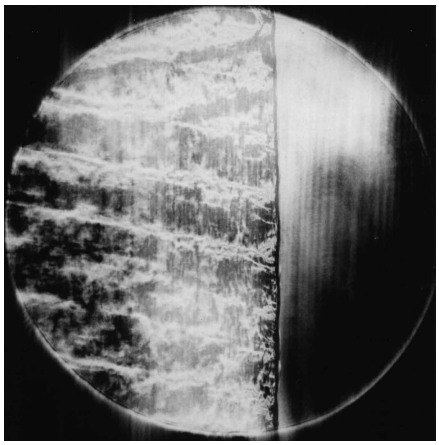

B.2: Shot 1367, 80% Argon

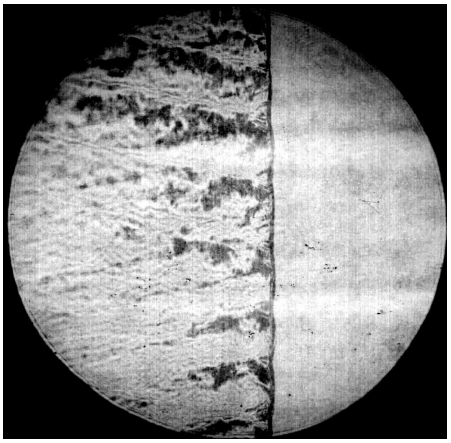

B.3: Shot 1369, 80% Argon

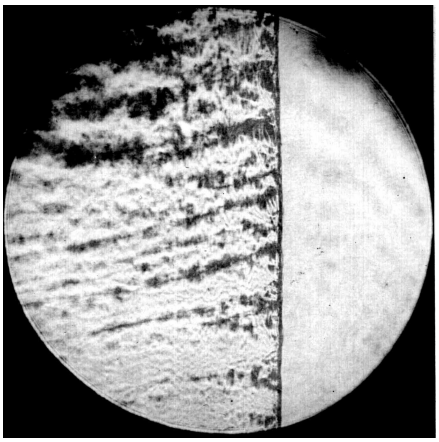

B.4: Shot 1370, 80% Argon

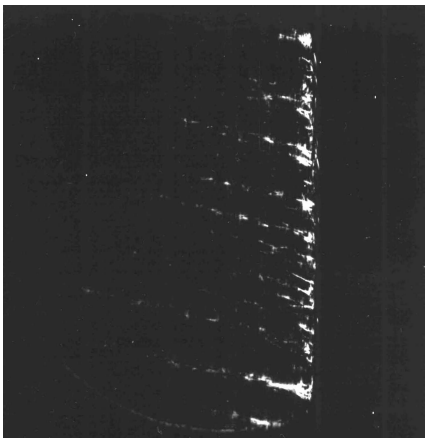

B.5: Shot 1371, 80% Argon

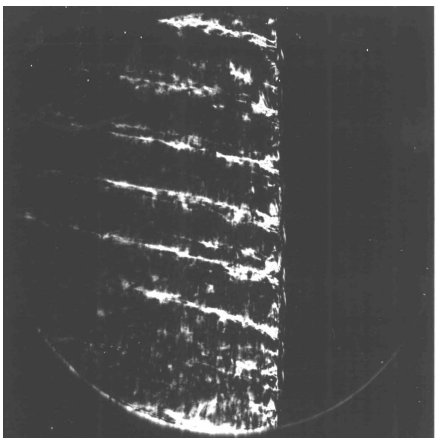

B.6: Shot 1372, 80% Argon

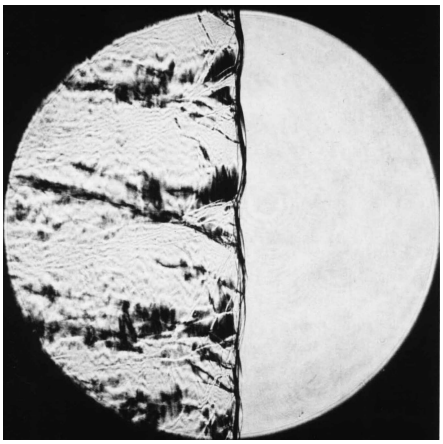

B.7: Shot 1373, 85% Argon

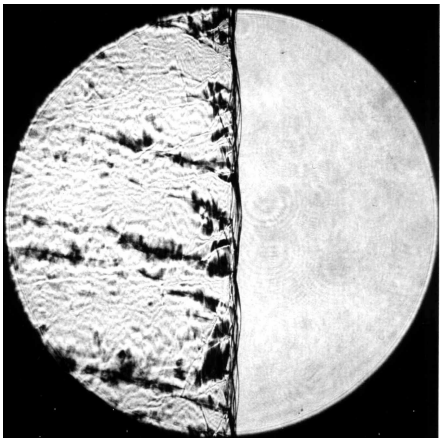

B.8: Shot 1374, 85% Argon

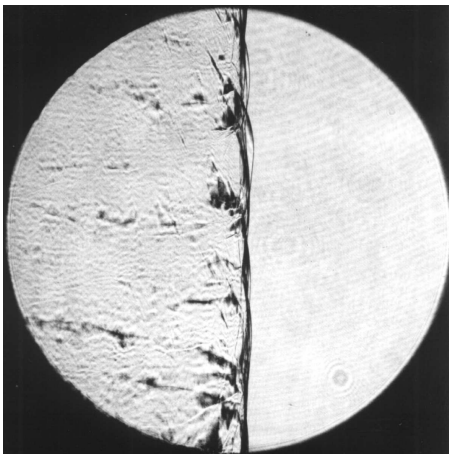

B.9: Shot 1375, 85% Argon

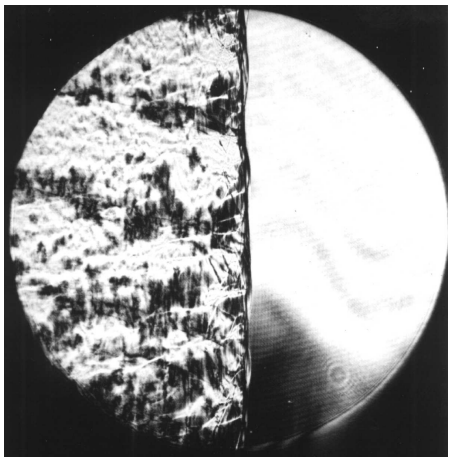

B.10: Shot 1376, 85% Argon

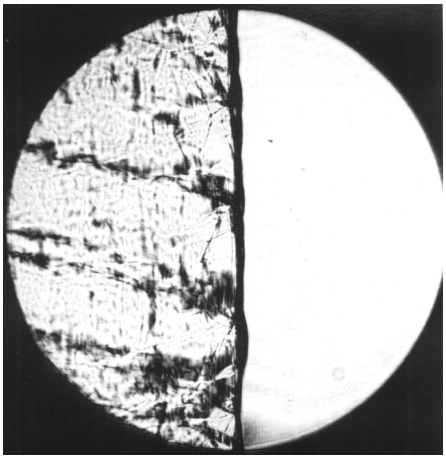

B.11: Shot 1377, 85% Argon

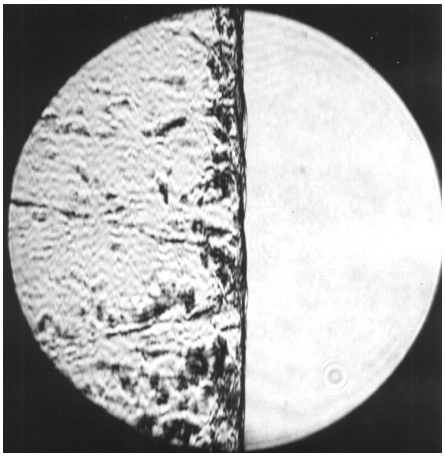

B.12: Shot 1378, 85% Argon

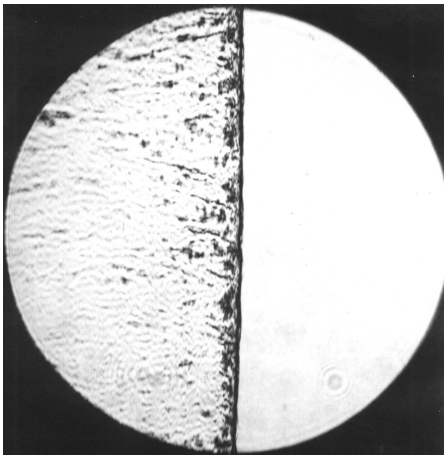

B.13: Shot 1379, 80% Argon

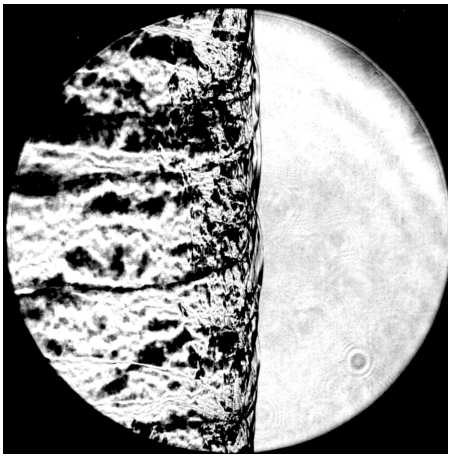

B.14: Shot 1396, 65% Nitrogen

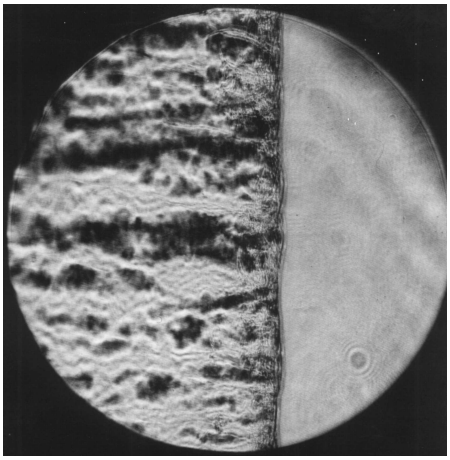

B.15: Shot 1397, 60% Nitrogen

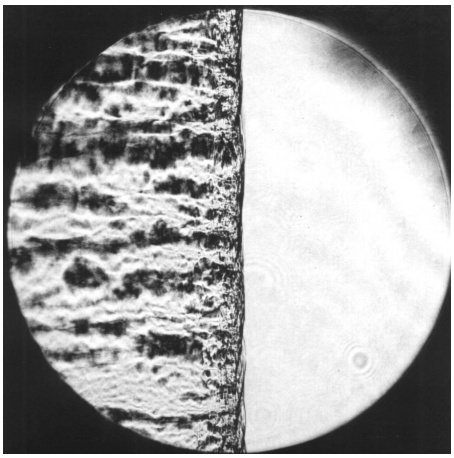

B.16: Shot 1399, 55% Nitrogen

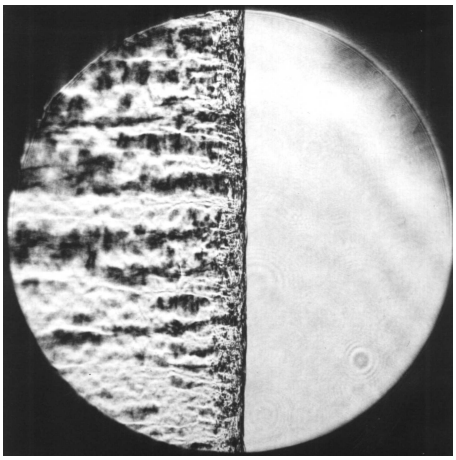

B.17: Shot 1400, 50% Nitrogen

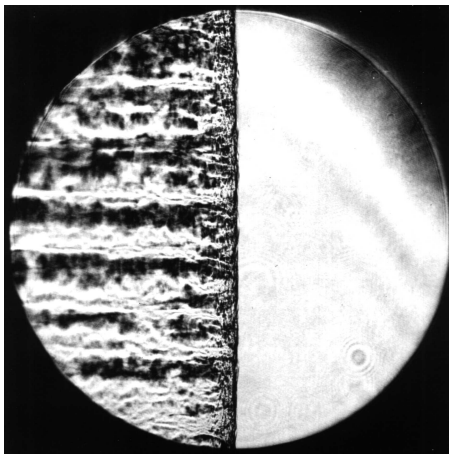

B.18: Shot 1401, 45% Nitrogen

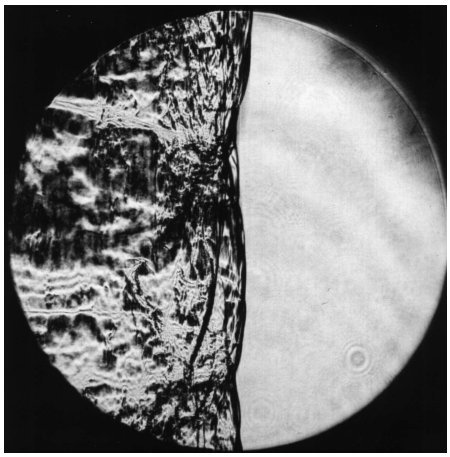

B.19: Shot 1402, 70% Nitrogen

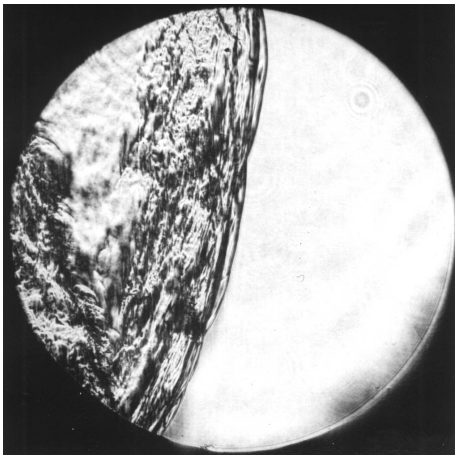

B.20: Shot 1403, 75% Nitrogen

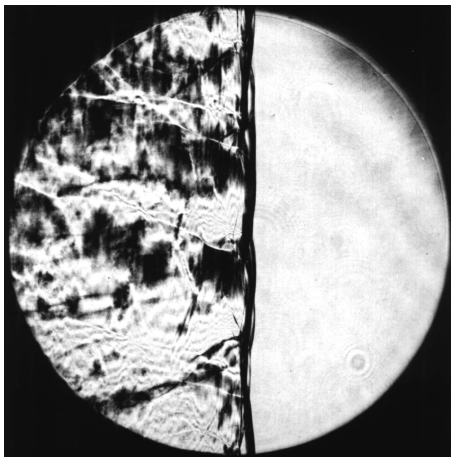

B.21: Shot 1404, 87% Argon

Appendix C

PLIF-pictures

The field of view for all PLIF-pictures shown is 75mm x 112mm.

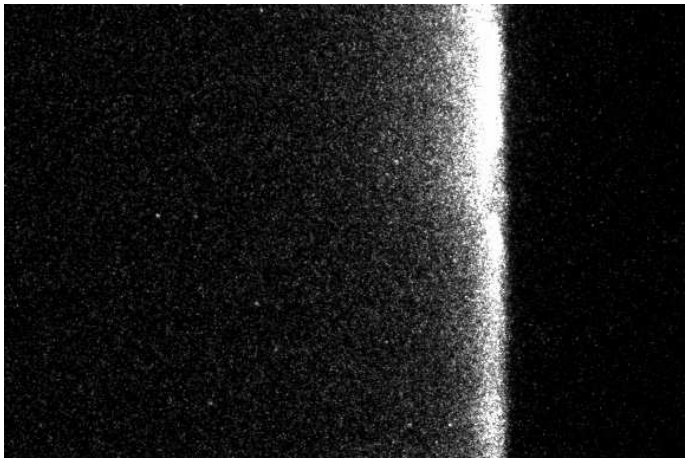

C.1: Shot 1359, 80% Argon

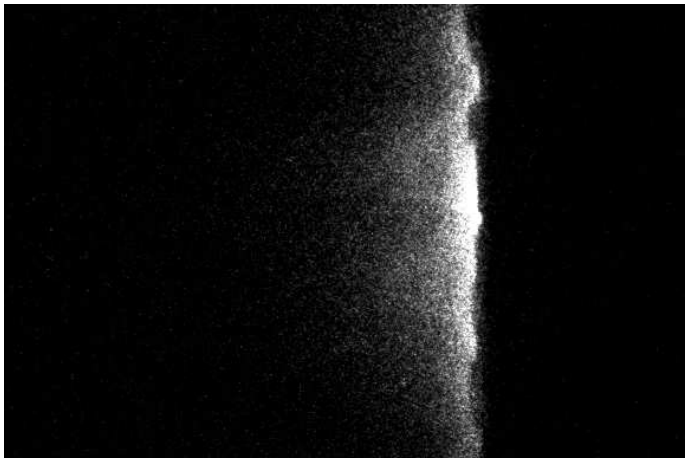

C.2: Shot 1361, 80% Argon

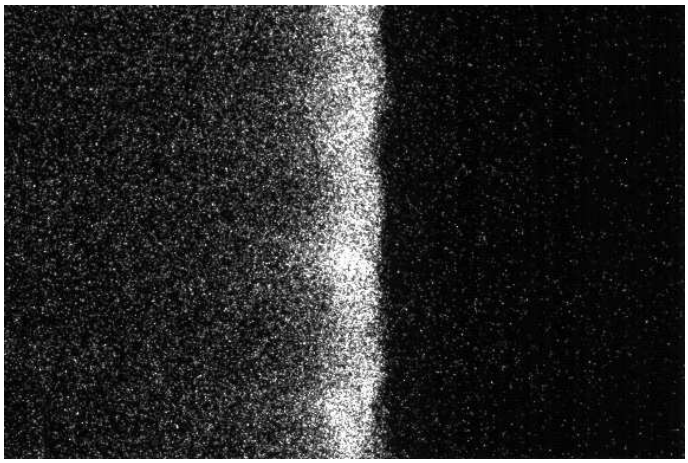

C.3: Shot 1362, 80% Argon

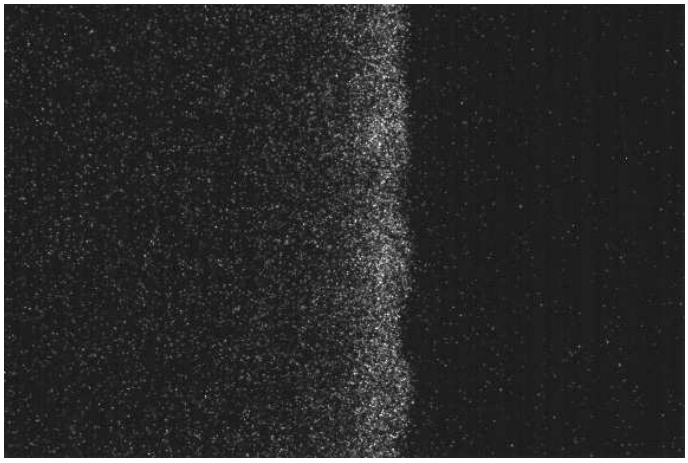

C.4: Shot 1363, 80% Argon

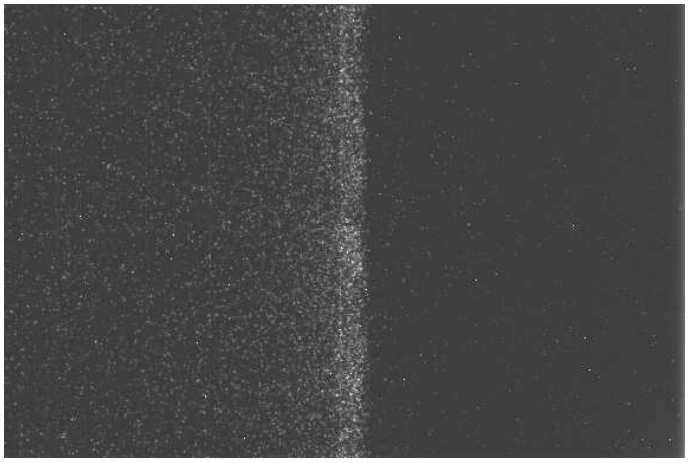

C.5: Shot 1406, 80% Argon

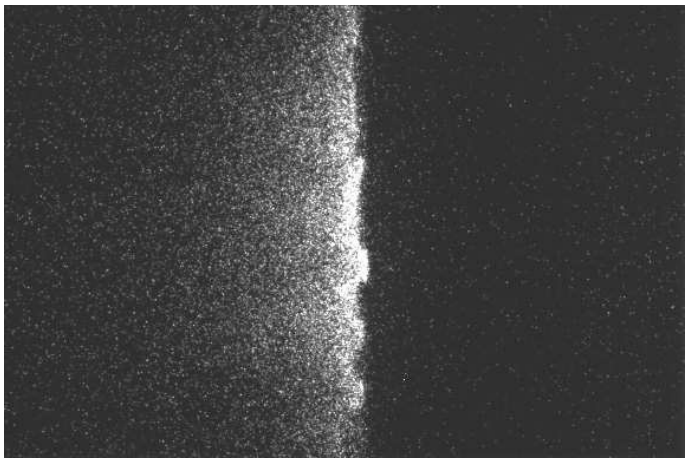

C.6: Shot 1407, 80% Argon

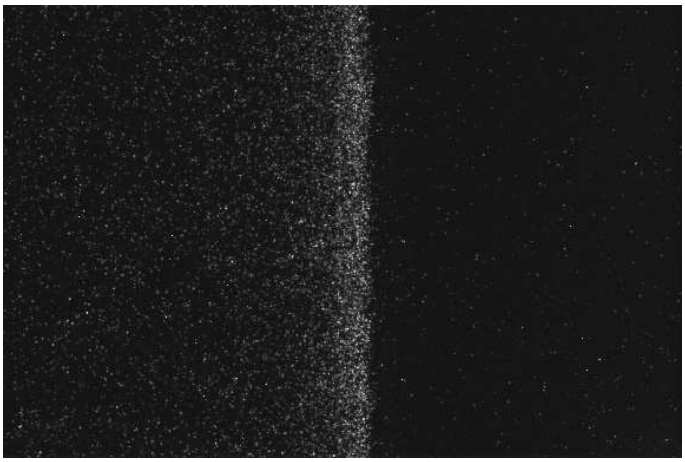

C.7: Shot 1408, 80% Argon

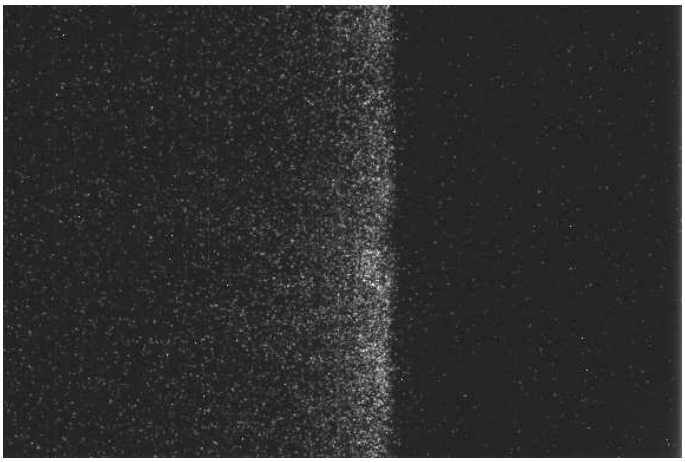

C.8: Shot 1409, 80% Argon

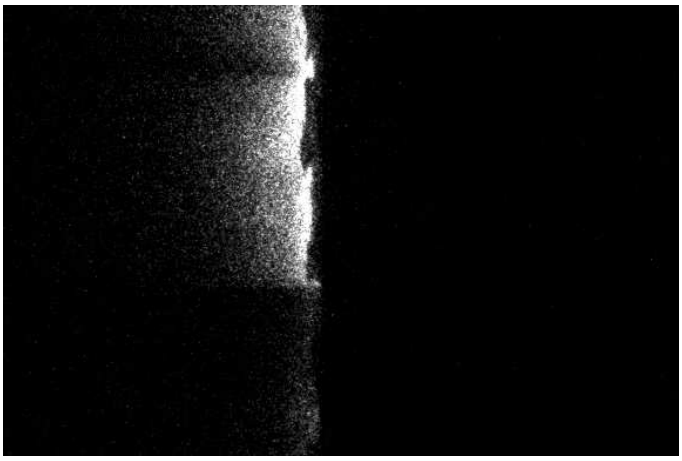

C.9: Shot 1411, 80% Argon

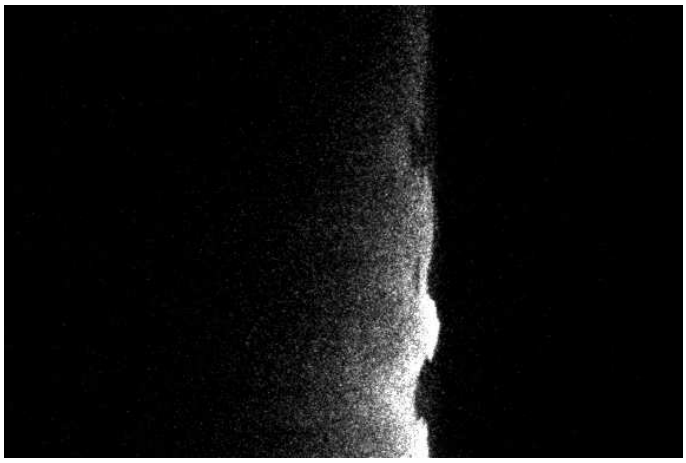

C.10: Shot 1412, 80% Argon

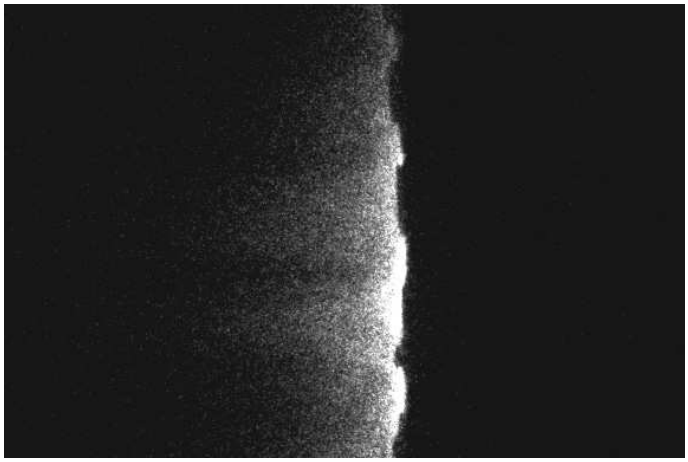

C.11: Shot 1415, 80% Argon

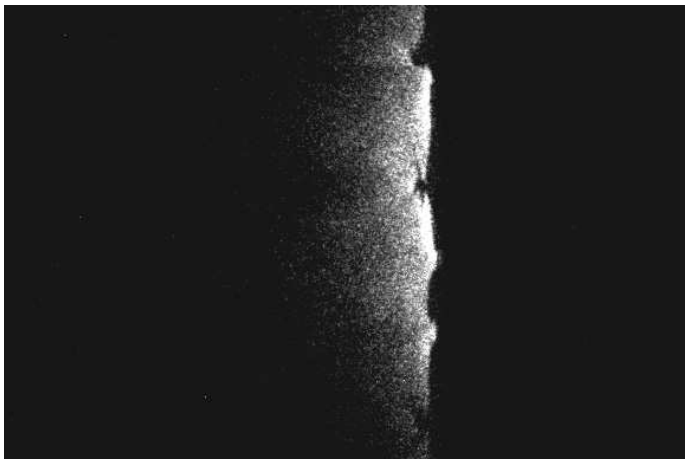

C.12: Shot 1416, 80% Argon

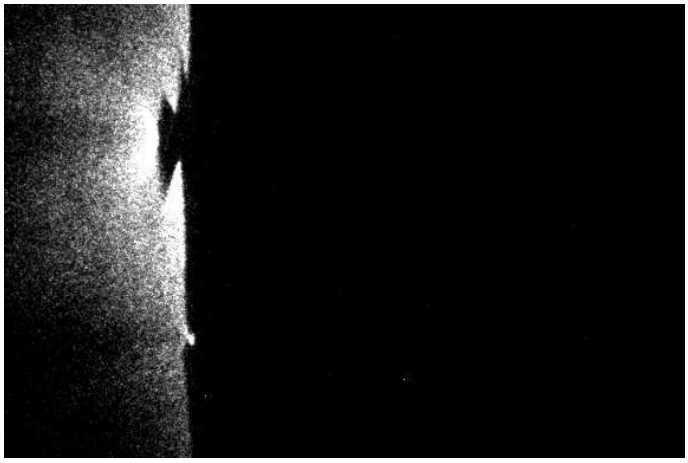

C.13: Shot 1417, 85% Argon

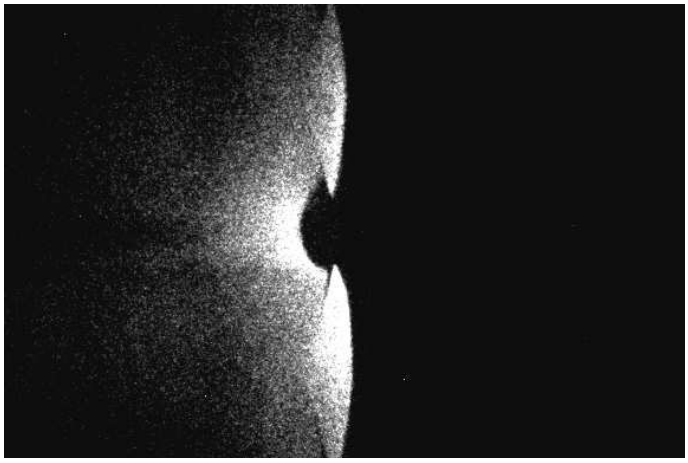

C.14: Shot 1419, 85% Argon

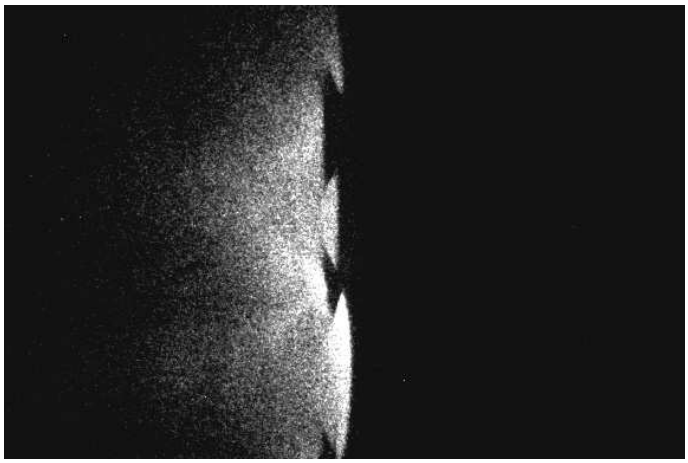

C.15: Shot 1420, 85% Argon

C.16: Shot 1421, 80% Argon

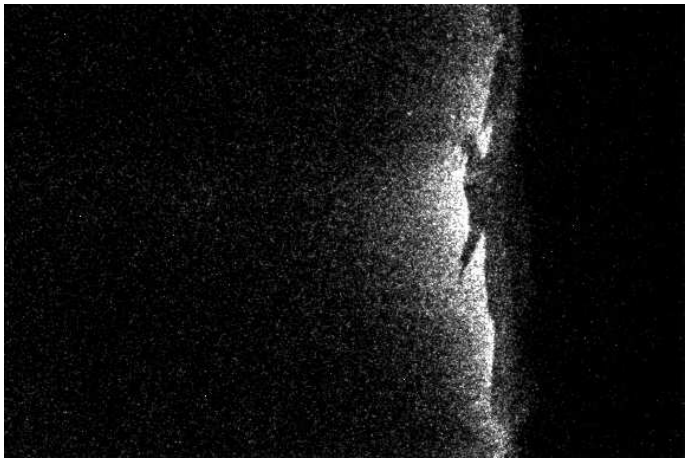

C.17: Shot 1422, 60% Nitrogen

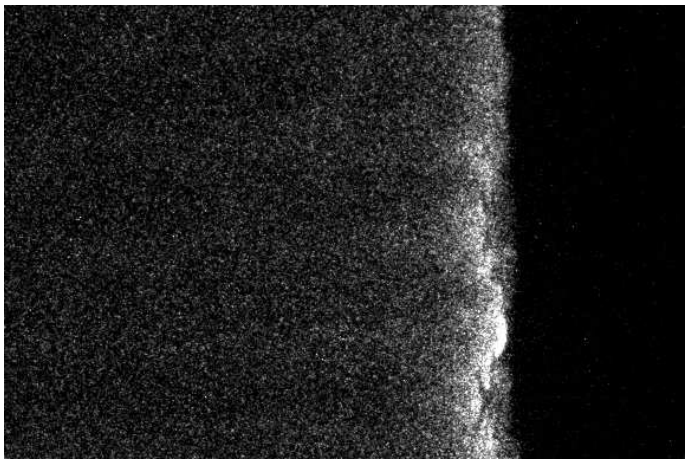

C.18: Shot 1423p, 45% Nitrogen

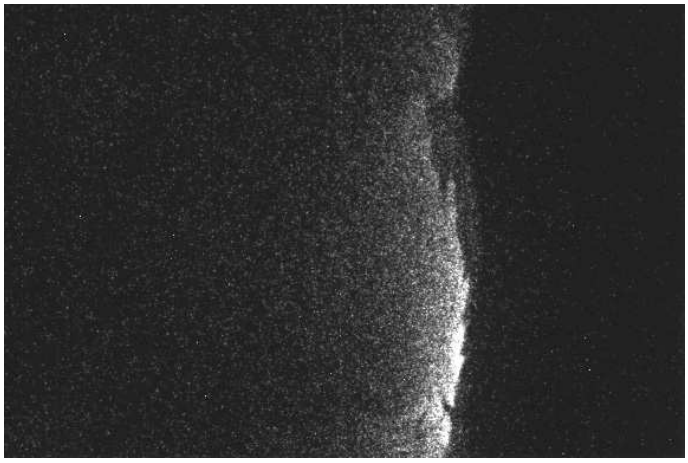

C.19: Shot 1424, 60% Nitrogen

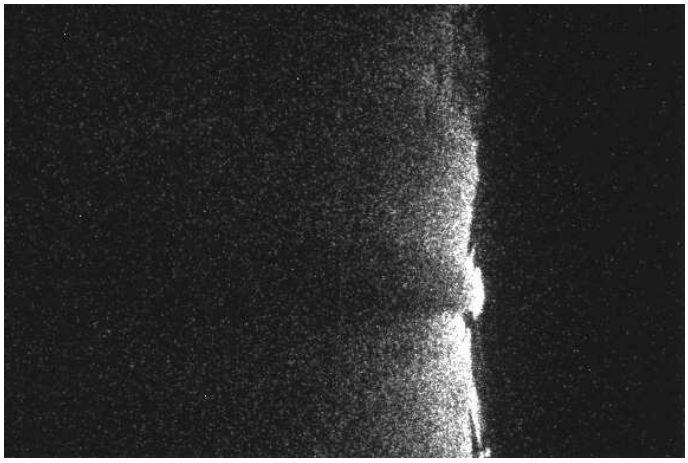

C.20: Shot 1425, 60% Nitrogen

C.21: Shot 1426, 60% Nitrogen

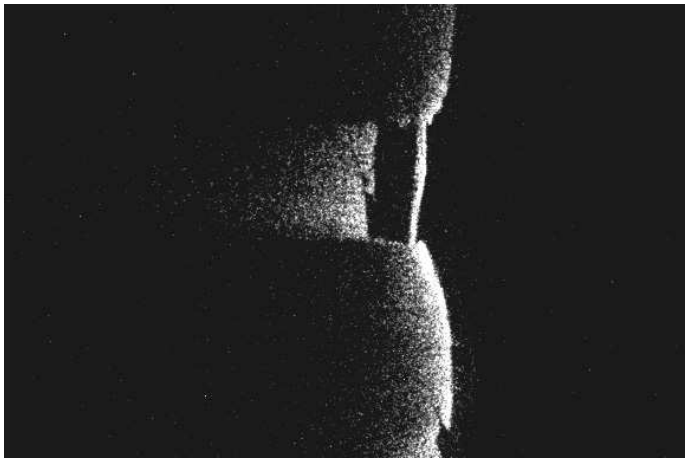

C.22: Shot 1427, 65% Nitrogen

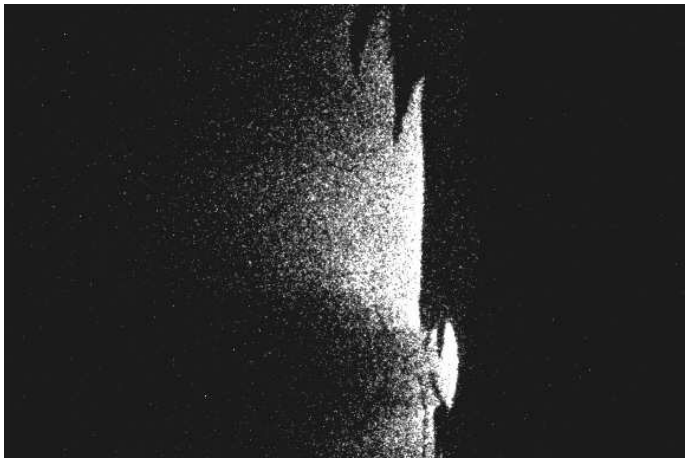

C.23: Shot 1428, 65% Nitrogen

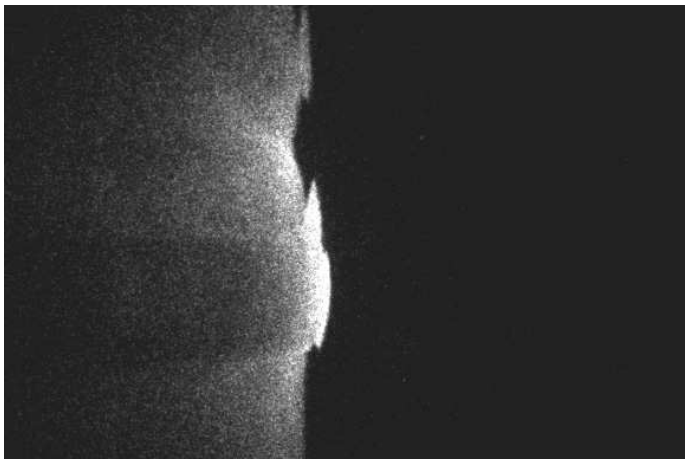

C.24: Shot 1429, 85% Argon

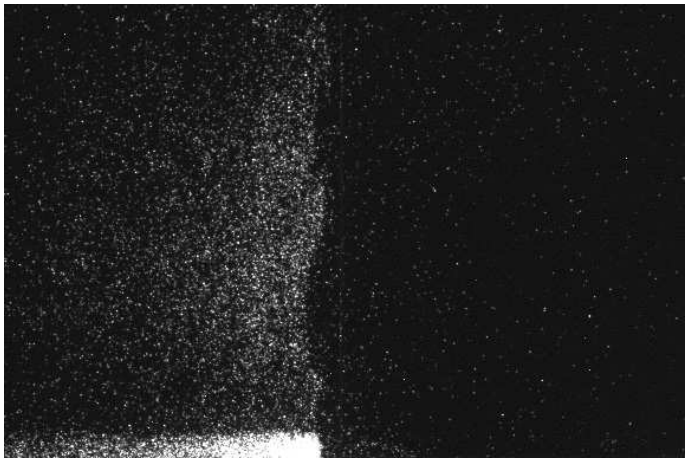

C.25: Shot 1430, 85% Argon

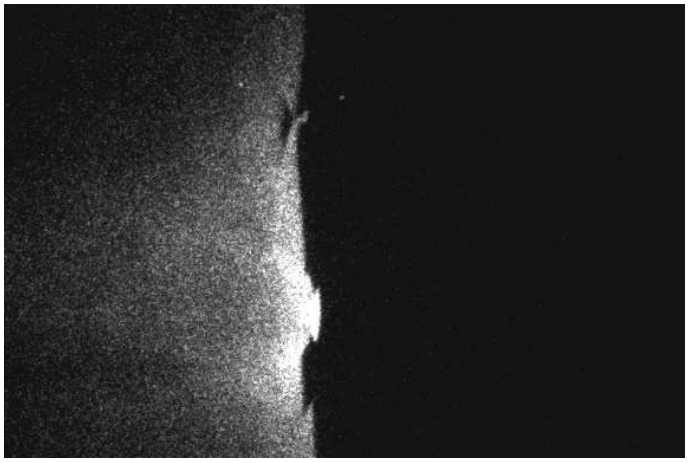

C.26: Shot 1431, 85% Argon

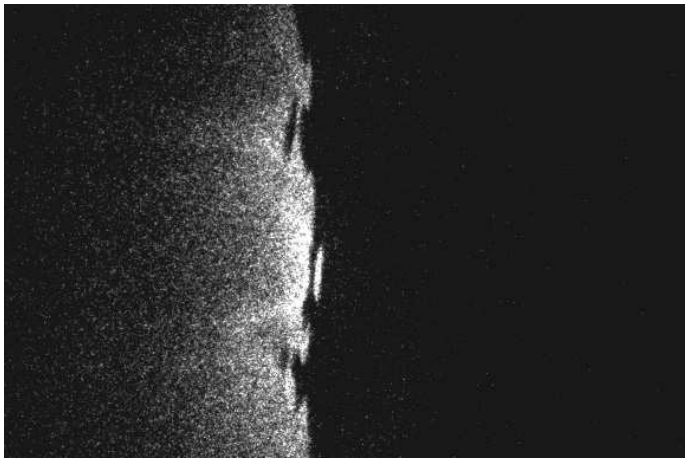

C.27: Shot 1432, 85% Argon

Appendix D

PLIF-Image Intensities

All intensities are measured in a 40 pixel wide horizontal stripe, averaged vertically. The length scale is set to 0 at the maximum OH-production ($\delta(OH)/\delta x = max.$).

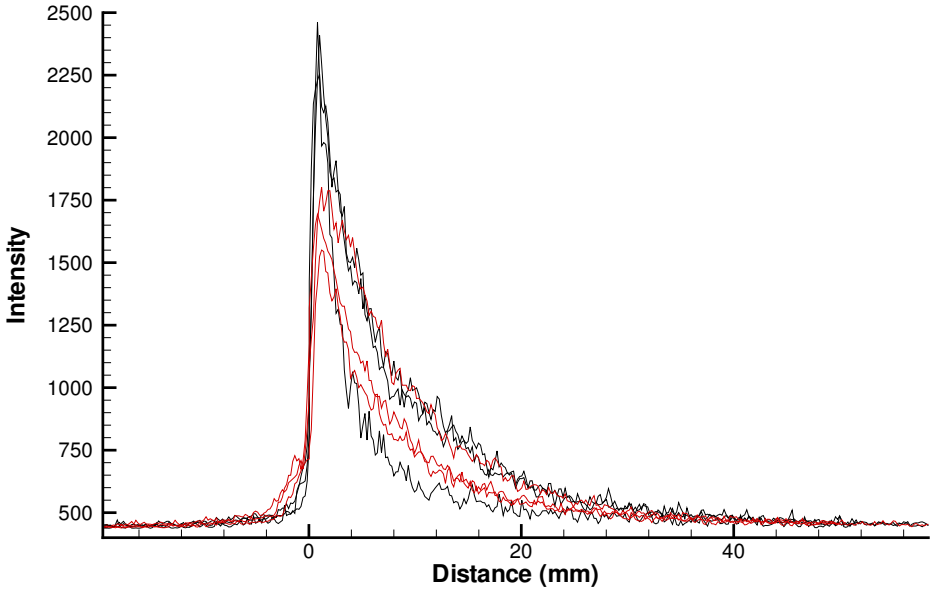

D.1: 80% Argon, black: stripe intersecting keystone of lower fluorescence (closing cell), red: stripe intersecting keystone of higher fluorescence (opening cell)

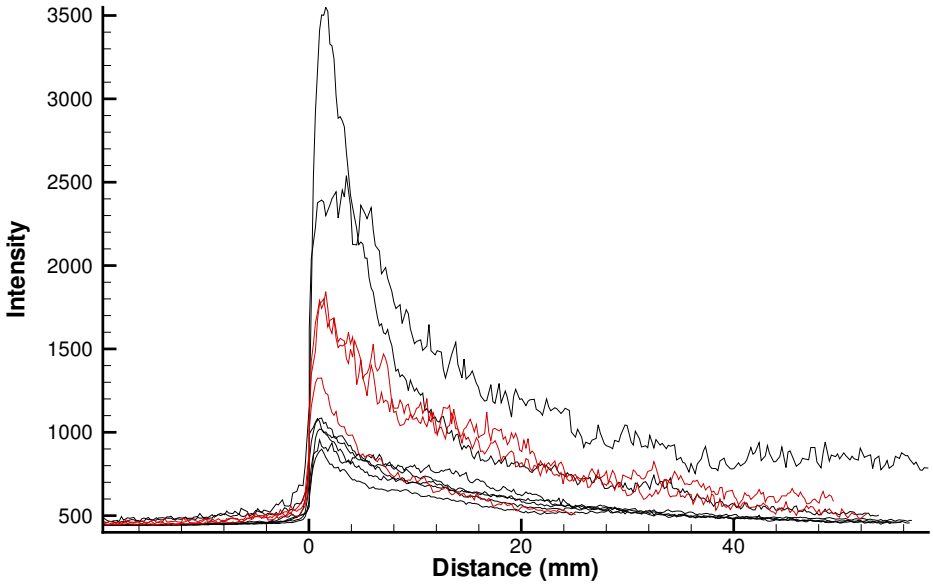

D.2: 85% Argon, black: stripe intersecting keystone of lower fluorescence (closing cell), red: stripe intersecting keystone of higher fluorescence (opening cell)

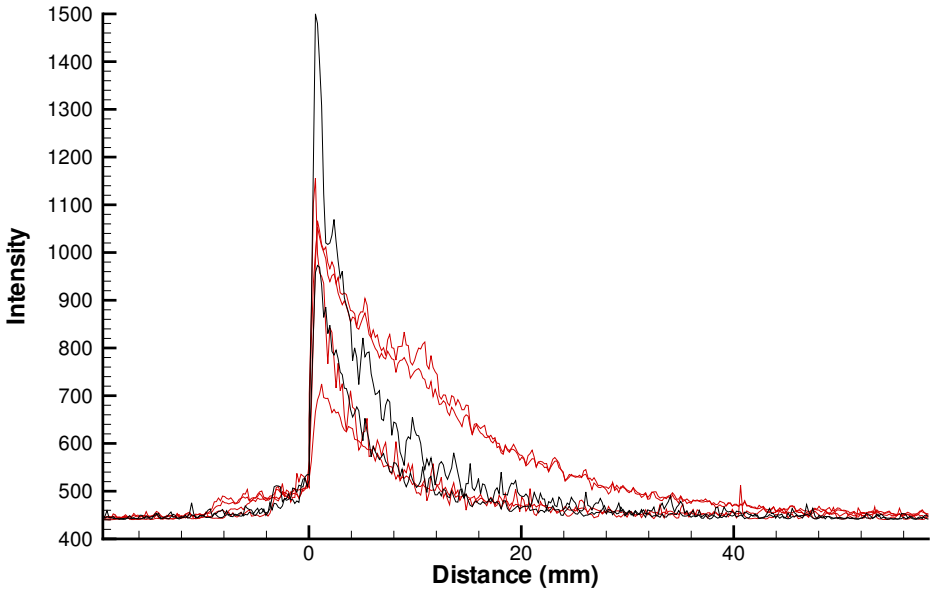

D.3: 65% Nitrogen, black: stripe intersecting keystone of lower fluorescence (closing cell), red: stripe intersecting keystone of higher fluorescence (opening cell)

Appendix E

Simultaneous Schlieren and PLIF-Images

All images shown are 70mm in height.

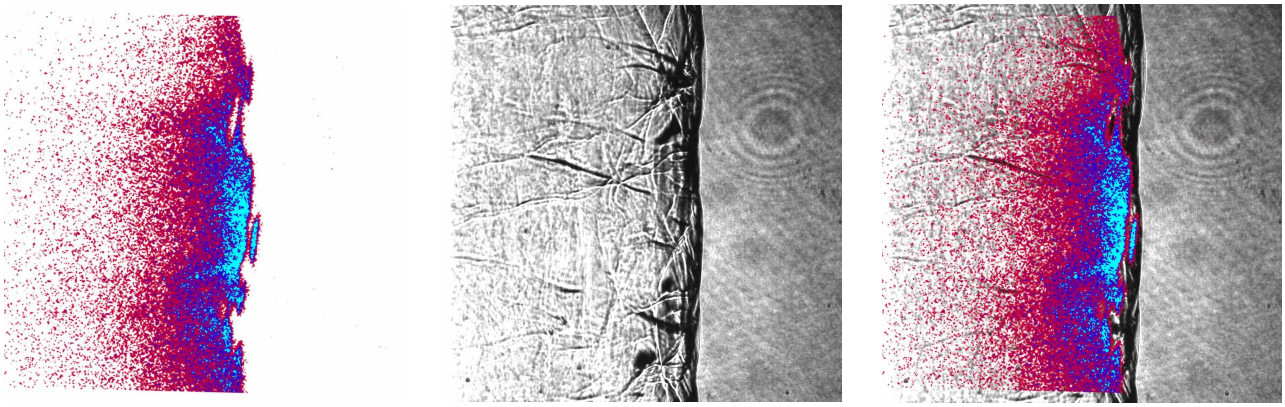

E.1: Shot 1432, 85% Argon

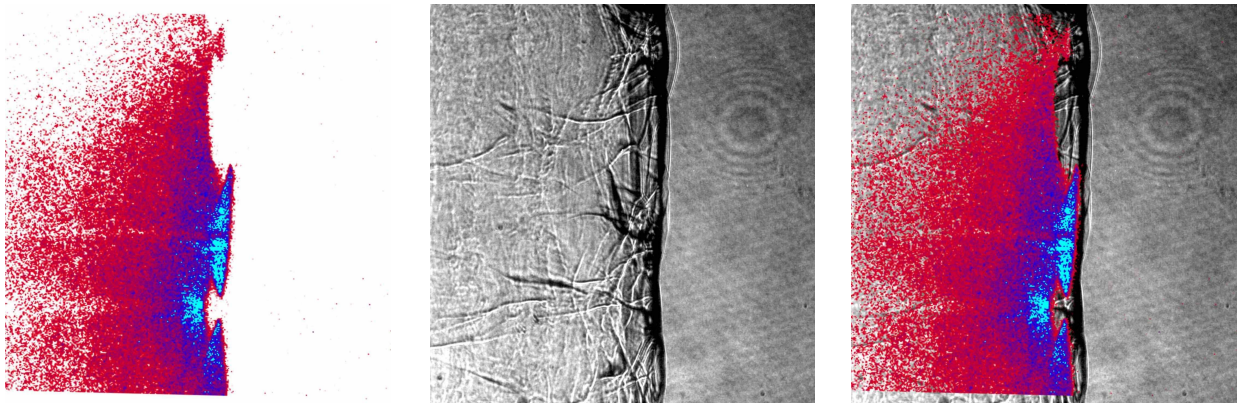

E.2: Shot 1433, 85% Argon

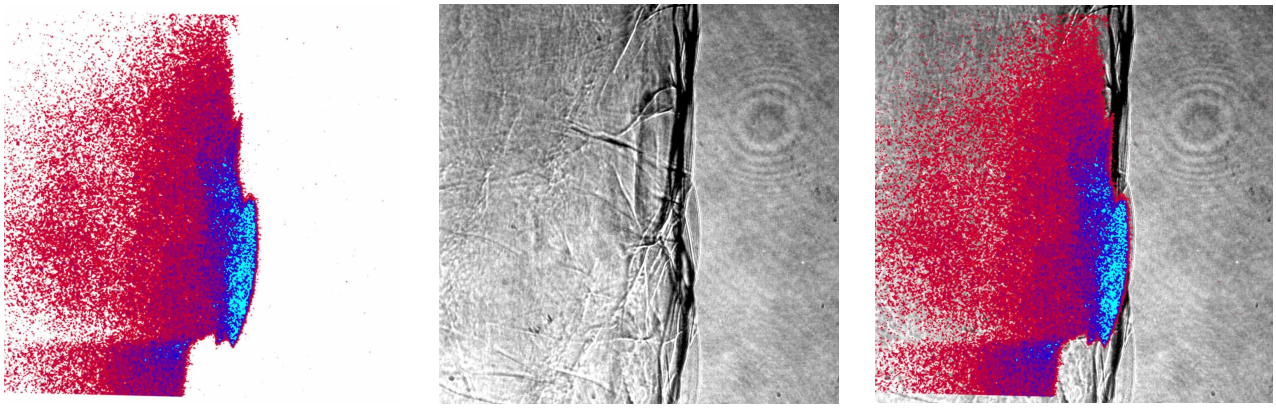

E.3: Shot 1434, 87% Argon

Appendix F

Shot list

	SETUP						Velocities					J-states		
shot	diluent	amount	O2	H2	press	temp	V 1-2	V 2-3	V 3-4	V 4-5	V_cj	T_cj	p_cj	v_psh
		%	%	%	kPa	C	m/s	m/s	m/s	m/s	m/s	K	kPa	m/s
1357	Ar	80	6,7	13,3	30	21					1526	2666	442	
1357b	Ar	80	6,7	13,3	30	21					1526	2666	442	
1358	Ar	80	6,7	13,3	30	21	1530	1514			1526	2666	442	
1359	Ar	80	6,7	13,3	30	20	1528	1517	1504	1486	1526	2666	442	
1360	Ar	80	6,7	13,3	20	21	1531	1517	1490	1436	1518	2640	291	921
1361	Ar	80	6,7	13,3	20	21	1531	1510	1483	1446	1518	2640	291	921
1362	Ar	80	6,7	13,3	20	21	1530	1508			1518	2640	291	921
1363	Ar	80	6,7	13,3	20	22	1531	1509	1479	1476	1518	2640	291	921
1364	Ar	80	6,7	13,3	20	25	1526	1511	1488	1445	1518	2640	291	921
1365	Ar	80	6,7	13,3	20	25	1534	1512	1486	1456	1518	2640	291	921
1366	Ar	80	6,7	13,3	20	25	1531	1509	1488	1445	1518	2640	291	921
1366b	Ar	80	6,7	13,3	20	25					1518	2640	291	921
1367	Ar	80	6,7	13,3	20	24	1528	1515	1488	1456	1518	2640	291	921
1369	Ar	80	6,7	13,3	20	24	1530	1510	1485	1466	1518	2640	291	921
1370	Ar	80	6,7	13,3	20	24	1526	1514	1485	1456	1518	2640	291	921
1371	Ar	80	6,7	13,3	20	23	1531	1542	1494	1456	1518	2640	291	921
1372	Ar	80	6,7	13,3	20	23					1518	2640	291	921
1373	Ar	85	5	10	20	24	1431	1401	1371	1363	1415	2349	253	814
1374	Ar	85	5	10	20	23	1428	1406	1373	1346	1415	2349	253	814
1375	Ar	85	5	10	20	21	1426	1395	1366	1354	1415	2349	253	814
1376	Ar	85	5	10	20	21	1435	1401	1374	1338	1415	2349	253	814
1377	Ar	85	5	10	20	21	1432	1402	1376	1338	1415	2349	253	814
1378	Ar	85	5	10	20	22	1429	1398	1366	1329	1415	2349	253	814
1379	Ar	80	6,7	13,3	20	21	1532	1511	1488	1445	1518	2640	291	921
1380	Ar	80	6,7	13,3	20	22	1532	1512	1488	1455	1518	2640	291	921
1381	Ar	80	6,7	13,3	20	17	1522	1502	1474	1436	1518	2640	291	921
1382	Ar	80	6,7	13,3	20	18	1527	1509	1490	1465	1518	2640	291	921
1383	Ar	80	6,7	13,3	20	17	1526	1508	1492	1455	1518	2640	291	921
1384	Ar	85	5	10	20	19	1425	1397	1374	1371	1415	2349	253	814
1385	Ar	70Ar + 18O2 + 8 H2 + 4 C2H2 *					1689	1658	1627	1597				
1386	Ar	85	5	10	20	21	1429	1396	1365	1337	1415	2349	253	814
1387	Ar	85	5	10	20	21	1430	1400	1369	1329	1415	2349	253	814
1388	N2	55	15	30	20	20	1953	1947	1922	1910	1943	2838	309	1367
1389	N2	50	16,7	33,3	20	20	2022	1015	1989	1981	2008	2928	318	1317
1390	N2	45	18,3	36,7	20	20	2048	2076	2061	2018	2071	3003	325	1364
1391	N2	65	11,7	23,3	20	21	1810	1803	1768	1739	1799	2583	281	1150
1392	N2	60	13,3	26,7	20	19	1892	1876	1854	1844	1875	2726	297	1213
1393	N2	63	12,3	24,7	20	20								
1394	N2	65	11,7	23,3	20	21	1814	1793	1771	1754	1799	2583	281	1150
1395	N2	65	11,7	23,3	20	21	1817	1797	1771	1740	1799	2583	281	1150
1396	N2	65	11,7	23,3	20	21	1817	1798	1771	1754	1799	2583	281	1150
1397	N2	60	13,3	26,7	20	21	1889	1882	1854	1861	1875	2583	281	1213
1398	N2	55	15	30	20	21					1943	2838	309	1367
1399	N2	55	15	30	20	20	1961	1948	1929	1877	1943	2838	309	1367

* accidentally two driver gas injections prior the ignition procedure

	SETUP						Velocities				C		J-states		
shot	diluent	amount	O2	H2	press	temp	V 1-2	V 2-3	V 3-4	V 4-5	V_cj	T_cj	p_cj	v_psh
		%			kPa	C	m/s	m/s	m/s	m/s	m/s	K	kPa	m/s
1400	N2	50	16,7	33,3	20	20	2024	1015	1993	1945	2008	2928	318	1317
1401	N2	45	18,3	36,7	20	20	2087	2078	2057	2019	2071	3003	325	1364
1402	N2	70	10	20	20	21	1720	1715	1671	1634	1710	2397	261	1074
1403	N2	75	8,3	16,7	20	21	1607	1591	1514	1259	1632	2223	241	1005
1404	Ar	87	4,3	8,7	20	21	1383	1339	1307	1305	1355	2169	229	748
1405	Ar	90	3,3	6,7	20	21					1235	1824	189	618
1406	Ar	80	6,7	13,3	20	21	1535	1511	1488	1456	1518	2640	291	921
1407	Ar	80	6,7	13,3	20	21	1531	1511	1488	1466	1518	2640	291	921
1408	Ar	80	6,7	13,3	20	21	1531	1509	1486	1456	1518	2640	291	921
1409	Ar	80	6,7	13,3	20	21	1535	1510	1488	1446	1518	2640	291	921
1410	Ar	80	6,7	13,3	20	21	1533	1512	1486	1456	1518	2640	291	921
1411	Ar	80	6,7	13,3	20	21	1531	1510	1485	1446	1518	2640	291	921
1412	Ar	80	6,7	13,3	20	21	1538	1511	1485	1466	1518	2640	291	921
1413	Ar	80	6,7	13,3	20	21	1534	1507	1486	1446	1518	2640	291	921
1414	Ar	80	6,7	13,3	20	21	1535	1510	1484	1466	1518	2640	291	921
1415	Ar	80	6,7	13,3	20	21	1538	1513	1488	1476	1518	2640	291	921
1416	Ar	80	6,7	13,3	20	21	1537	1515	1488	1466	1518	2640	291	921
1417	Ar	85	5	10	20	21	1429	1399	1369	1654	1415	2349	253	814
1418	Ar	85	5	10	20	21	1430	1399	1369	1354	1415	2349	253	814
1419	Ar	85	5	10	20	21	1436	1395	1371	1329	1415	2349	253	814
1420	Ar	85	5	10	20	21	1431	1396	1372	1329	1415	2349	253	814
1421	Ar	80	6,7	13,3	20	21	1531	1510	1484	1456	1518	2640	291	921
1422	N2	60	13,3	26,6	20	21	1896	1877	1848	1861	1875	2583	281	1213
1423	N2	45	18,3	36,7	20	21	2091	2072	2046	2038	1875	2583	281	1213
1424	N2	60	13,3	26,7	20	21	1892	1878	1851	1829	1875	2583	281	1213
1425	N2	60	13,3	26,7	20	21	1889	1882	1848	1861	1875	2583	281	1213
1426	N2	60	13,3	26,7	20	21	1894	1873	1842	1798	1875	2583	281	1213
1427	N2	65	11,7	23,3	20	21	1817	1797	1771	1754	1799	2583	281	1150
1428	N2	65	11,7	23,3	20	21	1810	1797	1763	1754	1799	2583	281	1150
1429	Ar	85	5	10	20	21	1430	1393	1364	1646	1415	2349	253	814
1430	Ar	85	5	10	20	21	1435	1397	1371	1363	1415	2349	253	814
1431	Ar	85	5	10	20	21	1433	1347	1371	1346	1415	2349	253	814
1432	Ar	85	5	10	20	21	1424	1390	1369	1338	1415	2349	253	814
1433	Ar	85	5	10	20	21	1430	1395	1371	1329	1415	2349	253	814
1434	Ar	87	4,3	8,7	20	21	1385	1336	1368	1274	1355	2169	229	748
1435	Ar	87	4,3	8,7	20	21	1383	1338	1307	1289	1355	2169	229	748

Bibliography

[AD92] T. Anderson and E. Debora. Measurements of normal detonation wave structure using rayleigh scattering. *24th Symposium (International) on Combustion*, pages 1853–1860, 1992.

[Akb00] R. Akbar. *Mach Reflection of Gasious Detonations*. PhD thesis, California Institute of Technology, 2000.

[AWW+92] P. Anderson, W.Reckers, H. Wagner, E. Debora, and H. Voges. The structure of gasous detonations as revealed by laser-induced flourescence of the oh-radical. *Zeitschrift für Physikalische Chemie*, Neue Folge 175:129–143, 1992.

[Bar75] F. Bartlm. *Gasdynamik der Verbrennung*. Springer Verlag, Wien, 1975.

[Bra97] U. Brackmann. *Lambdachrome Laser Dyes*. Lambda Physik, Göttingen, Germany, 1997.

[Bre61] Robert G. Brenne. *The shift and shape of spectral lines*. Pergamon Press, New York, 1961.

[DMW87] F. Durst, A. Melling, and J.H. Whitelaw. *Theorie und Praxis der Laser-Doppler-Anemometrie*. G. Braun, Karlsruhe, 1987.

[Dvo80] V. Dvorak. *Wiedemanns Analen*. 1880.

[Eck96] C. Eckbreth. *Laser Diagnostics for Combustion Temperature and Species*. Gordon and Breach Publishers, 1996. ISBN 90-5699-532-4.

[Eck00] C. Eckert. *Numerical and Analytical Studies of the Dynamics os Gasous Detonations*. PhD thesis, California Institute of Technology, 2000.

[FD79] W. Fickett and W.C. Davis. *Detonation*. University of California Press, 1979.

[Fow68] Grant F. Fowlers. *Introduction to modern otics*. Holt, Rinehart and Winston Inc., 1968.

[GDO99] V.N. Gamezo, D. Desbores, and E.S. Oran. Formation and evolution of two-dimensional cellular detonations. *Combustion & Flame*, 116:154–165, 1999.

[HLvT00] Z.W. Huang, M.H. Lefebvre, and P.J. v. Tiggelen. Experiments on spinning detonations with detailed analysis of the shock structure. *Shock Waves*, 10:119–125, 2000.

[KRM89] R.J. Kee, F.M. Rupley, and J.A. Miller. CHEMKIN-II: A FORTRAN chemical kinetics package for the analysis of gas-phase chemical kinetics. Technical Report SAND89-8009, Sandia National Laboratory, 1989.

[LC99] J. Luque and D.R. Crosley. Lifbase: Database and spectral simulation program (version 1.5). Technical Report MP-99-009, SRI International, 1999.

[Lee84] J.H.S. Lee. Dynamic parameters of gaseous detonations. *Annual Review of Fluid Mechanics*, 16:311–336, 1984.

[LOK92] M.H. Lefebvre, E.S. Oran, and K. Kailasanath. Computations of detonation structure: The influence of model input parameters. Technical Report NRL/MR/4404–92-6961, Naval Research Laboratory, Washington, 1992.

[LOKvT93] M.H. Lefebvre, E.S. Oran, K. Kailasanath, and P.J. v. Tiggelen. The influence of the heat capacity and diluent on detonation structure. *Combustion & Flame*, 95:206–218, 1993.

[LWO95] M.H. Lefebvre, J.W. Weber, and E.S. Oran. Numerical simulations of a marginal detonation: Wave velocities and transverse wave structure. To appear in book *Fluid Mechanics and Applications*, Eds.: B. Deshaies and L.F. da Silva, 1995.

[MF01] F. Mayinger and O. Feldmann, editors. *Optical Measurements. Techniques and Applications*. Springer Verlag, Berlin, 2 edition, 2001.

[Pan97] E. Pantow. *Ausbreitung und Zerfall von Detonationsfronten in Wechselwirkung mit technischen Strukturen*. VDI Fortschrittberichte, Reihe 7:Strmungstechnik, Nr. 330. VDI Verlag, Dsseldorf, 1997.

[Rey86] W.C. Reynolds. The element potential method for chemical equilibrium analysis: Implementation in the interactive program STANJAN, version 3. Technical report, Dept. of Mechanical Engineering, Stanford, CA, 1986.

[Sch34] H. Schardin. Das toeplersche schlierenverfahren. *VDI-Forschungsheft*, 367, 1934.

[Sch00] E. Schultz. *Detonation Diffraction Through an Abrupt Area Expansion*. PhD thesis, California Institute of Technology, 2000.

[She86] J.E. Shepherd. Chemical kinetics of hydrogen-air-diluent detonations. In J.R. Bowen and J.C. Leyer, editors, *Dynamics of Explosion*, volume 106 of *Prog. in Astronautics and Aeronautics*, pages 263–293. AIAA, 1986.

[She99] J.E. Shepherd. Turbulence behind the front. In *Proc. of the 17th Int. Coll. on the Dynamics of Explosions and Reactive Systems (ICDERS)*, Heidelberg, 1999. ISBN 3-932217-01-2.

[SMMT86] J.E. Shepherd, I.O. Moen, S.B. Murray, and P.A. Thibault. Analysis of the cellular structure of detonations. In *21st (Int.) Symposium on Combust.*, pages 1649–1658. The Combustion Institute, 1986.

[SS99] E. Schultz and J.E. Shepherd. Detonation analysis using detailed reaction mechanisms. In *Proceedings of the 22nd Int. Symp. on Shock Waves (ISSW22)*, London, 1999. ISBN 085432-706-1.

[SWS99] E. Schultz, E. Wintenberger, and J.E. Shepherd. Investigation of deflagration to detonation transition for application to pulse detonation engine ignition systems. In *Proceedings of the 16th JANNAF Propulsion Symposium*. Chemical Propulsion Information Agency, 1999.

[Toe64] A. Toepler. *Beobachtungen nach einer neuen optischen Methode*. Max Cohen und Sohn, Bonn, 1864.

[VMT69] B.V. Voytsekhovskiy, V.V. Mitrofanov, and M.Y. Tipchiyan. Investigation of the structure of detonation waves in gases. In *12th (Int.) Symposium on Combust.*, pages 829–837. The Combustion Institute, 1969.

[vN42] J. v. Neumann. Progress report on theory of detonation waves. Technical report, Office of Scientific Research and Development, OSDR Rep. No. 549, Proj. Rep. No. 238, 1942.

[Zel50] Y.B. Zel'dovich. On the theory of the propagation of detonation in gaseous systems. NACA TM, No. 1261, ursprgl. JETP10 (1940), 1950.